Characterization of Metal Contacts on Hydrothermally Synthesized Uranium Dioxide For Novel Semiconductor Applications

THESIS

Tory E. Robinson, Captain, USAF

AFIT-ENG-MS-19-M-052

DEPARTMENT OF THE AIR FORCE
AIR UNIVERSITY

AIR FORCE INSTITUTE OF TECHNOLOGY

Wright-Patterson Air Force Base, Ohio

DISTRIBUTION STATEMENT A
APPROVED FOR PUBLIC RELEASE; DISTRIBUTION UNLIMITED

The views expressed in this document are those of the author and do not reflect the official policy or position of the United States Air Force, the United States Department of Defense or the United States Government. This material is declared a work of the U.S. Government and is not subject to copyright protection in the United States.

AFIT-ENG-MS-19-M-052

CHARACTERIZATION OF METAL CONTACTS ON HYDROTHERMALLY SYNTHESIZED URANIUM DIOXIDE FOR NOVEL SEMICONDUCTOR APPLICATIONS

THESIS

Presented to the Faculty
Department of Engineering and Management
Graduate School of Engineering and Management
Air Force Institute of Technology
Air University
Air Education and Training Command
in Partial Fulfillment of the Requirements for the
Degree of Master of Science

Tory E. Robinson, BSEE
Captain, USAF

March 2019

DISTRIBUTION STATEMENT A
APPROVED FOR PUBLIC RELEASE; DISTRIBUTION UNLIMITED

AFIT-ENG-MS-19-M-052

CHARACTERIZATION OF METAL CONTACTS ON HYDROTHERMALLY SYNTHESIZED URANIUM DIOXIDE FOR NOVEL SEMICONDUCTOR APPLICATIONS

THESIS

Tory E. Robinson, BSEE
Captain, USAF

Committee Membership:

Maj. Tod V. Laurvick, PhD
Chair

Hengky Chandrahalim, PhD
Member

Maj Nicholas C. Herr, PhD
Member

George G. Peterson, PhD
Member

AFIT-ENG-MS-19-M-052

Abstract

This research is focused on determining which metals or combinations of metals form effective electrical contacts on hydrothermally synthesized UO_2 substrates to allow for additional work in characterization of the material and the feasibility of its use in semiconductor devices such as solid-state neutron detectors. A methodology was established for selection of candidate metals and consisted of choosing single metals with desirable work function values to obtain a range of work function values then referring to phase diagrams for the binary metals chosen. Phase diagrams mapped where stable phases existed in the alloys and at what elemental compositions which aided in determining feasible composition ranges. Targeted alloys composed of Au, Ag, Pt, and Mg were chosen with the aim of yielding stable alloys while still allowing for a difference in work functions across the spectrum of compositions. Important considerations, including thermal and mechanical effects such as contact asperities, were reviewed to help mitigate any issues that may arise due to those factors. Single metals were first characterized to obtain deposition rates used in determining ideal co-sputtering deposition rates.

In support of this research, various compositions of single-metal and binary-metal sputtered thin films were investigated for use as potential contact metals. Thin metal films were deposited onto tungsten probes to provide mechanical contacts of varying metallic composition. Metal contacts were also deposited to the surface of hydrothermally synthesized UO_2 samples provided by the Air Force Research Laboratory. Both were examined through I-V analysis where a comparative study utilizing the deposited and mechanical contacts on the UO_2

surface was performed on the samples. UO_2 samples were reportedly of n-type, with (100) and (111) lattice orientation however no electrical characterization or crystallographic evidence is provided as a part of this research. Analysis of deposited contacts determined that Ag functioned optimally on both samples, although other metals proved to form functional junctions with the substrate. Analysis of mechanical contacts to the UO_2 surface identifying Al, Au, and Ag on the (100) sample and Pt, Ag, and Al on the (111) sample as forming optimal contacts without consideration of proper surface adhesion.

Important observations and trends were discovered through other experimentation and analysis such as: the effects of rapid-thermal annealing treatments on work function, the effects of film composition and thickness on work function, and trends in the maximum current of I-V plots across repeated runs. It was found that rapid-thermal annealing treatments probably had some effect on measured work function but larger sample sizes were required to determine statistical significance. Au-Mg binary metal-films of increasing Mg content were studied and shown to decrease in measured work function up to ∼90% Mg content with measured work function values ranging from 4.83 eV to 3.21 eV on Si substrates and 4.59 eV to 3.05 eV on tungsten probes. Pt Films of increasing thickness were found to increase in work function, effectively "masking" the tungsten probes on which they were deposited with thicknesses of 55 nm or greater. Trends in maximum current of repeated I-V measurements revealed there may be some charging at/changing of the junction taking place with subsequent runs. Additionally, I-V measurements using binary-sputtered probes of known work function values were used to effectively show changes in barrier height within the junctions of the UO_2 samples studied. Lastly, plots of work function versus max current (I_{MAX}) through the junction showed unexpected results based on expected

behavior, leading to the assumption that the UO_2 samples used throughout this study likely are not true semiconductors.

Acknowledgements

First, I would like to thank my loving and supportive wife and my son for keeping me motivated to finish strong. Without you, none of this would have been possible. To the staff at AFIT (Maj Laurvick, Maj Herr, Dr. Peterson) for your unending support in accomplishing my thesis work, providing sanity checks, and lending an open ear when needed. To my fellow students (you know who you are) for all your help along the way and providing levity when needed. To the lab technicians (Adam Fritzsche, Rich Johnston, Greg Smith) for providing assistance and fixing issues in a timely manner. Lastly, to my parents for instilling in me a work ethic and giving me encouragement along the way.

Tory E. Robinson

Table of Contents

Page

Abstract . . . iv

Acknowledgements . . . vii

List of Figures . . . x

List of Tables . . . xiii

I. Introduction . . . 1

1.1 Motivation . . . 1
1.2 Research Objective and Overview . . . 2

II. Background . . . 4

2.1 Chapter Overview . . . 4
2.2 Semiconductor Physics . . . 4
2.3 Metal-Semiconductor Junction . . . 11
2.4 Current Transport Mechanisms for Metal-Semiconductor Contacts . . . 16
2.5 Metal-Oxide-Semiconductor System . . . 19
2.6 Important Considerations Regarding Contacts . . . 22
2.7 Uranium Dioxide . . . 24
2.7.1 Atomic Structure, Material and Electrical Characterization . . . 24
2.7.2 Electronic Band Structure . . . 28

III. Experiment . . . 31

3.1 Selection of Candidate Metals . . . 32
3.2 Metallization . . . 35
3.3 Energy Dispersive Spectroscopy . . . 38
3.4 Work Function Measurements . . . 39
3.5 Rapid Thermal Annealing Treatments . . . 42
3.6 Current Versus Voltage Measurements . . . 44
3.6.1 Bulk I-V Measurements . . . 45
3.6.2 Contact-to-Contact I-V Measurements . . . 46
3.6.3 Bulk Probe I-V Measurements . . . 47
3.6.4 Ideal Metal-Schottky Diode I-V Curve Fitting . . . 48

Page

IV. Results and Analysis 50

4.1 EDS Measurements 50
4.2 Work Function Measurements 51
4.2.1 Single-Metal Measured Values 51
4.2.2 Co-Sputtered Metal Measured Values 53
4.2.3 Work Function Dependence on Film Thickness 55
4.2.4 Work Function Dependence on RTA Treatments 56
4.3 I-V Measurements 58
4.3.1 Bulk I-V Plots 59
4.3.2 Contact-to-Contact I-V Plots 63
4.3.3 Bulk Probe I-V Plots 66
4.3.3.1 Single-Metal Probes 66
4.3.3.2 Binary-Metal Probes 68
4.3.4 Single-Metal Bulk Versus Bulk Probe I-V Plots 70
4.3.5 Effects of Contact Area 71
4.3.6 I-V Curve Fitting 73
4.4 Max Current Versus Work Function 74

V. Conclusion 76

5.1 Summary of Findings 76
5.1.1 Effective Contact Metals 76
5.1.2 Important Observations/Trends 78
5.2 Future Work 80

Appendix A. 82

1.1 Alloy Phase Diagrams 82
1.2 Fission Cross-Section of Elements 85
1.3 Single-Metal and Alloy Sputter Settings 86
1.4 Current-Voltage Measurement Plots 87

Appendix B. I-V Curve Fitting Code 93

Bibliography 95

List of Figures

Figure | Page

1 Energy band diagrams 5

2 Semiconductor band structure formation 6

3 Doping effects on density of states 7

4 Impurity/dopant effects on mobility and resistivity 9

5 Electron concentration versus temperature 10

6 Effects of temperature on electron and hole mobility 11

7 Ideal individual energy band diagrams of metal and semiconductor 13

8 Ideal energy band diagram of metal-semiconductor junction 13

9 Ideal energy band diagram of metal-semiconductor junction under bias 14

10 Ohmic/blocking metal-semiconductor junction conditions 15

11 I-V curve depicting ohmic and Schottky behavior 16

12 Current transport in MS junctions 18

13 Ideal individual energy band diagrams of metal, oxide, and semiconductor 19

14 Ideal MOS energy band diagram 20

15 Ideal MOS energy band diagram under flat-band bias 21

16 Two surfaces with asperities making contact 23

17 Contact asperities as an effective radius 24

18 Unit cell of fluorite-structured UO_2 25

19 Mott-Hubbard insulator energy band diagram 29

20 UO_2 density of states 30

Figure		Page

21 DC magnetron sputtering process . . . 36

22 UO_2 contact layout . . . 37

23 As-deposited metal contacts on UO_2 . . . 38

24 EDS spectrum . . . 39

25 KPFM tip/sample model and equivalent circuit . . . 39

26 AM-KPFM process . . . 41

27 Bulk (I-V) profile . . . 45

28 Contact-to-contact (I-V) profile . . . 46

29 Bulk (I-V) profile . . . 47

30 MS diode FB fitting region . . . 49

31 Work function versus Au-Mg content on Si . . . 54

32 Work function versus Au-Mg content on probes . . . 55

33 Pt film thickness versus work function . . . 56

34 Half-normal effects plot for RTA factors . . . 57

35 Bulk I-V summary plot (100) . . . 60

36 Bulk I-V summary plot (111) . . . 61

37 Max current versus run number: bulk I-V. . . . 62

38 Contact-to-contact I-V summary plot (100) . . . 63

39 Contact-to-contact I-V summary plot (111) . . . 64

40 Max current versus run number: contact-to-contact. . . . 65

41 Single-metal bulk probe I-V summary plots . . . 67

42 Max current versus run number: single-metal bulk probe. . . . 68

43 Binary-metal bulk probe I-V summary plots . . . 69

Figure | Page

44 Max current versus run number: binary-metal bulk probe. 69

45 Single-metal bulk versus bulk probe I-V summary plots 71

46 Single-metal bulk versus bulk probe J-V summary plots 73

47 Bulk I-V MS curve fit plots (100) 74

48 Max current versus work function plots 75

49 Gold-platinum phase diagram 82

50 Gold-silver phase diagram 82

51 Gold-palladium phase diagram 83

52 Gold-magnesium phase diagram 83

53 Silver-magnesium phase diagram 84

54 Fission cross-section of elements 85

55 Bulk I-V plot for (100) UO_2 sample 87

56 Bulk I-V plot for (111) UO_2 sample 88

57 Bulk probe I-V plot for (100) UO_2 sample 89

58 Bulk probe I-V plot for (111) UO_2 sample 90

59 Contact-to-contact I-V plot for (100) UO_2 sample 91

60 Contact-to-contact I-V plot for (111) UO_2 sample 92

List of Tables

Table		Page
1	MOS surface charge conditions	22
2	Candidate metals for electrical contacts	27
3	Known work function values for candidate metals	33
4	High and low RTA factor settings	43
5	EDS-measured elemental composition for co-sputtered alloys	50
6	Single-metal work function values	52
7	Co-sputtered metal work function values	53
8	Pt film thickness versus work function	55
9	RTA treatments and results	57
10	Deposition power and rate for single-metal films	86
11	Deposition power and rate for co-sputtered alloy films	86

CHARACTERIZATION OF METAL CONTACTS ON HYDROTHERMALLY SYNTHESIZED URANIUM DIOXIDE FOR NOVEL SEMICONDUCTOR APPLICATIONS

I. Introduction

1.1 Motivation

The ability to effectively track and identify a nuclear detonation (NUDET) around the world is paramount to ensuring nuclear treaty compliance together with sustaining national security. Although several means of nuclear detection currently exist such as seismic, hydroacoustic, and electromagnetic pulse detection, research into additional means of verifying NUDETs is always of great interest. One such method being investigated currently is that of solid-state neutron detection, specifically through use of neutron-sensitive materials such as uranium (U) and thorium (Th) [1]. Solid-state neutron detectors offer several advantages over current detection methods such as smaller footprint and lower energy consumption and garner much attention with respect to space-based applications despite requiring further work to attain comparable detection efficiency of legacy devices [2]. Though research in solid-state detectors using semiconducting conversion layers made of materials such as boron (B) have been conducted [3, 4], uranium-based detectors could offer significant advantages with regard to improved energy output and fission cross section as outlined in Figure 54 within Appendix 1.2 [5].

There has been much interest in utilizing actinide oxides, specifically urania and thoria oxides, to create neutron detection mediums as they show great potential in

their ability to produce secondary ionization and therefore a detection signal when hit with neutrons of desired energy levels [2, 6, 7, 8]. One limit to using actinide materials is the electronic quality and availability of said materials. Researchers at the Air Force Research Laboratories (AFRL) claim to have created a novel process to effectively and repeatedly grow samples of uranium dioxide (UO_2) through hydrothermal synthesization. Though the process has been proven repeatable, the question of electronic quality and the viability of samples as a true semiconductor material are still unknown despite ongoing research. A good first step in analyzing samples of UO_2 would be to establish quality electrical contacts to the surface of the substrate. While much is known in this area with regard to traditional semiconductor materials such as silicon (Si) or germanium (Ge), there is little research into what materials and processes form effective electrical contacts on UO_2 substrates.

1.2 Research Objective and Overview

The primary objective of this research was to establish processes to determine what metals could be deposited onto UO_2 samples to serve as electrical contacts. This would allow further work into determining its electronic properties and ultimately its potential for use in creating solid-state devices. In facilitating this primary objective, samples of hydrothermally grown UO_2 were systematically studied and used to answer the following questions:

1. Do any of the contact metals tested prove to form adequate ohmic electrical junctions with the samples tested?

2. Were any important trends in the data collected deemed important or provided useful information with regard to device fabrication?

Two samples of UO_2 were provided by AFRL for analysis and were reportedly of n-type with crystal faces of (111) and (100). Several metal contacts were deposited on the samples through direct-current magnetron sputtering (DCMS) which allowed for analysis through current-voltage (I-V) measurements. Tungsten probes were coated with single and binary-metals through DCMS which allowed for a comparative analysis between contacts deposited to the surface of the UO_2 samples and mechanical contacts made to the surface with metal-sputtered probes. Efforts were made to establish binary-metal sputtered probes of varying compositions to attain a range of work function values. These probes allowed for a narrow look at the effect of work function on barrier height within junctions made between the metal probes and the UO_2 substrate.

II. Background

2.1 Chapter Overview

The purpose of this chapter is to provide a fundamental understanding of the semiconductor physics that apply to metal-semiconductor (MS) junctions and to the metal-oxide-semiconductor (MOS) system that is used widely in integrated circuit design today. Current transport mechanisms in MS contacts, in addition to some important considerations with regard to these contacts, and relevant work/characteristics with respect to the UO_2 samples used throughout this study are reviewed. These concepts and information were utilized to provide a better understanding of the work that has been accomplished with respect to using uranium oxides to develop semiconductor devices and serves as a basis for future use in developing solid-state neutron detectors.

2.2 Semiconductor Physics

An important aspect to first consider when explaining the functionality behind semiconductor devices is how the materials differ from one another. Figure 1 [9] depicts the relationship from an energy band diagram perspective. The figure is pictured assuming these materials are sufficiently separated from one another, are intrinsic or free from defects, there is no applied bias, and are at room temperature. Metals are inherently the most conductive material. This is conveyed by means of the overlapping valence and conduction bands that yields a non-existent energy band gap (E_g), which is simply the difference between the valence and conduction band edges. The number of free carriers in each band also plays a role in determining a material's conductivity. The semiconductor in Figure 1 has a slightly larger band gap, a mostly filled valence band, and a conduction band with a small

number of electrons which lends it to be semi-conductive. Lastly, the insulator has a large band gap and a full valence band making it electrically non-conductive.

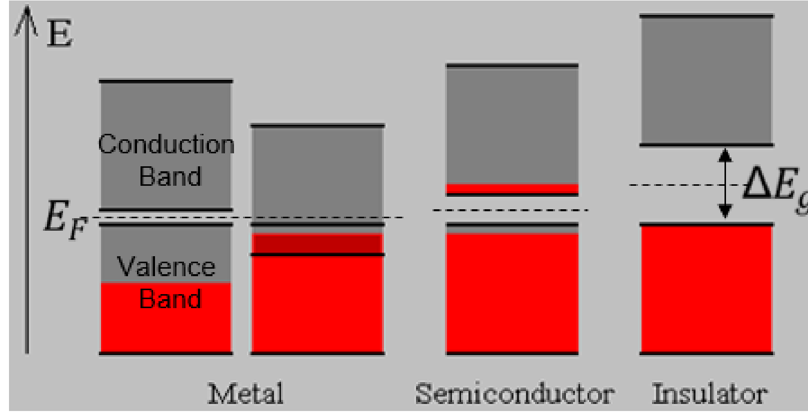

Figure 1. Energy band diagrams for a metal, semiconductor, and insulator [10].

The density of states in the conduction and valence bands, and the probability of a carrier lying in one of these bands dictates a material's ability to transfer electrons between bands. Meaning, the smaller the band gap, the larger the density of states and the higher the probability of an electron being in one of those bands, the more conductive the material. The relationship in a semiconductor between density of states $g(E)$, the probability of an electron filling one of those states $f_D(E)$, and the reference energy level E_f (Fermi energy level) is depicted in Figure 2 [11]. The graph in Figure 2(a) is plotted in accordance with the Fermi-Dirac distribution function which has the form:

$$f_D(E) = \frac{1}{(1 + exp[(E - E_f)/kT]} \tag{1}$$

and is known as the Fermi function. E_f is the Fermi level, k is Boltzmann's constant and T is temperature in degrees Kelvin. Figure 2(b) depicts the density of allowed states in the valence and conduction bands and shows the absence of allowed states between those two bands, this region is known as the forbidden energy band gap (E_g).

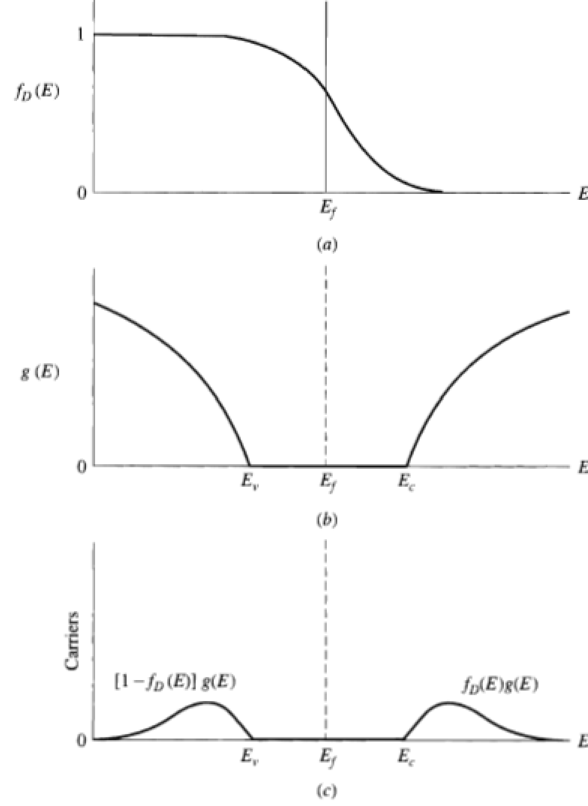

Figure 2. (a) Fermi-Dirac probability distribution $f_D(E)$. (b) The density of allowed states $g(E)$. (c) Product of $f_D(E)$ and $g(E)$ [12].

Figure 2(c) shows the product of the Fermi function and the density of states $g(E)$ and is representative of the density of carriers in the valence and conduction bands in an intrinsic semiconductor. The density of electrons, n, in the conduction band can be calculated by taking the product of $g(E)$ and $f_D(E)$ and integrating over the conduction band as shown in Equation 2 [11]. The same can be done for density of holes,p, in the valence band by taking the product of $g(E)$ and $1 - f_D(E)$ and integrating over the valence band as shown in Equation 3 [11].

$$n = \int_{cb} g(E) f_D(E) \tag{2}$$

$$p = \int_{vb} g(E)[1 - f_D(E)] \tag{3}$$

Another aspect to consider with regard to semiconductor device physics is that of doping or impurities within the substrate. Up to this point, the semiconductor has been considered free of impurities (intrinsic), at thermal equilibrium and without applied bias.

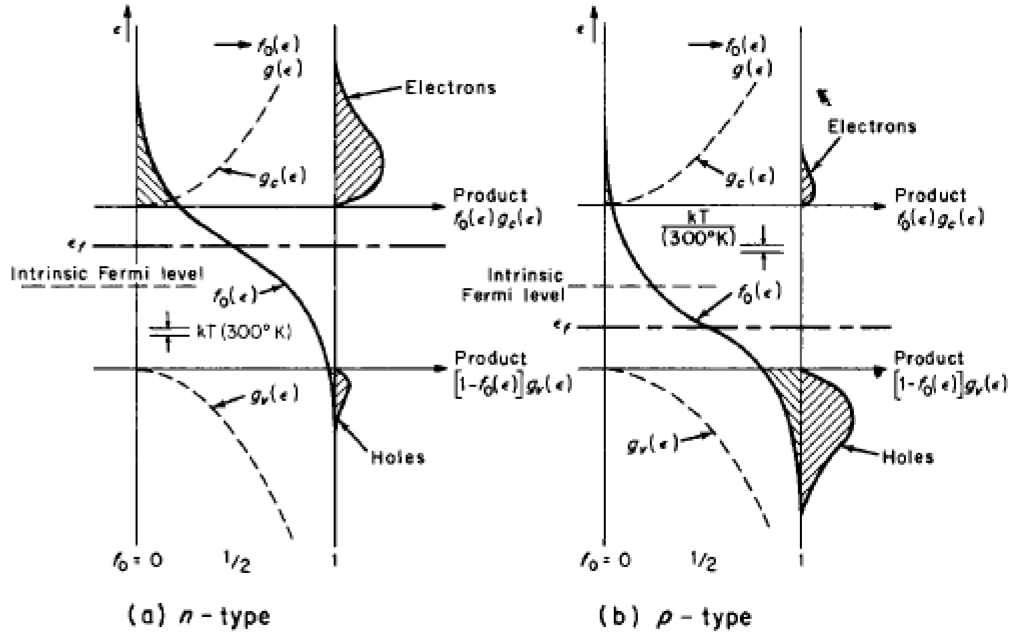

Figure 3. Fermi function overlaid on the density of states function to show the effects of (a) n-type doping and (b) p-type on the densities of holes and electrons within the valence and conduction bands of a semiconductor [9].

The effect of adding donor or acceptor atoms within a substrate is considered doping and is defined as n-type and p-type dopant respectively. This can be seen visually in Figure 3 where the Fermi function, density of states, and the product of the two have been graphed to show the effect that n-type and p-type doping has on the semiconductor [12]. In Figure 3(a) it can be seen that adding n-type dopant to an intrinsic semiconductor results in the Fermi level shifting upward away from the intrinsic Fermi level and towards the conduction band which shifts with it the Fermi-Dirac distribution, thereby increasing the density of electrons in the conduction band. Likewise, p-type doping shifts the Fermi level downward away

from the intrinsic Fermi level and toward the valence band which increases the density of holes within the valence band. This concept is important as doping and impurities within semiconductor devices enable their core functionality. Namely, an intrinsic semiconductor can be made to excite electrons from the valence to the conduction band but it can be very difficult, especially at ambient temperatures, and even then, not efficiently enough for desired performance. The two main performance driven effects of doping a semiconductor are that of electron (μ_n) and hole (μ_p) mobilities and resistivity (ρ) within the semiconductor. Electron and hole mobilities characterize how quickly electrons and holes travel through a substrate when driven by an applied electric field. Resistivity relates directly to resistance (R) within a thin film according to Equations 4 and 5,

$$\rho = \frac{1}{\sigma} = \frac{1}{q(\mu_n n + \mu_p p)} \tag{4}$$

$$R = \frac{\rho}{t} * \frac{W}{L} \tag{5}$$

where σ is the conductivity, W the width, and L the length of a rectangular piece of material with thickness t [4]. Doping leads to decreased resistivity/increased conductivity but also leads to decreased mobilities, where p-type decreases hole mobility and n-type decreases electron mobility. The relationship between mobility and impurity concentration can be seen in Figure 4(a). The relationship between resistivity and varying dopant density/type in silicon can be seen in Figure 4(b). Depending on device functionality, resistivity and mobility can play a large part in either helping or hindering device performance. Although doping is limited by the densities of states at the edges of the valence and conduction band edges, denoted N_V and N_C, typically doping is implemented in orders of magnitude less than that. Doping to N_V or N_C is commonly known as degenerately doping and leads to a

more metal-like energy band distribution, yielding a material that functions more like a metal but with a much higher resistivity in comparison.

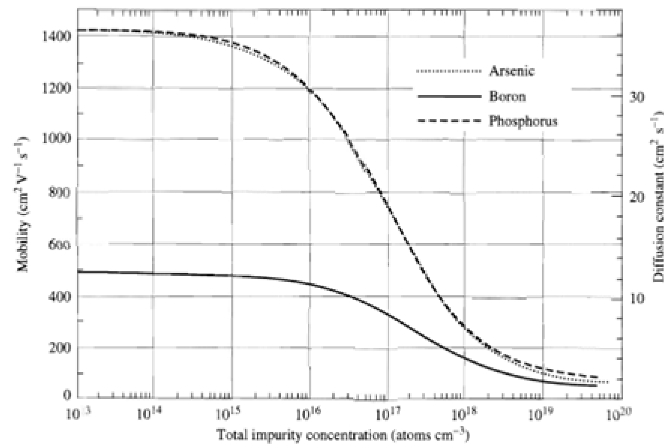

(a) Electron and hole mobilities versus total impurity concentration within silicon at $300° K$.

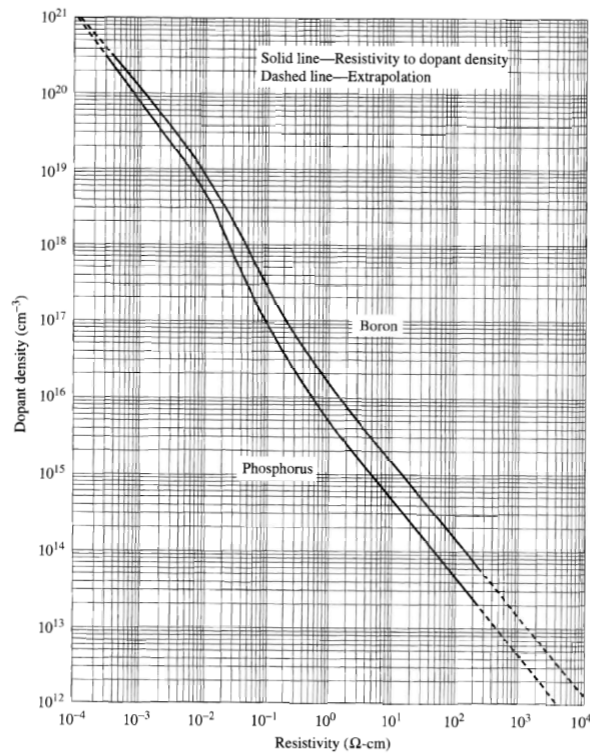

(b) Dopant density within silicon at $300° K$ doped with boron and phosphorous.

Figure 4. Impurity/dopant effects on mobility and resistivity [11].

The effects of temperature and of photons on semiconductor functionality are

important conditions to examine. Temperature's effect is plainly seen in Equation 1, where an increase in temperature leads to an increase in $f_D(E)$ directly affecting Equations 2 and 3. This shows that an increase in temperature will lead to an increase in electron concentration in the conduction band or hole concentration in the valence band. The dependence of electron concentration on temperature is illustrated in Figure 5 [11]. For most device applications, operation in the linear regions on the graph is desirable as constant electron concentration translates into stable and predictable behavior. In this particular case, this translates to operating between 150°K- 550°K for silicon and between 75°K - 275°K for germanium.

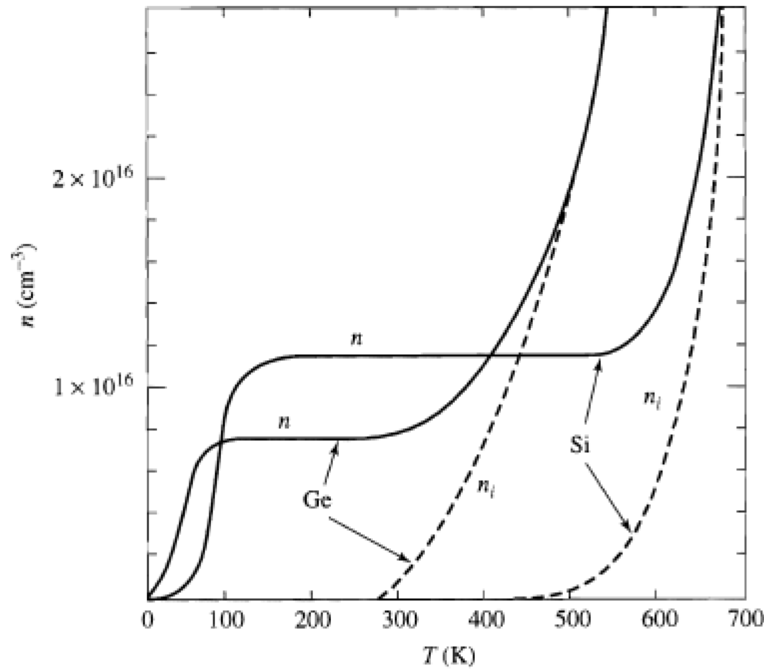

Figure 5. Electron concentration versus temperature for n-type silicon and germanium. Solid lines represent n-type and dashed lines intrinsic electron concentrations for each of the substrates [11].

Electron and hole mobilities are also very dependent on temperature, which are portrayed in Figure 6 [11], where the solid lines represent the electron concentrations of n-type Ge and Si and the dashed lines represent the electron concentrations of intrinsic Ge and Si. Photoconduction can have a similar effect on

electron concentration as incident photons can cause electrons to be excited into the conduction band. This event relies on the photon to be of equal or greater energy as compared to the energy band gap of the material absorbing the photons. In silicon, this requires a photon energy of approximately 1.1 eV which correlates to a photon in the far infrared regime.

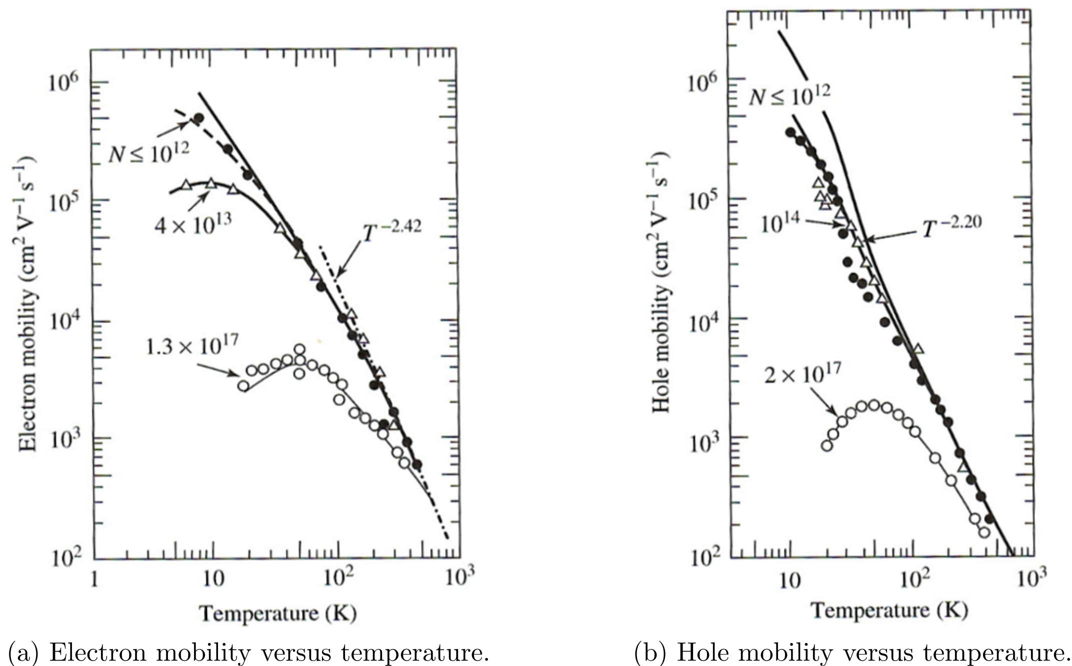

(a) Electron mobility versus temperature.

(b) Hole mobility versus temperature.

Figure 6. Effects of temperature on electron and hole mobility in Si [11].

Lastly, velocity limitations with respect to mobile carrier motion is taken into account. The net carrier velocity with an applied bias is known as the drift velocity. Drift velocity is linearly dependent on the field strength and dictates the speed at which holes and electrons are able to move through a semiconductor under an applied field. Drift velocity reaches saturation at around $10^7 cm/s$ in silicon [11].

2.3 Metal-Semiconductor Junction

This section will look at the interaction between a metal and semiconductor when brought into intimate contact. Standalone behavior still applies and all the

guiding physics are still valid, despite this, the results of creating a metal-semiconductor (MS) junction are unique. A good starting point for this topic involves looking at the ideal energy band diagram shown in Figure 7 which shows the energy bands of gold and an n-type silicon substrate [11]. One important item to note is that both materials have different Fermi levels that are independent of one another, indicating that these two materials are not in physical contact with one another.

E_0 is simply a reference energy level, much like E_f, and corresponds to the energy of free space and is often referred to as the vacuum energy level. It is useful in describing the work functions of the metal and semiconductor Φ_M and Φ_S, which are simply the difference in the Fermi level and the vacuum level as depicted in Figure 7. Physically, Φ can be defined as the thermodynamic work required to move an electron from the vacuum just outside of a material to within it, where the electron goes to the Fermi level on average. The electron affinity, χ, can be described as the energy obtained by moving an electron from the vacuum just outside of a material to the bottom of the conduction band just inside the material. The work function of metal is considered constant and is dependent on the type of metal being looked at, whereas the work function of the semiconductor is highly dependent on the type and level of impurities present in the material. The electron affinity, χ, is considered a constant of the semiconductor as it ideally does not change with doping and is calculated as the difference between the vacuum level E_0 and conduction band edge E_C.

When bringing these two materials in contact with one another, certain interactions take place to form the junction and the corresponding energy band diagram can be depicted as in Figure 8 [11]. It is important to note that the silicon is n-type and the work function of the metal is larger than that of the semiconductor

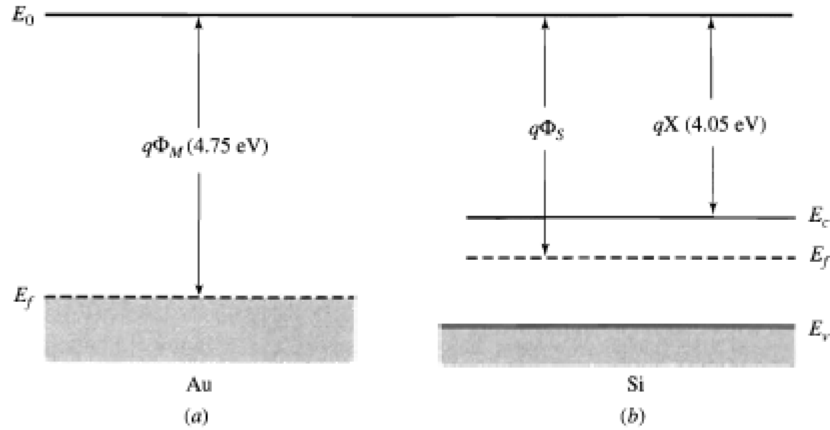

Figure 7. Ideal individual energy band diagrams for gold (a) and silicon (b) with continuous vacuum level E_0 [11].

as this will ultimately dictate the behavior of the band diagram and is essential to the explanation of the junction formation. Variations of those parameters will yield different behavior of this junction which will be discussed in further depth later.

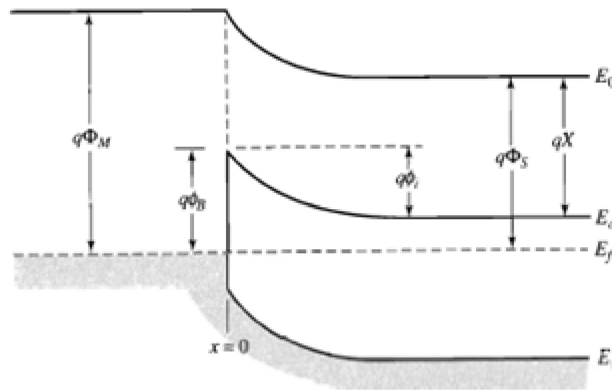

Figure 8. Ideal energy band diagram of metal-semiconductor junction between gold and n-type silicon [11].

When contact between the metal and semiconductor is first accomplished, there is a flow of electrons from semiconductor to metal until they reach equilibrium, resulting in a single Fermi level and positive charge of semiconductor with respect to the metal. This, along with the difference in the work function of the metal and electron affinity in the semiconductor cause an electrical barrier to form at the junction, the height of which can be calculated according to Equation 6 for a n-type

(Φ_{Bn}) semiconductor and Equation 7 for a p-type (Φ_{Bp}) [11].

$$\Phi_{Bn} = \Phi_M - \chi \tag{6}$$

$$\Phi_{Bp} = E_g + \chi - \Phi_M \tag{7}$$

While Figure 8 is at equilibrium and has no applied bias, it is important to consider the effects on the energy band diagram of an applied forward and reverse bias. Common convention dictates Forward bias (FB) being defined as a positive charge being placed on the metal and negative charge on the semiconductor ($V_a > 0$). Reverse bias (RB) being defined as the opposite of forward ($V_a < 0$). An applied FB causes a decrease in the voltage drop across the space charge region in the semiconductor, causing the barrier height to decrease. An applied RB causes an increase in the voltage drop across the space charge region in the semiconductor, causing the barrier height to increase. This is depicted visually in Figure 9 [11].

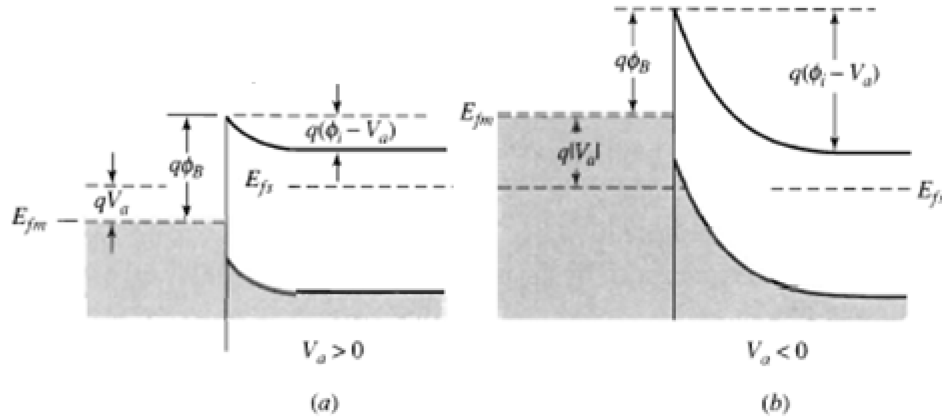

Figure 9. Ideal energy band diagram of metal-semiconductor junction under an applied forward (a) and reverse (b) bias [11].

This functionality is the basis of the design of MS junction devices and, as previously stated, changes with p/n-type substrates and differences in the work functions of the metal and electron affinity of the semiconductor. The effect on the

band diagram due to these differences is outlined in Figure 10 [11]. In an n-type semiconductor, when $\Phi_S < \Phi_M$, the result is a blocking or barrier effect which allows current easily in one direction and not the other. These devices are widely known as Schottky barriers or diodes after Walter Schottky due to his contributions in this field of study. When $\Phi_S > \Phi_M$, the result is an ohmic contact, which has a linear behavior that follows Ohm's law, and allows current to flow easily in both directions.

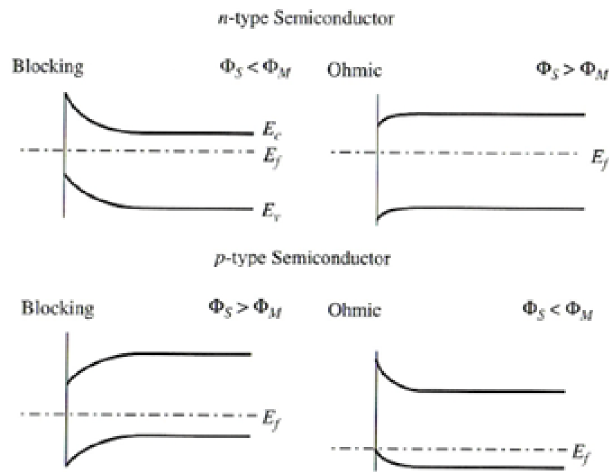

Figure 10. Ideal energy band diagrams of metal-semiconductor junctions depicting conditions required for ohmic and blocking behavior based on n-type and p-type semiconductors[11].

The current versus applied voltage (V_a) is plotted in Figure 11 for an ideal Schottky diode and an ohmic contact and is a good depiction of how these two junctions differ graphically.

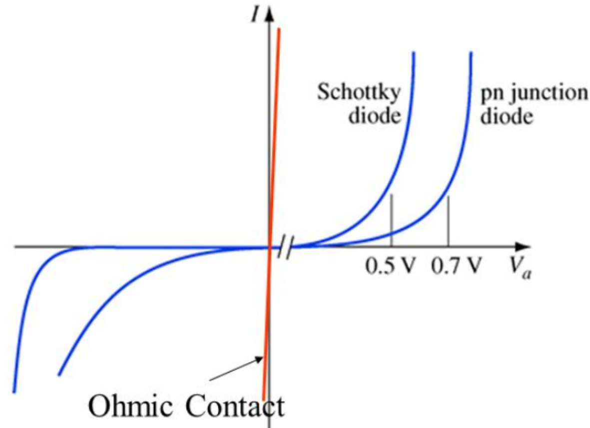

Figure 11. I-V curve for Schottky diode, PN junction diode, and for an ohmic contact.

In an ohmic contact, the current is proportional to the voltage offering a straight-forward interpretation of resistance within the MS junction. A large positive (steeper) slope indicates a lower resistance allowing a larger maximum current through the junction, the reverse can be said of a smaller positive slope. In Schottky junctions, however, voltage is not proportional to current which makes analysis of this relationship less intuitive. Contacts can be, and typically are, some variation between an Ohmic junction and Schottky barrier and often are described as being more or less Schottky/Ohmic in nature.

2.4 Current Transport Mechanisms for Metal-Semiconductor Contacts

The means to which carriers can overcome the potential barrier in a MS junction dictate the device's overall behavior. As depicted in Figure 12 below, the various modes of carrier transport are outlined with their representative I-V curves. As can be seen in Figure 12(a), junctions with low doping, ($< 10^{15} cm^3$ in Si), result in a junction with a very-wide depletion width x_d. Having such a wide depletion width results in carriers having to surmount the junction barrier with an applied bias greater than the built-in barrier. These devices are also known as Schottky or

blocking junctions/diodes, in which the potential barrier occurs due to differences in the work function of the metal and electron affinity of the semiconductor as can be seen in Equations 6 &7 above. The resulting current is given by [13]:

$$I(V_D) = I_S[exp(\frac{qV_D}{nkT}) - 1] \tag{8}$$

$$I_S = A^*T^2exp(-\frac{q\Phi_B}{kT}) \tag{9}$$

$$A^* = (\frac{4\pi qm^*k^2}{h^3}) \tag{10}$$

where k is the Boltzmann constant, h is Planck's constant, T the absolute temperature, A^* the effective Richardson constant, V_D is the voltage drop across the ideal diode, n an ideality factor, q the unit electron charge, m^* the carrier effective mass, and Φ_B the Schottky barrier height. The ideality factor, n, accounts for deviations in ideal Schottky behavior which most diodes exhibit experimentally. The parameter is equal to 1 ideally and increases in value for non-ideal differences in current transport and is predicted to be larger than 1.2 for undoped organic semiconductors [14]. I_S is known as the saturation current and is a small current due to the motion of minority carriers occurring during an applied reverse-bias.

Figure 12 (b) represents a slightly higher doping than that of (a) designated as "medium" doping ($10^{17}cm^3$-$10^{18}cm^3$ in Si) which results in a slightly lower and narrower barrier. In this region, the electrons thermally tunnel through the thin barrier created at the upper end of the conduction band which typically begins to occur when the barrier width is on the order of single-digit nanometers. The behavior begins to deviate from ideal Schottky behavior and gradually becomes more ohmic in nature. As doping increases and the semiconductor becomes very-heavily doped ($> 10^{19}cm^3$ in Si) x_d decreases to a few nanometers allowing carriers to tunnel directly through the barrier. This results in symmetric current

flow in the FB and RB regions forming a junction ohmic in nature without strictly relying on barrier lowering. This process is known as direct tunneling and is accomplished intentionally to avoid interface or surface states from causing a depletion zone in the semiconductor when a metal is brought into contact [15].

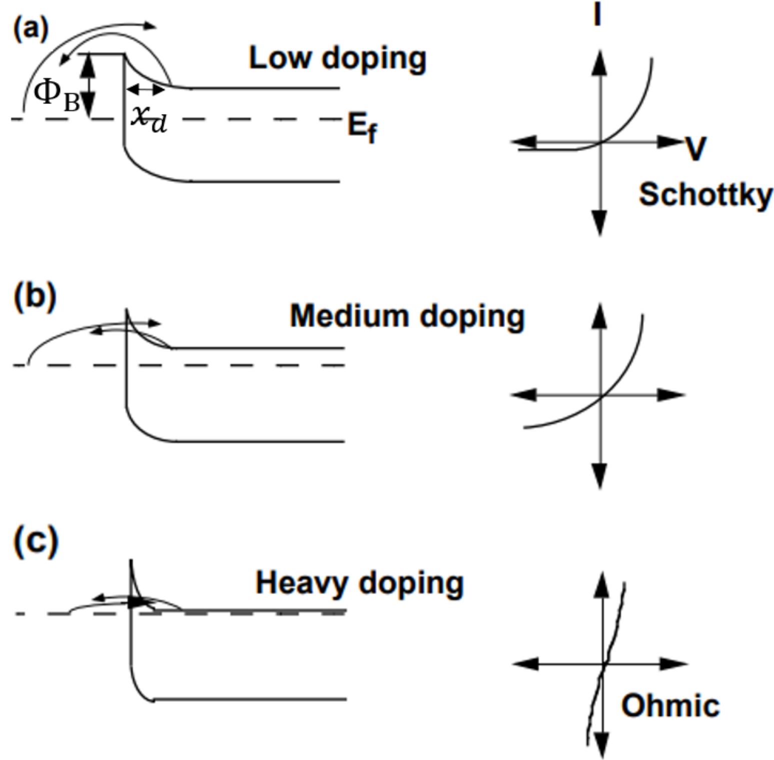

Figure 12. Current transport mechanisms for metal-semiconductor contacts. Metal/n-semiconductor pictured.

Taking the non-ideal diode equation describe previously and defining the voltage drop across the diode (V_D) in terms of the applied voltage (V_a) and current (I) where $V_D = V_a – IR_S$ due to the voltage drop caused by R_S, Equation 8 can now be written in terms of V_a as:

$$I(V_a) = I_S[exp(\frac{q(V_a - IR_S)}{nkT}) - 1] \tag{11}$$

where I_S was previously defined as the saturation current.

2.5 Metal-Oxide-Semiconductor System

Incorporating an oxide layer in between the metal and semiconductor layers of the junction describe in Figure 7, will yield a metal-oxide-semiconductor (MOS) structure. This structure is highly important in IC technology because it allows for the design of much more complex devices using planar silicon technology. The best way to look at the MOS system is by first looking at the energy band diagrams for the individual and joined structures as was done with the MS system. The respective diagrams for these can be seen in Figure 13 and Figure 14[11].

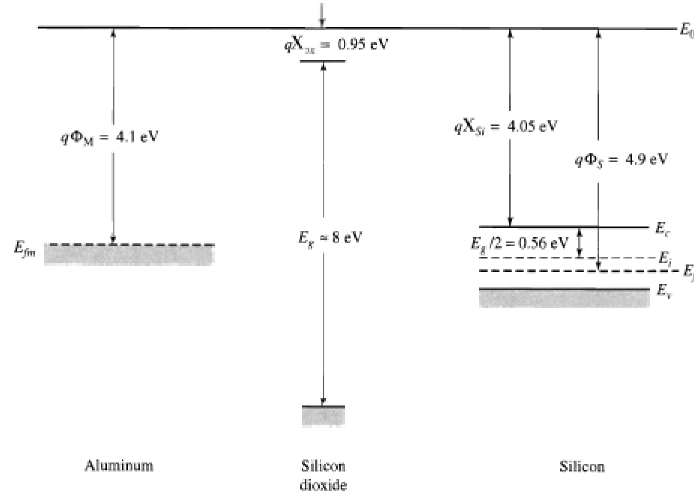

Figure 13. Ideal individual energy band diagrams for aluminum, silicon dioxide, and p-type silicon with continuous vacuum level E_0 [11].

To preface this topic, it is important to note that the silicon is of p-type as this plays a large part in device behavior as it did in the MS junction. In fact, the energy band diagrams under equilibrium are very similar. However, due to the oxide layer, charges do not flow freely between the metal and semiconductor as they did with the MS junction. This oxide region now functions more like a dielectric layer between a capacitor with metal and semiconductor plates. This results in a positive charge at the surface of the metal and negative charge at the surface of the silicon. The energy difference in both materials results in a voltage drop across the oxide

region. The structure now has a continuous Fermi level resulting in the band bending effect seen previously in Figure 8.

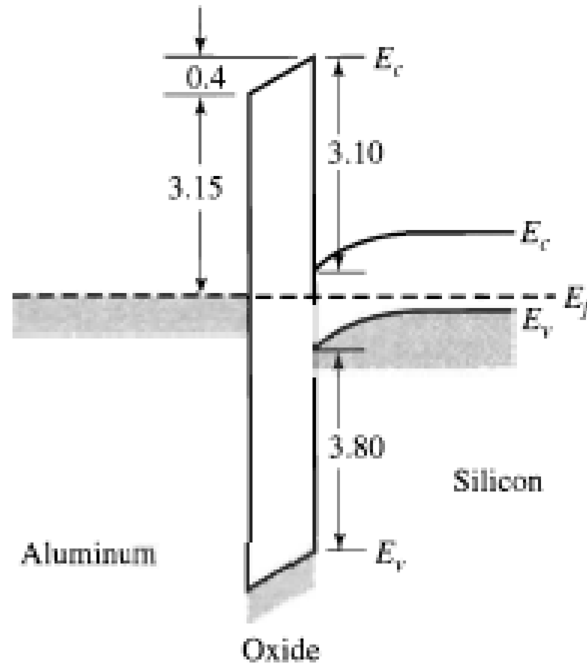

Figure 14. Ideal energy band diagram of MOS junction between aluminum, silicon dioxide, and p-type silicon [11].

By applying a bias between the metal and semiconductor of a MOS structure, a true difference of these devices compared to the MS junction can be seen. These bias voltages with respect to the flat-band voltage of the device ultimately dictate the different modes the MOS junction is operating in. Flat-band voltage (V_{FB}) is simply the difference in the work functions of the metal and semiconductor and characteristic of the flattening/shifting of bands and Fermi levels in the band diagram as can be seen in Figure 15 and calculated in Equation 12 [11].

$$V_{FB} = \Phi_M - \Phi_S \tag{12}$$

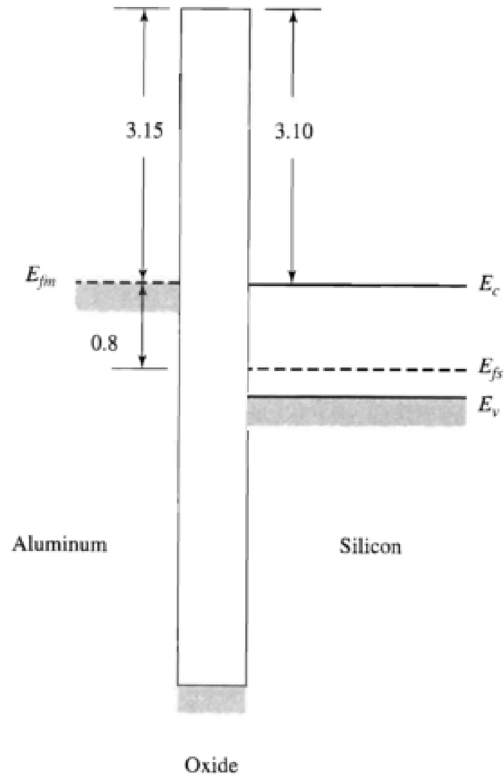

Figure 15. Energy band diagram of MOS junction between aluminum, silicon dioxide, and p-type silicon under flat-band applied bias conditions [11].

The different modes, defined as surface charge conditions, are defined with respect to the flat-band voltage and the voltage applied to the metal gate contact and are functions of the applied gate voltage (V_G) and surface carrier density. The different modes will not be delved into but simply stated as being accumulation, depletion, and inversion. The different modes and required conditions can be seen in Table 1[11].

Table 1. MOS surface charge conditions for p-type silicon [11]

$(V_G - V_{FB})$	ϕ_s	Surface Charge Condition	Surface Carrier Density
Negative	Negative $\|\phi_s\| > \|\phi_p\|$	Accumulation	$p_s > N_a$
0	Negative $\phi_s = \phi_p$	Neutral (Flat-band)	$p_s = N_a$
Positive (small)	Negative $\|\phi_s\| < \|\phi_p\|$	Depletion	$n_i < p_s < N_a$
Positive (larger)	0	Intrinsic	$p_s = n_s = n_i$
Positive (larger)	Positive $\|\phi_s\| < \|\phi_p\|$	Weak inversion	$n_i < n_s < N_a$
Positive (larger)	Positive $\phi_s = -\phi_p$	Onset of strong inversion	$n_s = N_a$
Positive (larger)	Positive $\|\phi_s\| > \|\phi_p\|$	Strong inversion	$n_s > N_a$

2.6 Important Considerations Regarding Contacts

When looking at the contact theory directly applicable to this study, two properties that seemed distinctly important when selecting metals were with respect to thermal and mechanical properties. These are not the only factors that play a substantial role in dictating contact behavior but did appear to be the driving ones with respect to this study. These concepts are looked at further in this section as well as possible strategies to mitigate any problems associated with them. In some cases, heating may have desirable effects as it does in the case of reducing surface roughness whereas in others it may have undesired effects such as varying resistivity and changing the physical structure of the alloys [16]. Acceptable temperature ranges are materially dependent and can vary based on composition of the alloys being looked at. A lot of information can be gained regarding this matter by studying phase diagrams for the alloys and looking at physical properties, such as thermal conductivity of the metals being used to form the alloys. For instance, in [17] it was found that for co-sputtered Au-Pt thin films that although alloys ranging

across all platinum contents were single-phased, they were ultimately metastable and characteristics of the alloys within the miscibility gap changed after being cycled over time. Despite not being directly attributed to heating by the authors, it could easily be theorized that thermal effects could be, at least in part, the cause.

Mechanical effects, more specifically surface roughness, play a large part in dictating contact behavior and performance. Analogous to surface roughness, contact asperities or peaks are problematic because when two surfaces come into contact with one another there are now multiple smaller contacts. This phenomenon is depicted graphically in Figure 16 below which shows a profile view of two surfaces with contact asperities meeting one another with more (bottom) or less (top) force.

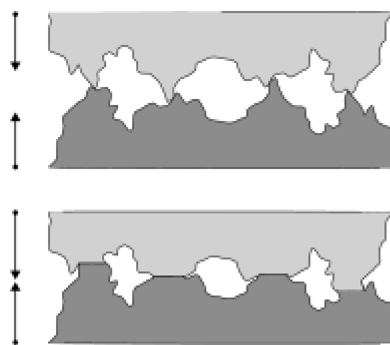

Figure 16. Two surfaces with asperities making contact [18].

Asperities can be problematic in that they provide the only conducting paths for the transfer of electrical current and increase the overall resistance of the contact [19]. Calculating ideal contact resistance, assuming perfectly smooth surfaces and a good ohmic contact, could be done in the same manner as bulk resistance. Equation 13 below can be used to calculate this resistance where ρ_C is the specific contact resistivity of the material and A the surface area of the contact. In practice, contact resistance is generally derived experimentally as it is difficult to accurately derive R_C computationally.

$$R_C = (\frac{\rho_C}{A}) \tag{13}$$

Ideal calculations become less intuitive considering the effects contact asperities introduce. Figure 17 illustrates the effect asperities have on the overall surface area of the contact [19]. The individual peaks of varying radii, or apparent radius (r_a), are transformed into a total effective radius (r_{eff}). Although a seemingly easy concept, the difficulties become inherent when trying to measure r_a or calculate r_{eff} but are only an issue with really small contact areas as variation caused by this effect become negligible with increasing contact area. Aside from constricting electrical paths, it is important to realize that contact asperities also inhibit the ability of the contact region to dissipate heat which can lead to further undesired thermal effects discussed earlier in this section. It is clear now why these asperities should be mitigated as much as possible.

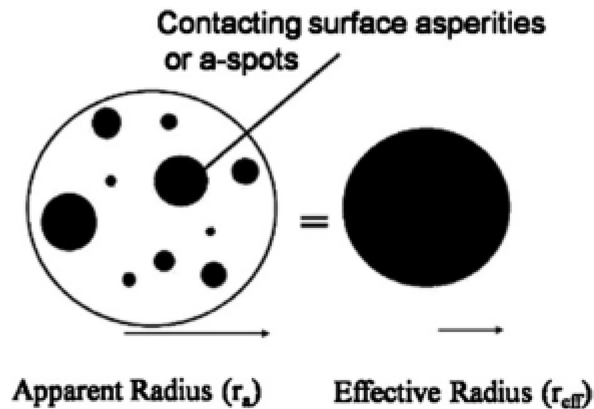

Figure 17. Contact asperities as an effective radius [20].

2.7 Uranium Dioxide

2.7.1 Atomic Structure, Material and Electrical Characterization.

The purpose of this section is to outline basic information about the atomic structure of uranium dioxide (UO_2) and to cover previous work by [21] and [2] on the material and electrical characterization of hydrothermally grown samples of UO_2.

The atomic structure of stoichiometric uranium dioxide can be seen in Figure 18 below and depicts the fluorite crystal structure with oxygen portrayed as the darker simple-cubic (SC) oriented atoms in the center of the unit cell and the uranium atoms (white) being configured in a face-centered cubic (FCC) manner surrounding the SC oxygen atoms. At room temperature, stoichiometric UO_2 is known to have an O/U ratio of 2.000±.001 and a lattice parameter (a_o) of 547.081 ± 0.008 pm [22]. Hydrothermally synthesized UO_2 crystals grown with the same process as those looked at in this study, have a measured lattice parameter of 547.03 ± 0.06 pm and stoichiometry near $UO_{2.003}$ [5].

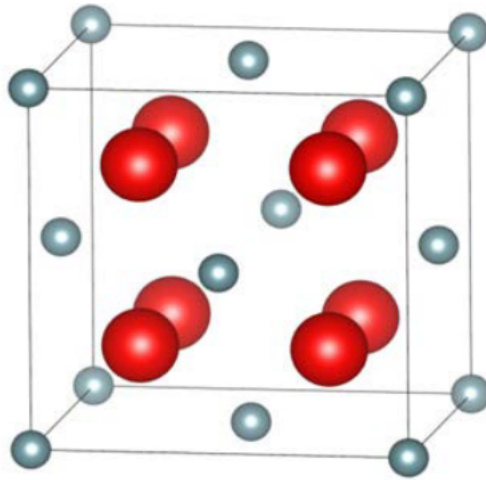

Figure 18. Unit cell of fluorite-structured UO_2. The smaller uranium atoms (grey) are located in the face-centered cubic (FCC) orientation surrounding the larger oxygen atoms (red) oriented in a simple cubic (SC) configuration [2].

Electrical characterization of hydrothermally grown crystals via various techniques provided crucial data in determining contact behavior and analysis of data collected on samples of UO_2 used in this study. In [23] the photoelectric work function, Φ_{PES}, was determined by x-ray photoemission on hydrothermally grown UO_2 samples of (100) and (111) orientation. The measurements took place over a period of time with initial values of 5.56 eV and 5.66 eV for the (100) and (111) samples respectively. Maximum values of the measured work functions were

determined to be those of the stoichiometric UO_2 surfaces at 5.80 eV (100) and 6.28 eV (111) with an associated uncertainty of ± .36 eV. In [21], a study was done on hydrothermally grown s.c. UO_2 to determine the mobility, carrier concentration, and conductivity of the samples. Hall measurements yielded the sample to be n-type with a carrier concentration (n) of $1.68x10^{16} \pm 0.8x10^{16} cm^{-3}$, conductivity ($\sigma$) of $5.7x10^{-3} \pm 0.3x10^{-3} \Omega - cm^{-1}$, and mobility (μ) of $2.5 \pm 1.3 cm^2 * V^{-1} s^{-1}$.

In [2], a contact study was accomplished with the goal of finding suitable metals for making contacts on a UO_2 substrate. It was determined that the best approach was to first look at the work functions of candidate metals, the electronegativity (χ) of UO_2, and the MS junction theory to predict whether candidate metals would form ohmic or Schottky type contacts. Using 2.1 ± .1 eV as the bandgap energy (E_g) of UO_2 [24], the electronegativity was resolved through flat-band approximation to be 4.2 eV (111) and 3.7 eV (100) both with a standard deviation of ± .4 eV. The other factor taken into consideration was that of lattice mismatch between the substrate and contact metal. A candidate was considered suitable if it was within 10% of UO_2's lattice constant of 5.471 Å or sub-lattice cell spacing of 3.87 Å. Metals were also identified as being potentially ohmic or Schottky based on being within 10% of the required work function to establish the respective contact type. The contact metals looked at and information from the previously discussed methodology are contained in Table 2 below where the parenthetical value following the contact type in the two rightmost columns indicates the order of best agreement based on potential barrier as calculated using Equations 6 and 7.

Table 2. Candidate metals for electrical contacts [2].

Candidate Contact Metal	Work Function[+] [eV]	Lattice Constant[++] [Å]	Resistivity @300K, 1 atm[++] [$\times10^{-8}$ Ω m]	UO_2 (111)	UO_2 (100)
Zn	3.63	2.67, 4.95	6.06	Schottky (1)	Schottky (1)
Mg	3.66	3.21, 5.21	4.51	Schottky (2)	Schottky (2)
Cd	4.08	2.98, 5.62	6.80	Schottky (3)	
Cu	4.65	3.61	1.73		Ohmic (1)
Be	4.98	2.29, 3.58	3.76		Ohmic (2)
Co	5.00	2.51, 4.07	5.60	Ohmic (5)	Ohmic (3)
Au	5.10	4.08	2.27	Ohmic (3)	Ohmic (4)
Ni	5.15	3.52	7.20	Ohmic (2)	Ohmic (5)
Pd	5.22	3.89	10.80	Ohmic (1)	
Pt	5.50	3.92	10.80	Ohmic (4)	Schottky (3)

Although data was not provided to solidify the nature of samples UO2-T-152a and UO2-T-64a used in this study, it will be assumed that what was reported to the experimenter of this study is valid. With regard to the crystallographic information, it was reported that the single-crystal (s.c.) nature and orientation of the UO_2 samples were resolved using x-ray diffraction (XRD). Analysis of collected XRD data reportedly showed that sample UO2-T-64a was of (100) crystal orientation and sample UO2-T-152a to be of (111) orientation and further solidified their s.c. nature. Due to the similar growth processes and conditions used, the type and electrical characteristics for the samples outlined earlier in this section were assumed to be representative of those used in this study. Repeatable hall measurements were unable to be conducted as it was assumed to be a result, at least in part, of poor

contacts made to the UO_2 substrate. Any analysis going forward in this document will use these assumptions and samples referred to as (100) and (111) will refer to UO2-T-64a and UO2-T-152a unless specified otherwise. Another important aspect to consider is the formation of oxide layers other than UO_2 known to develop on the surface over time. These oxides, such as U_3O_8, U_3O_7, and U_4O_9, can cause significant changes across the substrate surface as urania oxides' electrical characteristics are known to be highly dependent on the oxide's O/U ratio [25, 26].

2.7.2 Electronic Band Structure.

Despite the convenience of classifying UO_2 as a traditional semiconductor material, there have been many studies that characterize the material as being a $5f$ Mott-Hubbard insulator [27, 28, 29]. Due to differences in electron transport of Mott-Hubbard insulators and the band structure of UO_2, traditional band-theory pertaining to semiconductors cannot be used directly to model it. A useful comparison between Mott-Hubbard insulators and semiconductors can be seen in Figure 19 which depicts the energy band diagram for Mott-Hubbard insulators. Localized density of states are identified as the upper Hubbard band (UHB) and lower Hubbard band (LHB) with energy levels at the edges of these bands being identified as E_u and E_l respectively and the difference in those energy levels being the energy gap (E_g) [30].

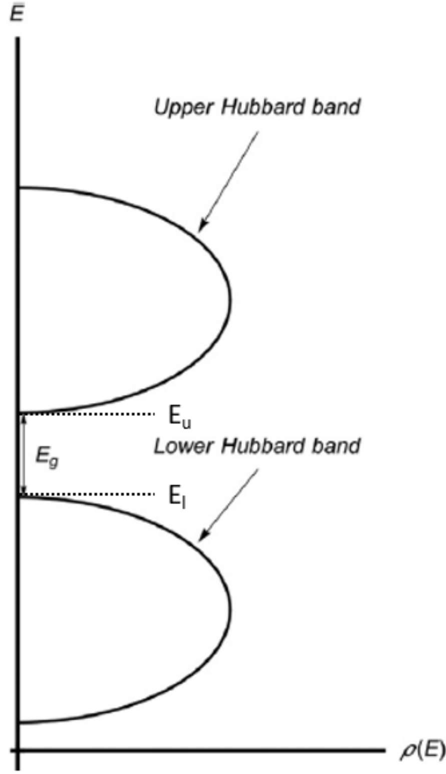

Figure 19. Energy band diagram of a Mott-Hubbard insulator. Adapted from [30].

The electronic band structure of single-crystal UO_2 has been studied extensively and can be seen depicted in Figure 20 below [24]. Localized density of states (DOS) are identified with a large band centered at approximately 5 eV from U $5f$ and U $6d$ contributions, a large band centered at $\sim$-5 eV from O $2p$ contributions, along with a narrow band at $\sim$-1 eV from both O $2p$ and U $5f$ contributions [31]. The previously described band structure designations can be pictured on Figure 20 to show the energy band diagram of UO_2 modeled as a Mott-Hubbard insulator. This translation is straightforward with the edges of the bands, E_l and E_u, existing at either side of ΔE_g however, in the case of UO_2 there exists an interim energy band between the UHB and LHB.

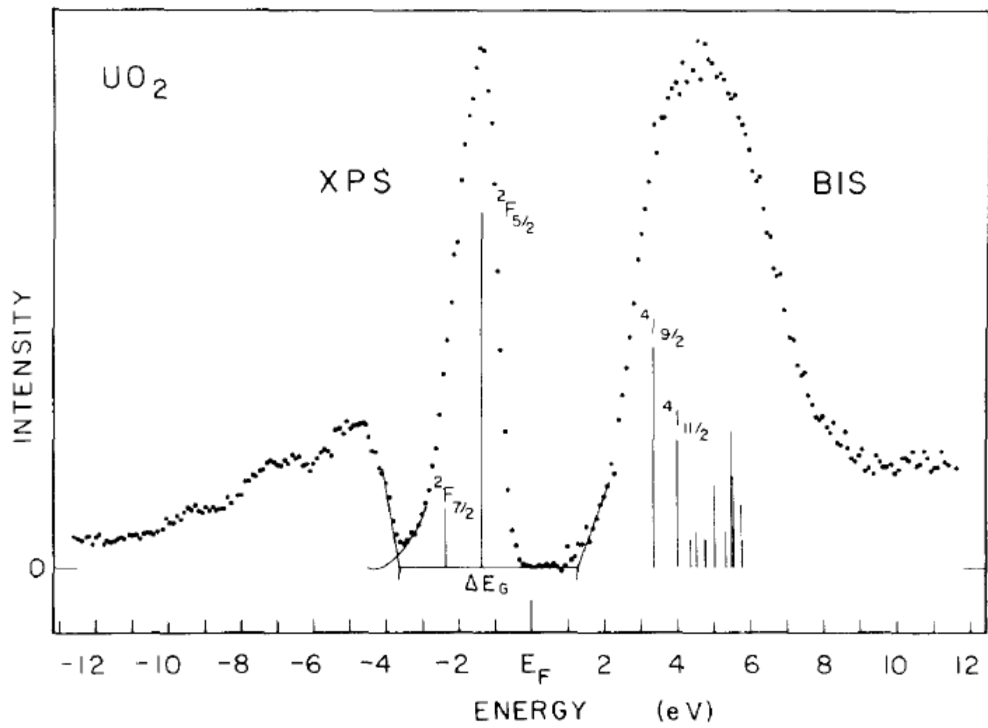

Figure 20. UO_2 **density of states as determined by XPS and BIS [24].**

III. Experiment

The purpose of this section is to describe the processes and techniques employed during experimentation conducted as a part of this study. The overall goal of experimentation was to determine ideal contact metals for use on UO_2 substrate material. There were several steps involved in the experimentation process, a list of the steps and brief overview of these steps in execution order were as follows:

1. Selection of candidate metals to be deposited onto UO_2 samples and tungsten probes - Involved a review of published candidate metals' work function values and phase diagrams for co-sputtered films, leading to the selection of single-metal and binary-metal film compositions to be deposited on the respective substrates.

2. Metallization of probes and UO_2 substrates - Offers an overview of the sputtering processes utilized for both substrates and outlines the deposited contact layout on UO_2 samples.

3. Energy dispersive spectroscopy - Provided quantitative elemental analysis of deposited binary-metal films allowing for confirmation of target compositions.

4. Work function measurements - Walks through the surface work function measurements performed on various single and binary-metal sputtered substrates.

5. Rapid thermal annealing treatments - Looks at the process used to thermally treat sputtered probes and the statistical design used to determine the treatment's effect on work function.

6. Current versus voltage measurements on UO_2 contacts - Covers the different

methods in which I-V measurements were taken on the UO_2 samples that allowed for contact analysis.

Information obtained from the experimentation conducted in this section is novel in approach and could prove to be of great value due to the limited number of studies of this nature pertaining to UO_2. Despite any limitations or specificity to the samples used in this study, the processes and techniques utilized can serve as a template for research going forward.

3.1 Selection of Candidate Metals

The following section outlines the procedure utilized in selecting candidate metals to be co-sputtered on tungsten probes and contact metals to be deposited to UO_2 samples as part of this study and was adapted from a contact study by [32]. The general process followed was: (1) study the known work function values for possible candidate metals, (2) review proposed metals' binary phase diagrams to ensure equilibrium miscibility or stable dual-phase combinations, and (3) determine suitable ratios to obtain desired work function values.

Expected work function values from literature (Φ_{Exp}) for each of the candidate metals is shown in Table 3. Values were obtained from [11],[33],[34], and [35]. Work function values for some elements have a wide range due to varying factors such as the lattice orientation and growth method of samples, as well as measurement techniques and deposition method utilized. An average work function value (Φ_{Avg}) was calculated and included in the table to aid in selecting candidate metals. Once candidate metals were selected, work function values of sputter targets and single-metal sputtered films were measured and used to calculate predicted work function values of co-sputtered films. A look at the effects of deposition thicknesses and annealing treatments on work function values were also briefly investigated with

platinum and gold-platinum coated probes respectively.

Table 3. Known work function values for candidate metals

Element	Φ_{Exp}(eV)	Φ_{Avg}(eV)
Ag	4.0-4.3	4.15
Al	4.06-4.26	4.16
Au	4.75-5.45	4.93
Co	4.4-5.1	4.75
Cu	4.4-4.7	4.55
Mo	4.0-4.75	4.38
Mg	3.66	3.66
Ni	4.5-5.25	4.88
Pd	4.9-5.65	5.28
Pt	5.2-5.8	5.50
W	4.65-5.99	5.32

One important aspect considered was the information obtained from binary alloy phase diagrams. Phase diagrams help to determine where different ratios of metals exist in different states (liquid, solid, hetero/homogeneous) and at what temperatures. Single-phase regions and miscibility gaps can be identified using the phase diagrams. This was an important consideration as single-phase alloys were desired due to their ability to maintain their metal alloy crystal structures at elevated temperatures. If at all possible, miscibility gaps and two-phase regions were avoided to ensure reliable/repeatable deposition and to avoid brittle, highly resistive intermetallic compounds from being formed [36].

Phase diagrams referenced in the following section are located in Figures 49-53 within Appendix A. The gold-platinum phase diagram in Figure 49 shows two stable phases below 1260°C and greater than ~15% Au concentration. Au concentrations below 15% result in single phase Au-Pt alloys. Figure 50 shows the gold-silver phase relationship where single-phase solid solution alloys exist across silver concentrations from 0-100% and the melting point changes from 961.93°C to 1064.43°C respectively. Reviewing the Au-Pd phase diagram in Figure 51, it

appears that concentrations of Pd below 40% and above 60% appear to be relatively stable single-phase alloys with two other miscibility gaps at temperatures between 600°C and 900°C. The Au-Mg and Ag-Mg phase diagrams in Figures 52 and 53 appear to be slightly more convoluted than those previously discussed. There are a range of phases across the Au-Mg spectrum but it appears that stable single-phase alloys occur from ∼35% Au to ∼70% Au concentrations. The melting point of Mg is 650°C which is substantially lower than the other metals looked at in this study. An interesting phenomenon appears to take place at around a 50% Au concentration where the melting point of the alloy rises above both that of Mg and Au at 1150°C. Figure 53 depicts the phase relationship between Ag-Mg alloys and appears to show stable single-phase alloys occurring from ∼30% Mg to ∼75% Mg concentrations. Again, a very similar phenomenon to that of the Au-Mg phase diagram occurs around the 50% Ag concentration where the melting point of the alloy raises abruptly to 820°C then decreases rapidly thereafter.

Taking work function ranges and insight gained from binary phase diagrams into consideration, it seemed reasonable that in order to obtain a range of work function values by varying the ratio of single metals being used to co-sputter that using Au, Pt, Ag, and Mg would be suitable choices. A range of atomic percentages of each of the metals to be co-sputtered were established with possible binary alloy films as follows: Au-30%Ag, Au-60%Ag, Au-10%Pt, Au-30%Pt, Au-75%Pt, Au-35%Mg, and Au-65%Mg. All of the alloys were expected to be single-phased with the exception of the alloys falling within miscibility gaps as identified on their respective phase diagrams. Those falling within miscibility gaps were expected to form stable or metastable dual-phase alloys.

After reviewing candidate metal work function values and the contact study discussed previously in Section 2.7, single metals were chosen for deposition on

n-type UO_2 substrate samples, UO2-T-152a and UO2-T-64a. The metals chosen were as follows: Ag, Al, Au, Pt, and W. The deposition method and related processes are described further in the following section.

3.2 Metallization

As part of the research on metal-thin film work functions, it was necessary to deposit metal on to the different substrates being analyzed. Throughout the course of this research, the method utilized for thin-metal deposition was direct-current magnetron sputtering (DCMS). DCMS is a thin-film physical vapor deposition technique where a target material is bombarded with ionized gas molecules, known as plasma, with sufficient energy to displace clusters of atoms, effectively "sputtering" these atoms off of the target which then condense on the desired substrate and walls of the vacuum chamber [37]. Figure 21 shows the physical configuration of the DCMS hardware and overall sputtering process. Co-sputtering is where two or more target materials are sputtered simultaneously and can be used to produce thin-film alloys or composites.

Single-metal thin films were deposited on silicon substrates, glass slides, and tungsten probes from ≥99.99% pure Ag, Al, Au, Co, Cu, Mg, Mo, Ni, Pt, and W targets in a custom-built Kurt J. Lesker DC magnetron sputtering system. A mass flow regulated argon sputtering pressure of 5 mTorr and substrate rotation speed of 5 RPM was used for all depositions. Substrate materials were 75 mm diameter and 380 µm thick test-grade silicon disc wafers, glass slides, and Signatone SE-20TB tungsten probes. Glass slides measured 1 mm in thickness and approximately 625 mm^2 in surface area. Tungsten probes had a measured tip diameter of 20 µm, shank diameter of 20 mil, and an overall length of 1.25". Substrates were placed on a water-cooled substrate holder without external heating and probes mounted

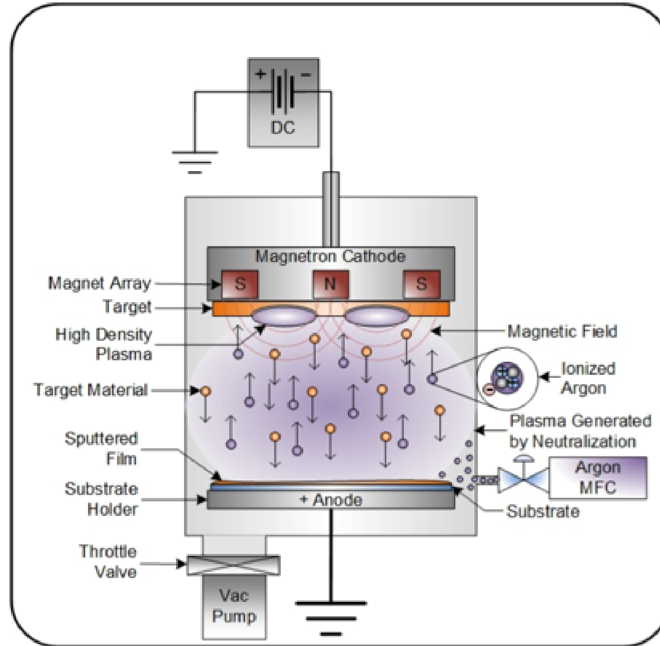

Figure 21. Diagram of DC magnetron sputtering process [38].

vertically in a metal shadow mask to ensure uniform coverage during deposition.

By characterizing single metal deposition first, it allowed for a straight-forward approach for determining ideal power settings to obtain desired ratios for the co-sputtered binary alloys. Depositions were performed at 35, 50, 100, 200, 300, and 350 W forward cathode power settings depending on sputtering target size/composition. Film thicknesses were then measured with a Tencor P-10 surface profilometer and deposition rates were calculated. Single-metal deposition rates based on cathode power are listed in Table 10 in Appendix A. Increased power/decreased deposition times were used only for deposition rate calibration in order to determine optimal sputter powers to obtain desired alloy combinations. This data was then plotted, curve fitted to determine deposition rate vs. cathode power, and used to estimate power levels that would yield desired film thicknesses. Power settings and deposition rates for co-sputtered films are listed in Table 11 in Appendix A. Deposited thicknesses varied between 300 nm – 600 nm for Si wafers,

200 nm – 600 nm for glass slides, and 430 nm – 600 nm for the tungsten probes. Depositions of Pt on tungsten probes were conducted with thicknesses ranging between 55-500 nm in order to determine film thickness' effect on work function.

In order to perform electrical characterization of the UO_2, it was necessary to deposit metal contacts. The DCMS process was used to lay down contact materials of Ag, Al, Au, Pt, and W. To avoid changing any chemical or structural properties of the UO_2 substrate, a process known as shadow masking was used to form uniform contacts and to mask the substrate from being coated in unwanted areas. The desired contact layout to be achieved through shadow masking can be seen in Figure 22.

Figure 22. Diagram of shadow mask contact layout on UO_2.

Nominal contact thickness was 250 nm with a diameter of 200 µm each separated by 500 µm vertical and horizontal distance between contacts. Contacts were laid down in such a manner to allow for current-voltage (I-V) measurements to be performed between like metals and between combinations of the different metals. The as-deposited contacts can be seen in Figure 23. Measured substrate thickness for both samples were 1 mm, a scale is provided as a reference of the overall surface area.

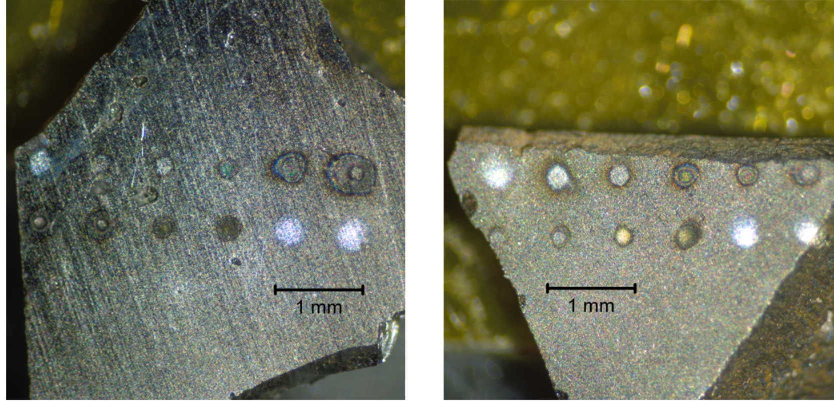

Figure 23. As-deposited metal contacts on UO_2 substrates.

3.3 Energy Dispersive Spectroscopy

Energy dispersive spectroscopy (EDS) is an analytical technique used for chemical or elemental analysis of a sample and is typically utilized in conjunction with a scanning electron microscope (SEM) [39]. Its functionality is based on the fact that each element has a unique atomic structure that corresponds to a unique set of emitted x-ray peaks when bombarded by the electron beam within the SEM. EDS is capable of accurately detecting elements from atomic number Z=4 (Be) to Z=92 (U). The x-ray peaks occur at specific energy levels and are characteristic of the element from which it was emitted. These peaks collected across a range of energies are known as the EDS spectra, an example of this spectra taken on a glass sample containing Si, O, Ca, Al, Fe, and Ba is depicted in Figure 24. When used to perform quantitative analysis, x-ray counts are collected at each characteristic energy level which are used to calculate the concentration of each element within a sample.

For this research, all EDS measurements were conducted in a FEI Quanta 450 SEM equipped with an EDAX EDS system with an acceleration voltage setting of 10 kV and a target working distance of 10 mm.

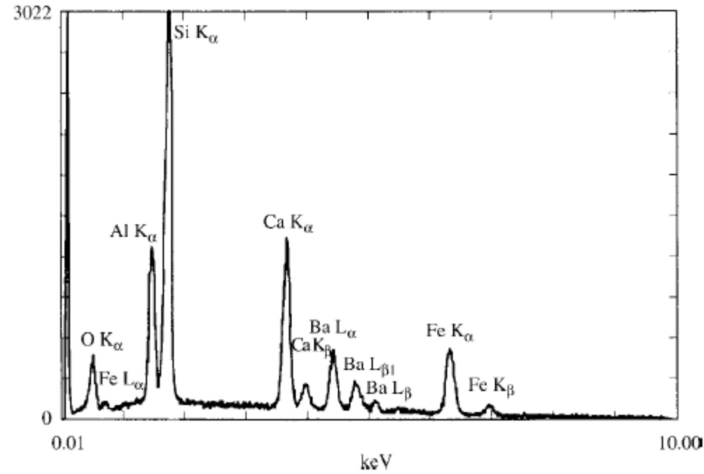

Figure 24. EDS spectrum of glass which includes Si, O, Ca, Al, Fe and Ba [40].

3.4 Work Function Measurements

Kelvin probe force microscopy (KPFM) is an electrical measurement technique that is able to resolve the work function of metal and semiconductor sample surfaces by translating electrostatic forces imposed between a sample and the cantilever tip of an atomic force microscope (AFM) into a contact potential difference (CPD). The overall functionality of the KPFM measurement technique is based on a simple parallel-plate capacitor model as shown in Figure 25 below.

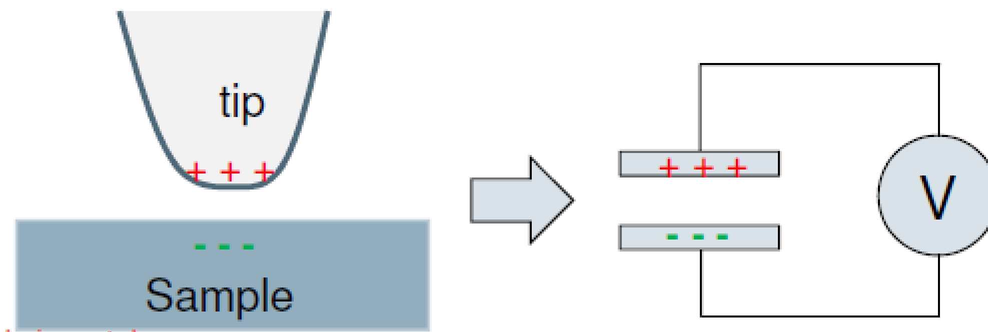

Figure 25. KPFM measurement parallel-plate capacitor model and equivalent circuit [41].

The AFM tip and sample form opposing plates of the capacitor with an air dielectric. Looking at the equivalent circuit, V represents the potential difference

between the CPD (V_{CPD}) and the voltage applied to the tip. The electrostatic force (F_{ES}) between the tip and sample is given by:

$$F_{ES}(z,t) = -\frac{\delta U}{\delta z} = -\frac{1}{2}\frac{\delta C(z)}{\delta z}V^2 \tag{14}$$

where z is the direction normal to the sample surface, U the energy stored in a capacitor, and $\delta C/\delta z$ the gradient of the capacitance between the tip and sample surface. By applying an AC (V_{AC}) voltage to the AFM tip and DC (V_{DC}) voltage to either the AFM tip or sample, V can now be expressed as:

$$V = (V_{DC} \pm V_{CPD}) + V_{AC} sin(\omega t) \tag{15}$$

where ω represents the resonant frequency of the AFM cantilever. By substituting V into Equation 14, Equation 16 below describes the behavior of F_{ES}, the force that causes the tip to oscillate during CPD measurement.

$$F_{ES}(z,t) = -\frac{1}{2}\frac{\partial C(z)}{\partial z}[(V_{DC} \pm V_{CPD}) + V_{AC} sin(\omega t)]^2 \tag{16}$$

During amplitude-modulated KPFM (AM-KPFM) measurements, V_{DC} is adjusted through a potential feedback loop to nullify the oscillating electrical forces originating from CPD between the tip and surface (i.e. setting $V_{DC} = V_{CPD}$) [42]. The overall AM-KPFM measurement process can be seen in Figure 26 where the area outlined as AM-KPFM represents the feedback and lock-in amplifier circuit and the other being the AFM process itself.

During surface scans, the cantilever tip operates in a tapping contact mode to map out the surface topography. Tapping mode is then turned off and the cantilever is moved to a set distance above the mapped surface as depicted by the dashed line

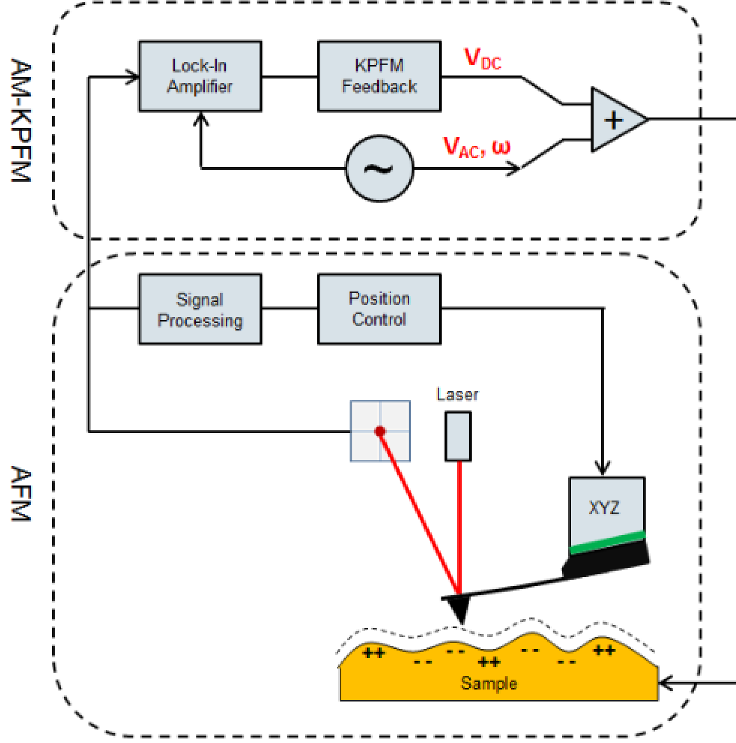

Figure 26. Diagram of AM-KPFM functionality [41].

in Figure 26, this ensures a set distance between the parallel-plates as described in the capacitor model previously. V_{AC} and V_{DC} are applied to the tip/sample surface as previously described and the feedback circuit adjusts V_{DC} to match V_{CPD} which causes F_{ES} to equal 0 and tip oscillation to cease. V_{CPD} is now measured through use of the lock- in amplifier across the surface of the sample. The differential work function between the tip and sample surface can be resolved by Equation 17 [42],

$$V_{CPD} = \frac{(\Phi_{tip} - \Phi_{sample})}{(-e)} \tag{17}$$

where Φ_{sample} and Φ_{tip} are the work functions of the sample surface and tip respectively and e is the electron charge. Since V_{CPD} has been measured, in order to find Φ_{sample} all that is needed is Φ_{tip}. The tip work function can be determined by taking a CPD measurement with a sample of known work function. In the case of

this study, a reference sample of highly ordered pyrolytic graphite (HOPG) with a known work function, $\Phi_{HOPG} = 4.6$ eV, was used and Φ_{tip} now could be calculated using Equation 18 and Φ_{sample} by substituting the value for Φ_{tip} in Equation 19.

$$\Phi_{tip} = \Phi_{HOPG} - (e * V_{CPD}) \tag{18}$$

$$\Phi_{sample} = \Phi_{tip} + (e * V_{CPD}) \tag{19}$$

Measurements of Φ_{HOPG} were taken in between each subsequent sample measurement as there was some anticipation of the AFM tip wearing during scan and re-scans of sample surfaces. A layer of HOPG was removed at the beginning of each set of measurements to ensure the tip work function was accurately calculated. The frequent measurements on HOPG were done in order to accommodate for and track any changes in work function of the AFM tip over time. It also provided a consistent reference point for subsequent measurements, i.e. if the tip work function changed drastically from measurement to measurement it could be an indication of severe tip degradation or need for equipment calibration to ensure integrity of data being collected.

For this research, all KPFM measurements were conducted in a Bruker Dimension Icon AFM equipped with DDESP-V2 electrical probes with conductive diamond tip coating. All equipment and samples were contained within an air-tight glove box enclosure filled with nitrogen and incorporated equipment to maintain O_2 and H_2O levels to provide an inert measurement environment.

3.5 Rapid Thermal Annealing Treatments

Studies, such as the one by [43], have proven that annealing after the deposition of co-sputtered alloys can greatly decrease grain size, reduce surface roughness, and

other physical properties of the alloys. It is easy to postulate that rapid thermal annealing (RTA) treatments could cause a change in the work function of sputtered thin-metals due to the change in physical properties.

A brief study on the effects of RTA treatments on the work function of co-sputtered probes with varied Au-Pt content was performed. Solaris 150 RTA hardware utilizing a lamp-based heating element was used to treat sputtered probes. It was capable of rapidly heating probes to temperatures as high as 1250°C for a duration of time. Probes were removed from the RTA system after allowing the absorbed heat to dissipate. Since the system allowed for users to select predefined recipes based on desired time and temperature, these were chosen as controllable treatment factors for the experiment. Platinum content was also treated as a factor as probes were sputtered with high and low percentages of platinum. After reviewing the phase diagram in Figure 49 and conferring with a subject matter expert, high and low settings for temperature and time were chosen. Settings for RTA time, temperature, and platinum content are outlined in Table 4 below.

Table 4. High and low RTA factor settings

Factors	Low (-1)	High (+1)
Pt Content (%)	13	77
RTA Temp (°C)	750	1000
RTA Time (s)	30	60

For the experiment, three factors were investigated at two levels each. The number of runs were limited by the availability of samples and so a half-factorial 2^{3-1} design was used. This design allowed for a total of four runs and was the most efficient way to provide information about the effects of the factors in the experiment while determining which factors significantly affected the mean response, work function [44].

3.6 Current Versus Voltage Measurements

In order to properly analyze current-voltage (I-V) measurements, it is imperative to first understand the device being characterized. When looking at the metal contacts deposited onto the UO_2 samples as described in the Section 3.2, the current transport mechanisms in MS junctions described previously becomes a useful reference when analyzing the resulting graphs.

For this research, I-V measurements were conducted in three different scenarios: "bulk" - through a deposited metal contact to ground via the UO_2 substrate, "bulk probe" - through a sputtered metal probe to ground via the UO_2 substrate, and "contact-to-contact" - through one deposited metal contact, the UO_2 substrate and to ground via the second deposited metal contact. Each of these scenarios are depicted below in Figures 27-28, where the test stand probes can be seen making mechanical contact with either the substrate surface or deposited metal contacts. Probes, or the metal chuck in the case of bulk measurements, are labeled as either "Probe Hi" or "Probe Lo" and are indicative of the applied bias on that probe.

An important consideration with respect to I-V measurements is the error introduced due to differences in effective contact area. All deposited metal contacts were assumed to be of ideal contact size and placement as illustrated in Figure 22 in Section 3.2. For purposes of this study, variations in effective contact area of probes were considered to be due to angle of incidence of the probe tip to the substrate surface, differences in tip radius of unsputtered and sputtered probes, and varied force used to apply probes to the substrate. With regard to angle of incidence and force applied to probes, due to the design of experimental setup, there was no straightforward method to ensure identical angles and force applied between probes and substrates across all of the measurements taken. Efforts to consistently place probes were striven for and it was assumed that any differences in these parameters

had negligible effects on the measurements taken. As for differences in effective contact radius between sputtered and unsputtered probes, a brief study was conducted. It was found that even when considering a tip with sputtered film thickness of 1000 nm, far thicker than any used in this study, that I-V plots only changed in magnitude by ∼3% and varied only ∼1% for films of 300 nm thickness.

3.6.1 Bulk I-V Measurements.

A profile view of a single metal contact deposited on a UO_2 substrate with component resistances is pictured in Figure 27 below. This profile is representative of how each of the bulk I-V measurements were taken experimentally, where a voltage (V_a) was applied to the metal contact and grounded through a metal chuck on the bottom of the UO_2 substrate.

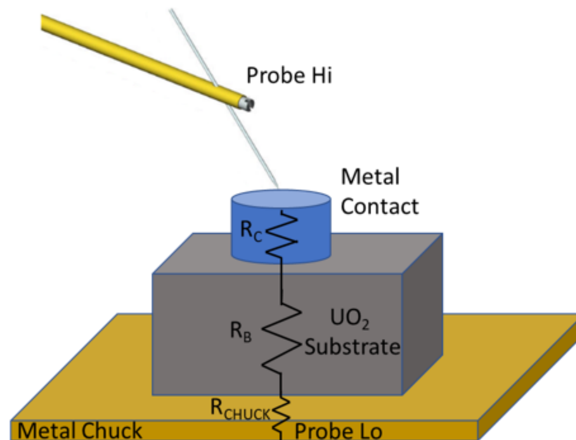

Figure 27. UO_2 **substrate with deposited metal contact showing equivalent component resistances.**

As can be seen, R_C represents the contact resistance for the metal contact, R_B the bulk resistance of the semiconductor, and R_C the resistance of the metal chuck. These component resistances, connected in series, can be represented by a single

equivalent resistance as follows:

$$R_S = R_B + R_C + R_{CHUCK} \tag{20}$$

3.6.2 Contact-to-Contact I-V Measurements.

A profile view of two metal contacts deposited on a UO_2 substrate with component resistances is pictured in Figure 28 below. This profile is representative of how each of the contact-to-contact I-V measurements were taken experimentally, where a voltage (V_a) was applied to metal contact 1 and grounded through the substrate to metal contact 2. The UO_2 substrate was electrically isolated from the I-V test stand by placing a glass slide beneath the substrate during measurements to avoid leakage current through the metal chuck.

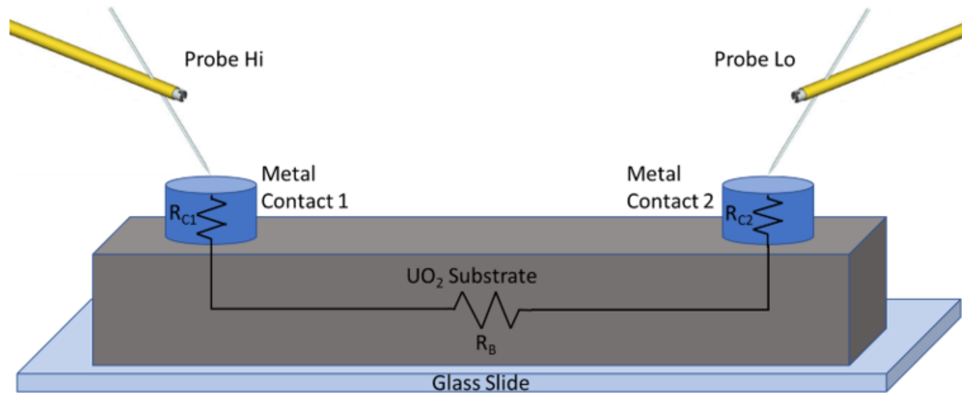

Figure 28. UO_2 **substrate with deposited metal contacts showing equivalent component resistances.**

As can be seen, R_{C1} and R_{C2} represent the contact resistances for metal contact 1 and 2 and R_B as previously defined. These component resistances in series can be represented by a single equivalent resistance as follows:

$$R_S = R_B + R_{C1} + R_{C2} \tag{21}$$

3.6.3 Bulk Probe I-V Measurements.

A profile view of a UO_2 substrate with component resistances is pictured in Figure 29 below. This profile is representative of how each of the bulk probe I-V measurements were taken experimentally, where sputtered probes were applied to the UO_2 substrate. A voltage (V_a) was applied to the substrate through the probes and grounded through the metal chuck of the test stand. The series resistance, R_S, can be calculated the same as in Equation 20 where R_C is now attributed to the contact metal sputtered on the probe tips.

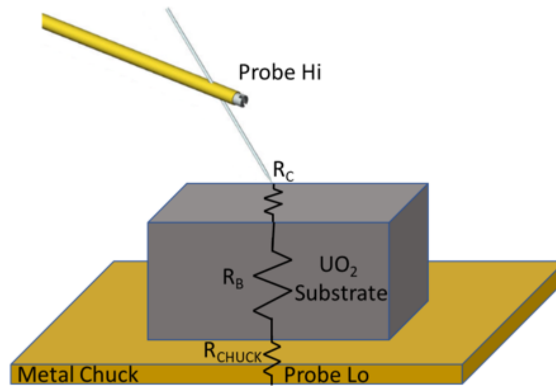

Figure 29. UO_2 **substrate with deposited metal contact showing equivalent component resistances.**

For this research, all I-V measurements were taken with a Keithley 2636B dual-channel system source meter unit (SMU) with built-in 4-quadrant voltage/current source and measure instrument. All I-V measurements were taken from +10 V to -10 V in .5 V increments. Bias on the probes was then swapped, and swept from -10 V to +10 V. Taking this measurement in this manner allowed for identification of any change in the plot due to bias or previous measurements and could serve as a good indication of hysteresis. Current was limited to 10 mA and a settling time of .5 seconds was utilized to allow measurements to normalize. Each measurement was taken back-to-back and was approximately 42 seconds in duration, multiple runs were taken for each measurement. The test stand and all samples were

placed inside an enclosure to avoid any unwanted effects due ambient light sources.

3.6.4 Ideal Metal-Schottky Diode I-V Curve Fitting.

Curve fitting tools become increasingly important when analyzing experimental I-V data and even allow for parameters such as I_S, R_S, and n to be resolved when properly fitted. In [45], the ideal MS diode current as outlined in Equations 8 - 10 are used to fit to experimental data. The process involves looking for a linear region in the FB I-V plot ($ln(I)$ vs. V) as depicted in Figure 30 below. The linear (2nd) region depicts the I-V behavior pertaining to the series resistance R_S with the dashed line fitted to the linear region bounded by $V_{MIN}$and V_{MAX}. The logarithmic form of the fit equation for this particular method is as follows:

$$ln(I) = ln(I_S) + \frac{q}{(nkT)} * V_A \qquad (22)$$

where n is an ideality factor that ideally is equal to 1 but is frequently determined to be slightly higher, and all other values are as defined previously [45]. For purposes of this study, MATLAB code was written to plot I-V data to allow for identification of the linear region, then inputting values for V_{MIN} and V_{MAX} the code was executed using a least-squares fit to determine the slope and y-intercept of the linear region and resolved fitting parameters I_S and n. The MATLAB script for this fitting code is listed in Appendix B.

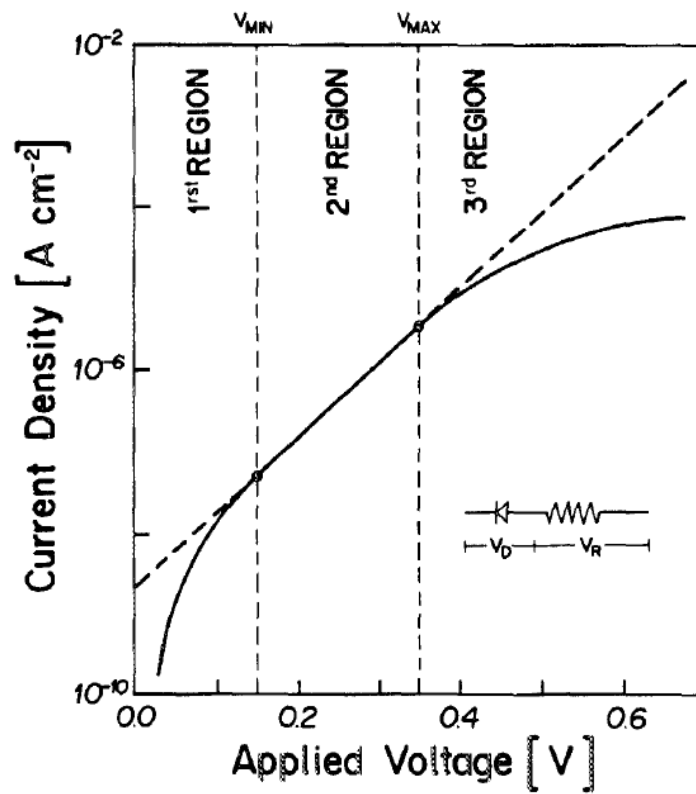

Figure 30. Experimental I-V data for non-ideal MS barrier depicting linear series resistance in the 2nd region with curve-fitted dashed line [46].

IV. Results and Analysis

4.1 EDS Measurements

In order to verify the composition of co-sputtered tungsten probes and Si wafers, EDS measurements were taken on each of the samples and are shown in Table 5 below.

Table 5. EDS-measured elemental composition for co-sputtered alloys

(At. %)	**EDS Measured**	
Predicted	Si Wafers	Probes
Au-13%Pt	3.14%Pt	3.08%Pt
Au-81%Pt	69.7%Pt	66.9%Pt
Au-35%Mg	40.01%Mg	51.41%Mg
Au-45%Mg	55.63%Mg	65.14%Mg
Au-50%Mg	57.04%Mg	52.40%Mg
Au-55%Mg	65.43%Mg	71.90%Mg
Au-65%Mg	71.44%Mg	77.27%Mg
Au-80%Mg	85.54%Mg	83.39%Mg
Au-90%Mg	87.71%Mg	90.08%Mg
Ag-65%Mg	56.86%Mg	69.11%Mg
Pt-65%Mg	62.89%Mg	78.79%Mg
W-65%Mg	57.83%Mg	71.46%Mg

Targeted composition values, based on relative power during the deposition process for composition compared to EDS-measured, were expected to be within $\pm$ 5% of each other as they were in [36] but were found to be within approximately $\pm$ 10% of one another barring a few compositions. Si wafer predicted values appeared to line up more closely than with measured values taken on the tungsten probe tips and there was some considerable variance between measured composition values for the wafers and probe tips. Differences between predicted and expected values were likely due to the accuracy of the profilometer measurements utilized in modeling/predicting expected compositions and the substrate on which they were taken. Because a physical step is required for the profilometer to determine

deposition thicknesses, areas on the silicon wafers were masked off and removed post-deposition. Due to the simplicity of masking and taking step measurements on the silicon wafers versus the probe tips, the availability/cost of the two substrates, and the assumption that deposition rates would essentially be equal for both substrates, it made logical sense to characterize the deposition rates for both substrates based on measurements taken solely from the silicon wafers. Because of this, it seems reasonable that composition values matched more closely on the silicon wafers. Other factors that could have played a part in composition variance are differences in metal adhesion between the two substrates and distance from/orientation to the deposition source.

4.2 Work Function Measurements

Measured work function values via AM-KPFM were taken on single-metal and co-sputtered thin films deposited on Si wafers, tungsten probes, and glass slides as described in sections 3.1 and 3.2. Pre-sputtered substrate work function values were taken for reference with the exception of the glass slides as glass is a known electrical insulator and therefore would not provide any meaningful data. Si wafers yielded an average work function value of 4.28 ± 0.23 eV, variance in work function was likely due to the test wafers used having different type, orientation, and doping levels. Tungsten probes had a measured work function value of 4.49 ± 0.05 eV. The effects of deposition thickness and annealing treatments on work function were also briefly investigated with platinum and gold-platinum coated probes.

4.2.1 Single-Metal Measured Values.

Single-metal work function values for each of the substrates were compiled and are listed in Table 6 appended with expected work function values from Table 3.

Table 6. Table of KPFM measured work function values for single metals

Metal	Φ_{Target}(eV)	Φ_{Si}(eV)	Φ_{Glass}(eV)	Φ_{Probe}(eV)	Φ_{Exp}(eV)
Ag	4.75	4.66	-	4.66	4.0-4.3
Al	3.56	3.85	3.11	3.55	4.06-4.26
Au	4.66	4.83	4.72	4.59	4.75-5.45
Co	4.44	4.89	4.25	4.51	4.4-5.1
Cu	4.54	4.67	3.42	4.62	4.4-4.7
Mg	3.05	4.28	-	3.96	3.66
Mo	4.98	4.11	3.19	4.51	4.0-4.75
Ni	4.32	4.49	4.52	4.49	4.5-5.25
Pt	4.49	4.67	5.06	4.75	4.9-5.65
W1	3.98	4.54	5.35	4.17	5.2-5.8

Reviewing the table of measured work function values there are a few metals whose measured values do not fall within the expected range of work function values. There are several explanations for these deviations in work function, many of which being metal-specific, include but are not limited to: measured crystal face, adsorption of oxygen, electronic structure, and chemical effects due to exposure to atmospheric conditions over time [47]. Looking specifically at Ag, a study done by [48, 49] looked at the difference in work function of (110), (100), and (111) single crystals before and after cleaning the surfaces by argon ion bombardment and annealing in vacuum. It was found that measurements taken pre- and post-cleaning changed significantly with values for (110) and (100) crystals initially measured at 4.5 eV - 4.6 eV came down to 4.14 eV and 4.22 eV respectively, where the (111) crystal shifted from 4.8 eV down to 4.46 eV. It was discovered that the presence of carbon on the silver crystals had the effect of reducing the work function while the presence of sulfur on the surface had the opposite effect. The effects of adsorption and oxidation on poly-crystalline Al were studied in [50], where it was found that the work function of the surface cleaned by ion bombardment decreased by as much as 1.2 eV after exposure to atmosphere for as little as 60 minutes.

4.2.2 Co-Sputtered Metal Measured Values.

Co-sputtered metal work function values for each of the substrates were compiled and are listed in Table 7 below.

Table 7. KPFM measured work function values for co-sputtered metals

Alloy	Φ_{Si}(eV)	Φ_{Glass}(eV)	Φ_{Probe}(eV)
Au-13%Pt	4.87	-	4.56
Au-81%Pt	4.87	-	4.66
Au-35%Mg	3.93	-	3.55
Au-45%Mg	3.53	3.92	3.28
Au-50%Mg	2.87	-	2.92
Au-55%Mg	3.68	4.75	3.12
Au-65%Mg	3.45	-	2.84
Au-80%Mg	3.21	3.84	3.12
Au-90%Mg	3.34	4.99	3.05
Ag-65%Mg	3.43	3.81	3.76
Pt-65%Mg	4.39	3.74	3.60
W-65%Mg	3.38	4.47	3.43

Based on a similar study utilizing Au-Ag compositions [51], work function values were not expected to follow a linear relationship with respect to composition and to fall somewhere between the range of their respective single-metal values as listed in Table 6. It seems though, at least with varied Au-Mg compositions, the relationship between composition and work function appears to be mostly linear in nature. Figure 31 below depicts EDS-measured Au-Mg compositions versus the corresponding KPFM-measured work function values of as-deposited alloys on silicon wafers.

Six work function measurements were taken across each of the silicon wafers for each Mg composition level, error bars represent the standard deviation from the average work function value at each point. The work function of the different alloys decreases rapidly from 4.83 eV at 0% Mg (100% Au) down to 3.21 eV for the ∼86% Mg data point. It is assumed that the work function increases rapidly again after

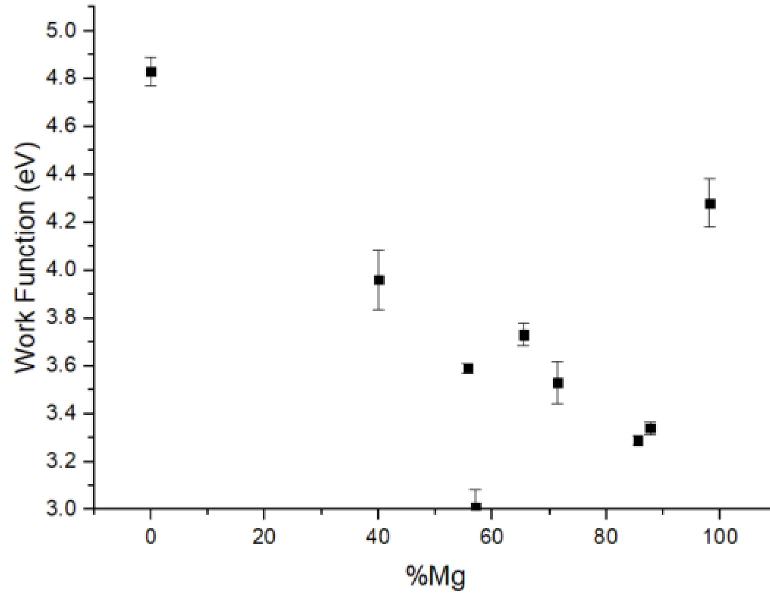

Figure 31. Au-Mg composition versus work function on Si wafers.

90% Mg content from thick oxide layers formed due to magnesium's highly reactive nature when exposed to atmosphere over time. Depositions of Ag, Pt, and W with 65% targeted Mg content achieved interim work function values of 3.76 eV, 3.60 eV and 3.43 eV on tungsten probes. Figure 32 below depicts the same information as the graph in Figure 31 but for Au-Mg alloys deposited on tungsten probes.

At 0% Mg, the measured work function value is 4.59 eV. The work function decreases to a value of 3.05 eV at ∼90% Mg content. It appears that both graphs follow a very similar trend of decreasing work function up to ∼90% Mg content with an increase in work function thereafter. There appears to be some indication that the work function of these thin-metal films may be mostly independent of the substrate although the trends outlined in this section provide confirmation that increasing the concentration of Mg in Au-Mg alloys effectively decreases the work function.

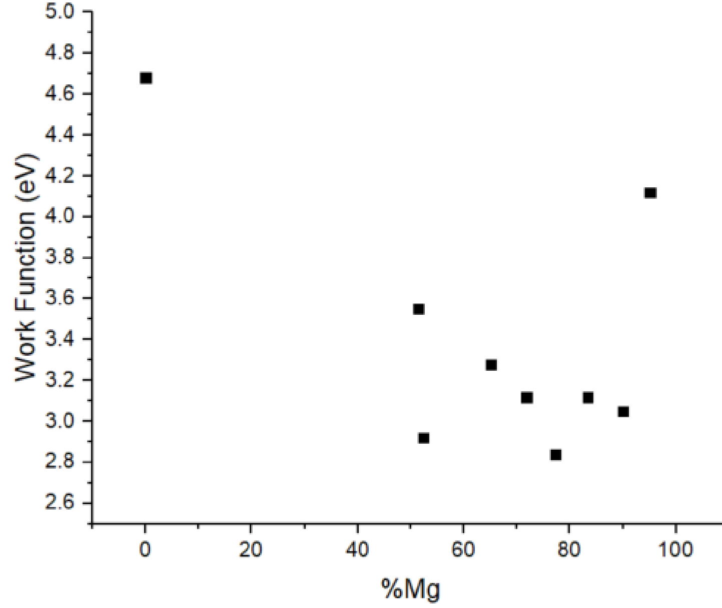

Figure 32. Au-Mg composition versus work function on tungsten probes.

4.2.3 Work Function Dependence on Film Thickness.

Platinum depositions were executed on tungsten probes with varying thicknesses up to 500 nm. Platinum deposited thicknesses and their respective measured work function (Φ_{Pt}) values were compiled and are listed in Table 8 below.

Table 8. KPFM measured work function values for varied thickness Pt films

Pt Thickness (nm)	Φ_{Pt}(eV)
0	4.49
37	4.57
54	4.8
87	4.82
298.7	4.75
500.4	4.78

Figure 33 below depicts the relationship between platinum sputtered on tungsten probes and work function values at different deposition thicknesses.

The point at 0 nm represents an unsputtered tungsten probe with a KPFM-measured work function value of 4.49 eV. Work function values increase with platinum thickness up to around 55 nm and appear to become constant after

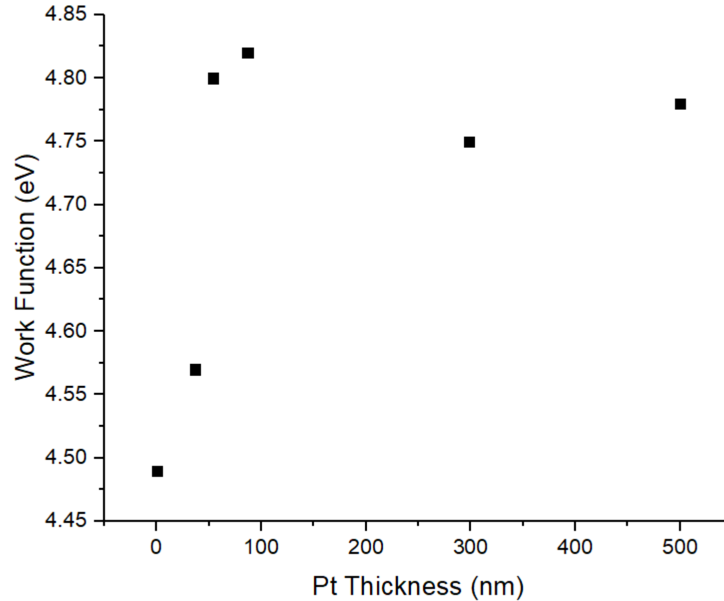

Figure 33. Pt film thickness versus work function on tungsten probes.

that, deposited thicknesses of 55 – 500 nm yield an average work function value of 4.79 ± .03 eV. This data agrees with the assertion that the thickness of the deposited metal can affect measured work function of the thin film. It would appear that the substrate is "seen" in thinner metal films but becomes negligible after a certain thickness, in this case, depositions greater than or equal to 55 nm. It is possible that other substrates, metals, deposition methods, and/or work function measurement techniques could affect film thicknesses required to mask the substrate. Further studies in this area would be highly beneficial.

4.2.4 Work Function Dependence on RTA Treatments.

RTA treatments were performed on Au-Pt co-sputtered probes utilizing the factor levels and methodology as outlined in Section 3.5, results are outlined in Table 9 below. Run order indicates the order in which each treatment was applied to the probes and probe # was assigned to identify which probe was being treated. Work function values as measured by KPFM are listed in the right-most column (Φ_{Probe}).

Table 9. RTA treatments and measured work function values of treated probes

Run Order	Std Order	Pt%	Temp (°C)	Time (s)	Probe #	Φ_{Probe}(eV)
1	2	77	750	30	5	4.66
2	3	13	750	60	1	4.85
3	4	13	1000	30	2	4.82
4	1	77	1000	60	6	4.8

An analysis of variance (ANOVA) was performed using Minitab statistical software where it was found that none of the factors were considered to have a significant effect on work function. The half-normal plot shown below in Figure 34 visually demonstrates the effect size breakdown where the cross on the top right is the largest effect size of platinum content, bottom left is the next largest effect size of temperature, and the cross on the line is the smallest effect size, time. It appears the factors examined did affect work function values to some degree, however, due to the limited sample size the ANOVA method did not have a sufficient number of data points to determine statistical significance.

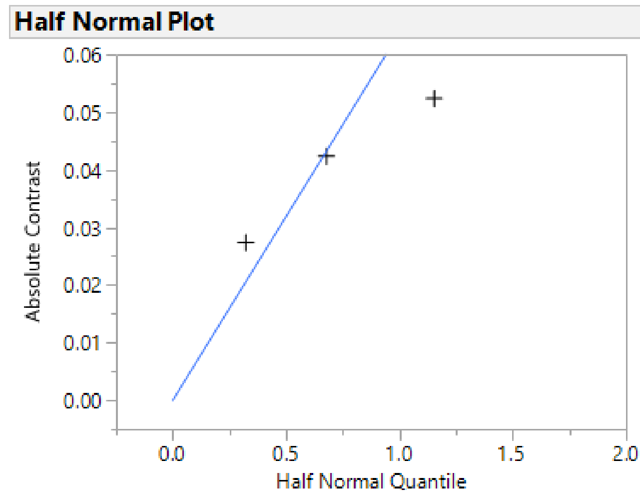

Figure 34. Half-normal plot of effects for temperature, time, and Pt content.

Due to the small sample size, an analysis utilizing "Cohen's d" was performed to determine the overall impact of the different factors on work function. Since each factor has only two levels, conducting only pairwise comparisons using the formula

and process shown below in equations 23-26 was sufficient [52]. Note that any value greater than 0.8 is deemed to have a significant impact, even if p-values in the ANOVA table are not significant as determined in prior analysis.

$$Cohen'sD : \frac{(Mean_1 - Mean_2)}{(SD_{Pooled})} = EffectSize \tag{23}$$

$$Pt_{13\%} - Pt_{17\%} = \frac{(4.84 - 4.73)}{\sqrt{\frac{.212^2 + .099^2}{2}}} = 1.54 \tag{24}$$

$$Time_{30s} - Time_{60s} = \frac{(4.81 - 4.76)}{\sqrt{\frac{.141^2 + .134^2}{2}}} = .528 \tag{25}$$

$$Temp_{750^\circ C} - Temp_{1000^\circ C} = \frac{(4.82 - 4.74)}{\sqrt{\frac{.113^2 + .0354^2}{2}}} = .955 \tag{26}$$

From the analysis above on effect size it is noted that there was a strong effect size in the differences in groups of platinum content and temperature, but time only has a medium overall effect size. These metrics serve further to support the conclusion that further experimentation is needed to determine statistical significance via the ANOVA method. Further analysis concluded that sample sizes required to determine significance for each factor are as follows: platinum content – 5, RTA time – 20, and RTA temperature – 8. Given the promising results from the effect size analysis and the minimal number of required samples to determine significance for platinum content and RTA temperature, performing the second half of the half-factorial 2^{3-1} design used in this study is recommended for future studies.

4.3 I-V Measurements

I-V measurements outlined in this section were taken on UO_2 samples as described in Section 3.6 above. Due to the large amount of data collected, the

entirety of all plotted I-V data is located within Appendix section 1.4 for reference. The titles of each of the individual plots indicate which metal contact(s) were being contacted by test probes during measurement. In the case of contact-to-contact measurements, the title of the plot can be interpreted as "metal contact 1 - metal contact 2" as depicted in Figure 28. Plots containing UO_2 in the title are indicative of a measurement utilizing probes directly to the substrate and serve as a baseline for comparison. Any pertinent data contained within specific individual plots was pulled forward for analysis and any identified trends were outlined in the following sections.

As for the evaluation/interpretation of the I-V plots looked at in the following section, a brief explanation is needed. Due to the low current throughput and symmetric nature of the data observed, it was assumed that despite the Ohmic appearance of the plotted I-V data that the MS junctions looked at in this study couldn't be classified as such. So instead, it was decided that I-V plots would be analyzed comparatively in which resistivity and the amount of carriers allowed through the junction would serve as comparative factors. Plots having a steeper slope and greater magnitude were considered less resistive allowing for more carriers through the junction and were considered "better" in comparison.

4.3.1 Bulk I-V Plots.

The complied collection of bulk I-V plots can be seen in Figures 55 and 56 for the (100) and (111) sample respectively. Through visual inspection it is easy to identify which deposited contacts form a functional contact and of those, which are optimal with regard to maximum allowed current and the nature of the junction formed. The test configuration for these measurements are depicted in Figure 27 where both probes utilized consisted of uncoated tungsten.

On the (100) sample, only two of the deposited metals appeared to form functional contacts. A graph depicting bulk I-V measurements through these contacts and a reference plot through just the UO_2 substrate can be seen in Figure 35 below.

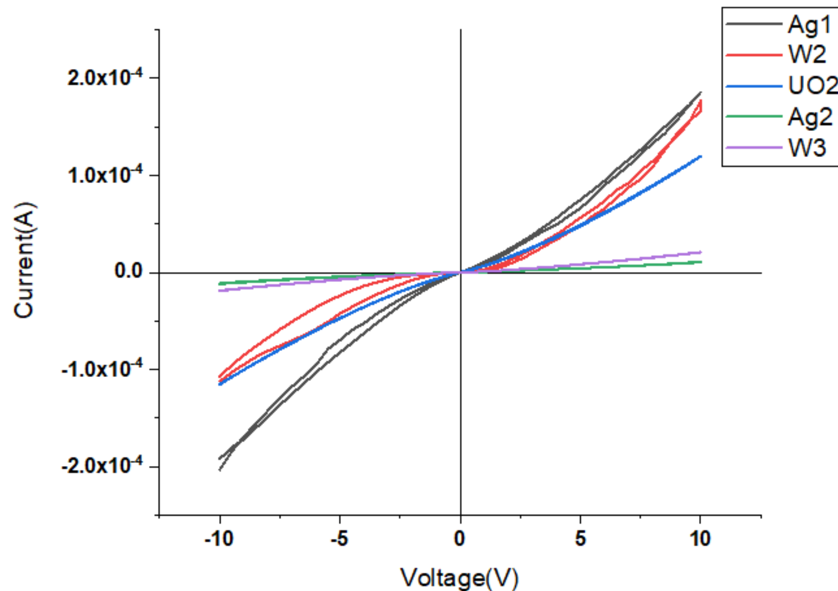

Figure 35. Summary bulk I-V plot of deposited metal contacts on (100) sample.

Individual I-V plots of Ag1 (black), W2 (red), Ag2 (green), W3 (purple) and UO_2 (blue) can be seen plotted together on the same axes. The UO_2 plot provides a useful reference for comparison of the deposited metal contacts as it depicts the bulk I-V behavior without a deposited metal contact present. It appears that I-V behavior for the W2 contact mimics that of the baseline UO_2 fairly closely in the reverse bias region, departing at higher voltages in the forward bias and shows some signs of hysteresis. Ag2 and W3 did not appear to provide good contact which is represented by the highly resistive nature of their plots. Ag1 appears to be more linear in nature and had a maximum current throughput of $\pm .2$ mA at ± 10 V. On the (111) sample, considerably more of the metals appeared to make a functional contact with the substrate. A graph similar to that of Figure 35 was compiled for

Ag1, Pt2, Ag2, Ag3, Au1, Au2, W3, and the UO_2 reference for contacts to the (111) substrate and can be seen in Figure 36 below.

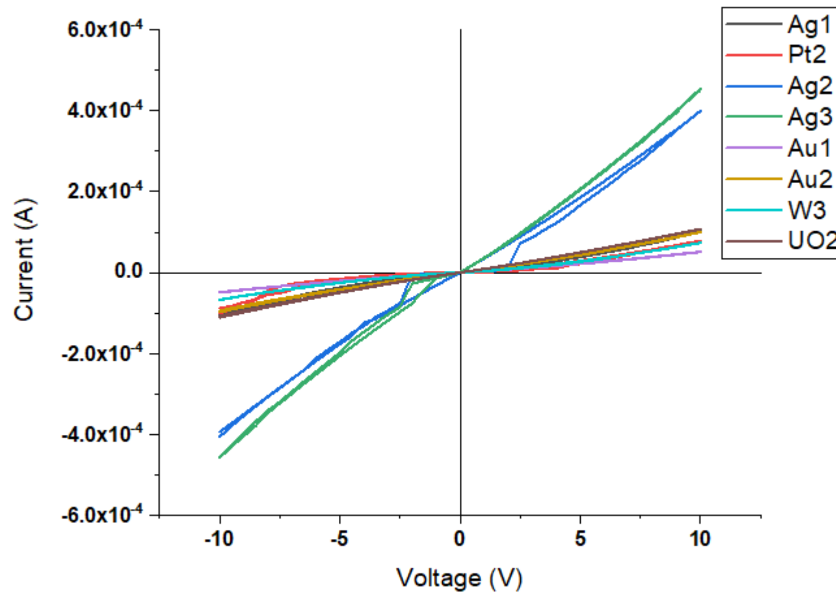

Figure 36. Summary bulk I-V plot of deposited metal contacts on (111) sample.

It can be seen that contacts composed of Pt, Au, and W, despite displaying mostly linear behavior, appeared to form more resistive junctions than those made with Ag and departed only minimally from the reference plot. Ag2 (blue) and Ag3 (green) clearly show the best performance of the deposited contacts with a max current throughput of ±.395 mA and ±.455 mA respectively at ±10 V. Both Ag contacts appear to be mostly linear in nature but do show some signs of hysteresis. While aluminum was deposited on both of the samples, it did not appear to form a good junction with the substrate as indicated by characteristic open circuit plots for all deposited Al contacts.

An interesting phenomenon occurred during I-V measurements where plots appeared to shift from the first to last repeated measurement. These trends are shown in Figure 37 below. Max current (I_{MAX}) for each of the I-V measurements is plotted against the run # for each contact, where run # is plotted in increasing

chronological order of the measurement taken. All runs can be considered replicates as they were taken back-to-back after probes were positioned on the contact and were not lifted off until all replicate measurements were complete.

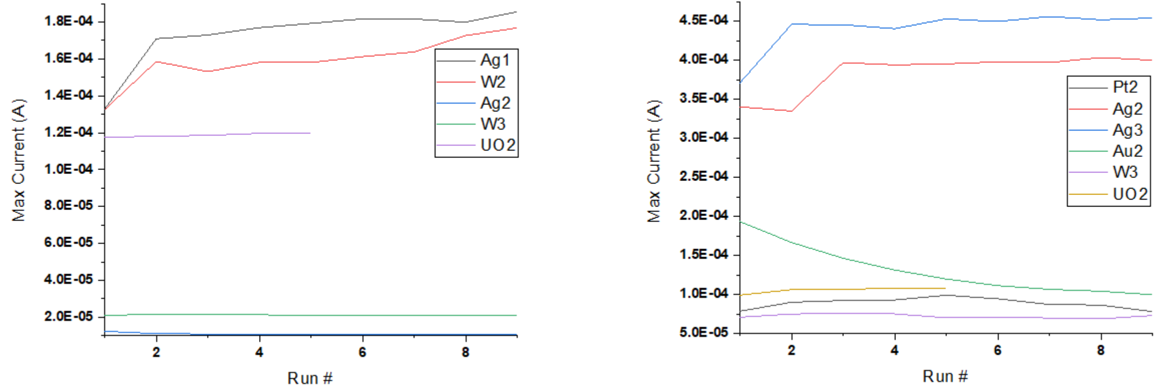

(a) Max current versus run #: (100) sample.

(b) Max current versus run #: (111) sample.

Figure 37. Max current versus run number: bulk I-V.

Referring to Figure 37(a), contacts Ag1 and W2 can be seen plotted with the UO_2 reference line for the (100) sample. It appears that I_{MAX} is gradually increasing with each run but does not seem to reach a steady-state current within the 9 runs that were conducted, UO_2 does not show much variation and seems to level out by run 4. Referring to Figure 37(b), contacts Ag2 and Ag3 follow a very similar trend of an increasing I_{MAX} to a steady-state max current, Ag3 is seen leveling off at around run 2 where Ag2 takes another run to do so. Looking at Au2, the trend in I_{MAX} can be fit almost perfectly to a logarithmic decay function where the steady-state current is reached toward run 8 or 9. There are many plausible reasons that could be attributed to these trends in I_{MAX}, however it seems probable that either the junction is changing over time or there is a build-up of charge at the junction due to the low mobility of the substrate. The effects of this seem to be minimal in the (111) sample but seem to play a more significant role in the (100) sample.

4.3.2 Contact-to-Contact I-V Plots.

The complied collection of contact-to-contact I-V plots can be seen in Figures 59 and 60 within Appendix 1.4 for the (100) and (111) sample respectively. As before with the bulk I-V measurements, it is easy to identify which deposited contacts form a functional contact and of those, which are optimal with regard to maximum allowed current and the nature of the junction formed. The test configuration for these measurements are depicted in Figure 28 where both probes utilized consisted of uncoated tungsten.

On the (100) sample, six of the deposited metal contacts appeared to function better than the UO_2-UO_2 reference. A graph depicting bulk I-V measurements through these contacts and a reference plot through just the UO_2 substrate can be seen in Figure 38 below.

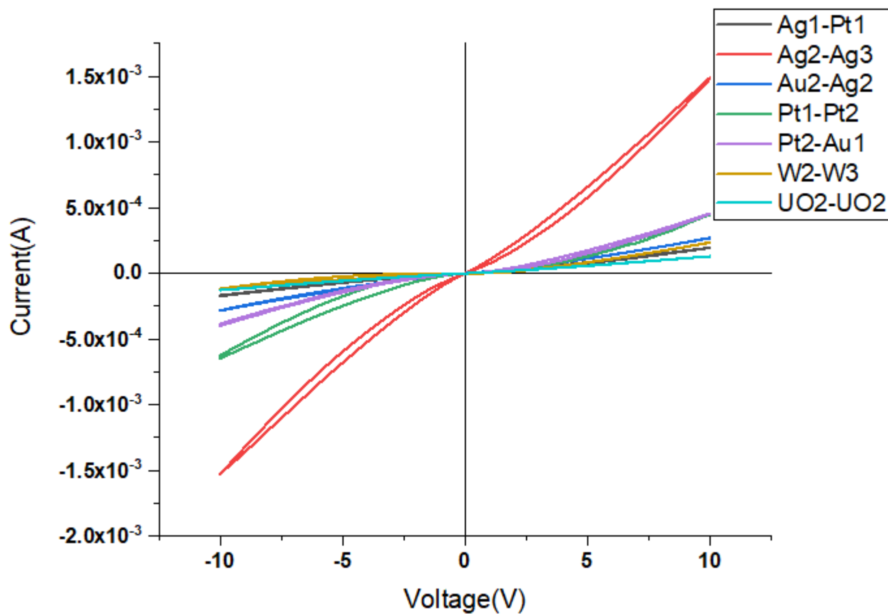

Figure 38. Summary contact-to-contact I-V plot of deposited metal contacts on (100) sample.

I-V plots of Ag1-Pt1 (black), Ag2-Ag3 (red), Au2-Ag2 (blue), Pt1-Pt2 (green), Pt2-Au1 (purple), W2-W3 (orange), and UO_2-UO_2 (teal) can be seen plotted

together on the same axes. As before, the UO_2-UO_2 plot provides a useful reference for comparison of the deposited metal contacts as it depicts the I-V behavior with just the mechanical contacts of the probes present. Aside from the Ag1-Ag2 and Pt1-Pt2 contacts, it appears that the other combinations of contacts performed better than the baseline measurement although marginally. Pt1-Pt2 appeared to form a moderately resisitive and displayed mostly linear behavior with a max current in the FB of .455 mA and .647 mA in the RB, there were some signs of mild hysteresis. Ag2-Ag3 appeared to be the best performing contact pair on the (100) substrate with ±1.5 mA at ±10 V respectively. The junction appeared to depart slightly from linearity with some mild hysteresis. A graph similar to that of Figure 38 was compiled for Ag1-Pt1, Ag1-W2, Ag2-Ag3, Au2-Ag2, Pt1-Pt2, W2-W3, and the UO_2-UO_2 reference provided for contacts to the (111) substrate and can be seen in Figure 39 below.

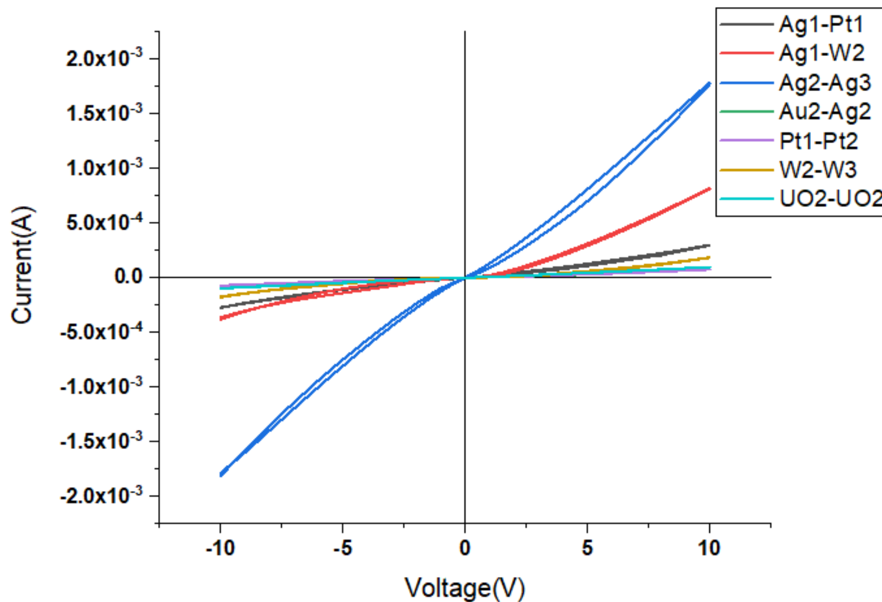

Figure 39. Summary contact-to-contact I-V plot of deposited metal contacts on (111) sample.

Of the deposited contacts on the (111) substrate, Ag2-Ag3 and Ag1-W2 appear to form the most ideal junctions. Ag2-Ag3 again seems to be the most linear with

maximum current throughput of ±1.79 mA, slight hysteresis in the RB and moderate in the FB. Ag1-W2 displays some interesting behavior akin to some combination of the Ag and W contact metal I-V plots, appearing to almost function more like a traditional diode with minimal current (.362 mA @ -10 V) in the RB and increasingly more when in FB (.816 mA @ +10 V). It was evident that for both the (100) and (111) samples that Ag was the optimal contact metal used, this was of no surprise as this was the case with the bulk I-V results.

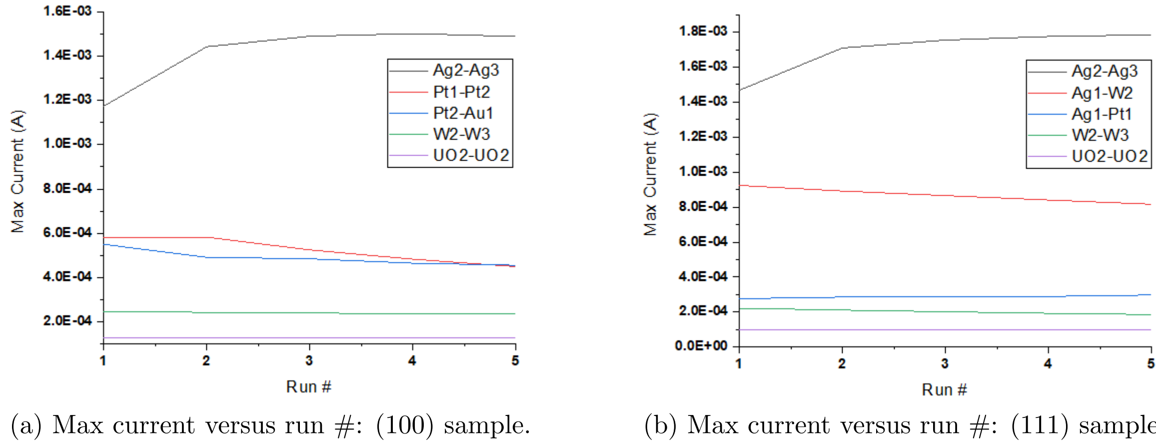

(a) Max current versus run #: (100) sample.

(b) Max current versus run #: (111) sample.

Figure 40. Max current versus run number: contact-to-contact.

Looking again at the relationship between max current and run # as was done previously in the bulk I-V analysis, some of the trends in Figure 40 seem to be similar to those previously analyzed. Referring to the Ag2-Ag3 junctions in Sub-Figures (a) and (b), the trends are quite similar to one another and build up to a steady-state I_{MAX} as they did previously and level off. Pt1-Pt2 and Pt2-Au1 on the (100) substrate display some interesting behavior where they both share a similar starting and final I_{MAX}. The Pt-Pt contact has a constant $I_{MAX}$for the first two runs and gradually decreases to run 5 where the Pt-Au contact decreases initially and starts to level off after the 2nd run, eventually ending at nearly the same max current as one another. It is believed that the same factors influencing the behaviors outlined in the bulk I-V section are the same here. One difference

here being that both sets of Ag contacts appear to behave almost identically on both samples and are within .2 mA each other's measured I_{MAX}.

4.3.3 Bulk Probe I-V Plots.

The complied collection of bulk probe I-V plots can be seen in Figures 57 and 58 within Appendix 1.4 for the (100) and (111) sample respectively. The experimental setup used in bulk probe evaluations are fundamentally different than those of the bulk and contact-to-contact I-V plots as both methods involved taking measurements through metal contacts deposited to the surface of the UO_2 substrate whereas the bulk probe method utilized sputtered metal probes applied directly to the substrate surface. The reference I-V measurement was taken using an unsputtered tungsten probe and can be seen labeled as "W" in all of the plot legends, not to be confused with "W1" which represents a probe sputtered with tungsten metal. Going forward, W will serve as a baseline to compare the other measurements against. All probes used in these measurements are the same as those outlined in Section 3.2 and analyzed in Section 3.4.

4.3.3.1 Single-Metal Probes.

Graphs depicting bulk I-V measurements through single-metal probes and a reference plot using the W probe can be seen in Figure 41 below. On both the (100) and (111) sample, most of the sputtered single-metal probes appeared to function as well or better than the W reference probe.

On the (100) sample in Figure 41(a), it appears that Al, Au, and Ag form the best junctions with the UO_2 substrate. All of the measurements taken are of the same magnitude of those taken in the bulk measurements in Figure 35 with the max current through the Al probe measuring at $\pm .295$ mA, behavior appears mostly

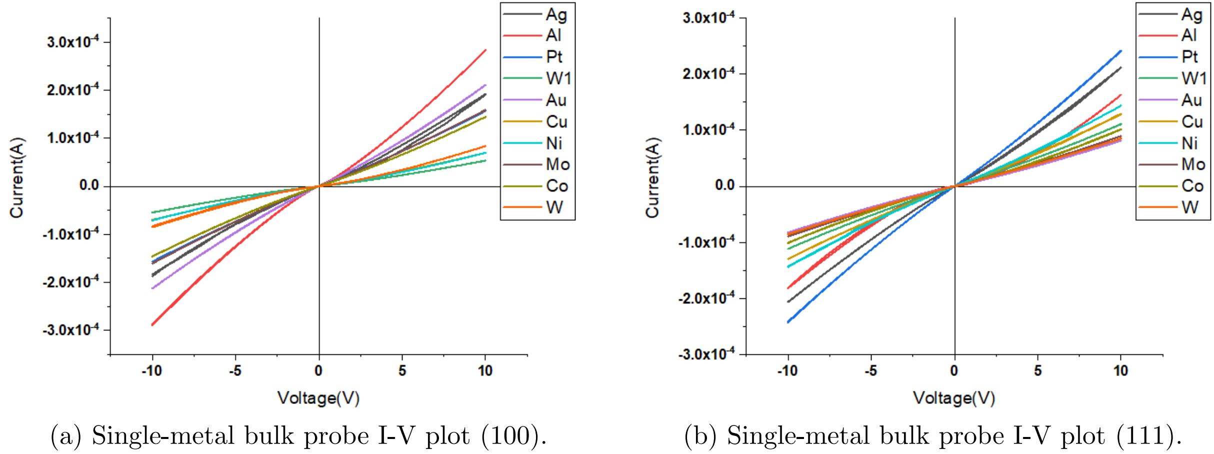

(a) Single-metal bulk probe I-V plot (100). (b) Single-metal bulk probe I-V plot (111).

Figure 41. Summary single-metal bulk probe I-V plots.

linear. Au and Ag perform similar to one another also displaying mostly linear behavior, although more resistive than Al with Ag showing a little hysteresis in the FB. All other measurements taken on the (100) appear to form better junctions than the W reference plot, with the exception of Ni and W1. Looking at the measurements taken on the (111) sample in Figure 41(b), it appears that Pt, Ag, and Al form the best junctions with the substrate. The max current through the Pt junction measures at ±.242 mA and behaves in an almost perfectly linear fashion. Ag behaves very similarly and measures at ±.210 mA max current throughput where Al appears to depart from linearity. All other single-metal probes on the (111) sample form superior junctions to the W reference with the exception of Au.

In Figure 37 above, a look at I_{MAX} from initial to final run can be seen for the single-metal probe measurements. In the (100) sample it appears that all I_{MAX} values appear to remain more or less constant across runs with the exception of Al and Ag where Al appears to gradually taper off to a steady-state current and Ag behaves as it did with the previous measurement methods. In the (111) sample, all I_{MAX} values appear to remain constant with the exception of Al which gradually decreases over the range of runs. As a whole, I_{MAX} values appear to remain more

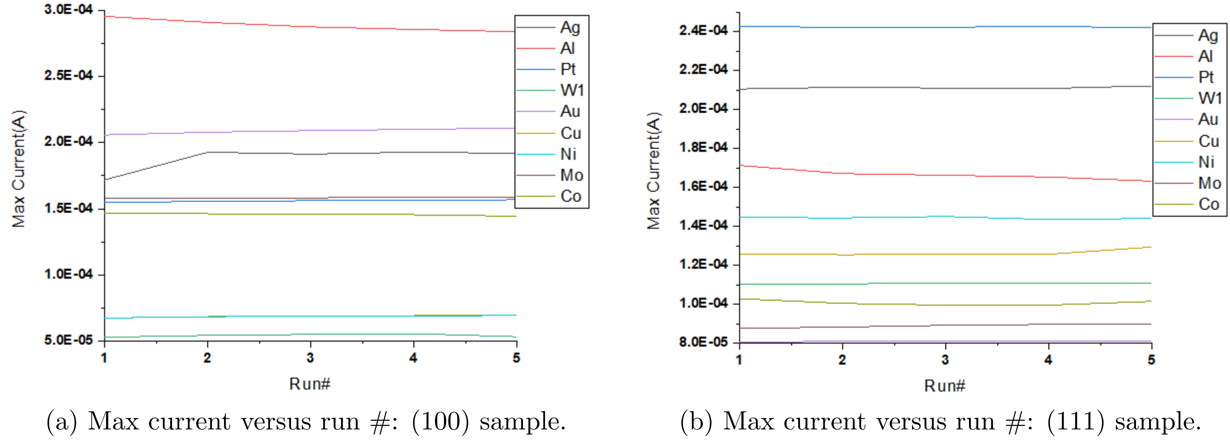

(a) Max current versus run #: (100) sample. (b) Max current versus run #: (111) sample.

Figure 42. Max current versus run number: single-metal bulk probe.

constant in these measurements than they did when compared to the measured values of the other methods. This difference could be attributed to changes in the substrate caused by the metallization process and could explain some of the behavior seen in Figures 37 and 40 previously.

4.3.3.2 Binary-Metal Probes.

The binary-metal probes used in this section can be identified in Section 4.2 as those with the following predicted Mg concentrations: AuMg1 - 45%Mg, AuMg2 - 55%Mg, AgMg - 65%Mg, PtMg - 65%Mg, and WMg - 65%Mg. All binary-metal bulk probe I-V measurements were compiled and can be seen plotted together in Figure 43 below. On the (100) and (111) sample, all binary-sputtered probes appear to form junctions that perform better than that of the W reference probe.

On the (100) sample in Figure 43(a), it appears that WMg, PtMg, and AgMg probes form the best junctions with the UO_2 substrate. WMg and PtMg seem to display mostly linear behavior with the same I_{MAX} of $\pm.229$ mA. AgMg appear to depart slightly from linearity and forms a more resistive barrier showing some signs of mild hysteresis. Referring to Figure 43(b), measurements on the (111) sample can be seen with WMg and AuMg1 forming the optimal contacts on that substrate.

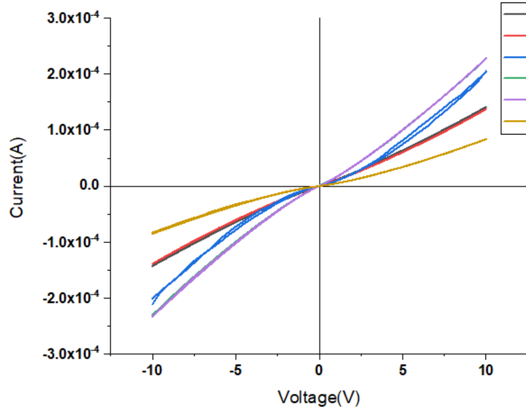

(a) Binary-metal bulk probe I-V plot (100).

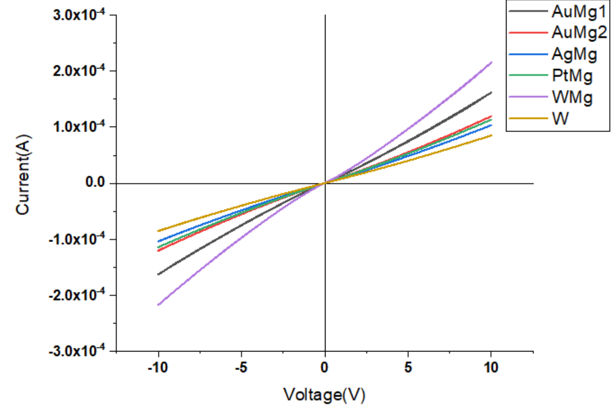

(b) Binary-metal bulk probe I-V plot (111).

Figure 43. Summary binary-metal bulk probe I-V plots.

WMg appears mostly linear with a max current of ±.217 mA, where AuMg1 behaves similarly but forming a slightly more resistive junction.

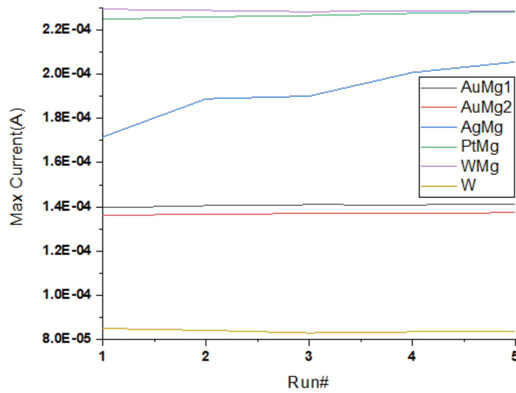

(a) Max current versus run #: (100) sample.

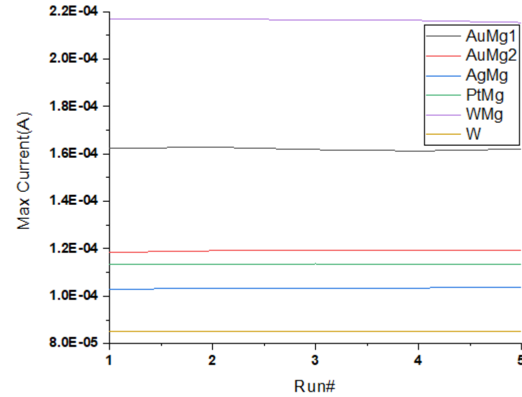

(b) Max current versus run #: (111) sample.

Figure 44. Max current versus run number: binary-metal bulk probe.

The max current versus run number of both (100) and (111) samples for measurements of I_{MAX} taken using binary-metal probes is depicted in Figure 44 above. On the (100) sample it appears that all measured I_{MAX} values across runs remain relatively constant with the exception of the AgMg probe. AgMg's max current gradually rises from run-to-run in a pseudo-step like fashion and begins to flatten off toward run 5. This seems similar to the behavior depicted for the Ag probe in Figure 42 on the (100) sample, though it would appear that the addition of

Mg has altered it somewhat. Looking at Figure 44(b), I_{MAX} measurements taken on the (111) sample versus run number can be seen. All measured I_{MAX} values remain relatively constant across all runs and for all probes. An interesting trend can be seen within both samples with respect to I_{MAX} and measured work function values of the binary metal probes with some assumptions. Looking at the binary-metal probe measured work function (Φ_{Probe}) values with $\Phi_{AuMg1} = 3.28$ eV, $\Phi_{AuMg2} = 3.12$ eV, $\Phi_{AgMg} = 3.76$ eV, $\Phi_{PtMg} = 3.60$ eV, and $\Phi_{AgMg} = 3.43$ eV and assuming that the AuMg probes form p-type junctions while the others form n-type, there could be a case made for barrier lowering with an increase/decrease in (Φ_{Probe}) respectively. Measurements of I_{MAX} using the AuMg probes on both samples show an increase in max current with increasing (Φ_{Probe}), whereas the other Mg-alloy probes show an increase in I_{MAX} with decreasing (Φ_{Probe}).

4.3.4 Single-Metal Bulk Versus Bulk Probe I-V Plots.

The goal of this section is to make comparisons between the the single-metal bulk measurements that were discussed in Section 4.3.1 and the single-metal bulk probe measurements that were discussed in Section 4.3.3. The I-V plots from both measurement methods can be seen plotted together in Figure 45 below where the solid lines represent bulk I-V plots and dashed lines bulk probe I-V plots. The similarities in contact size of the probes used and the experimental setup during measurements allows for some interesting comparisons. Of the deposited contacts, the only ones that appeared to perform equal or better than probes of like metal were that of Ag and W on the (100) sample and Ag, Au, and W on the (111) sample. This, along with the fact that many of the deposited metal contacts yielded open-circuit I-V plots points to a possible issue with metal adhesion to the UO_2 surface. This fact was also evidenced visually during experimentation as it was

observed that contact metals would gradually degrade over time. It would appear that silver and tungsten form the most viable contacts on the UO_2 samples looked at in this study. One area of interest pertaining to this matter would be a study into adhesion layer metals or the effects of annealing contacts post-deposition. Based on information gained through this study, it would seem reasonable to combat adhesion issues by using Ag as a thin deposition layer prior to depositing other contact metals or through co-deposition of contact metals containing Ag such as: Ag-Au, Ag-Pt, or Ag-Al.

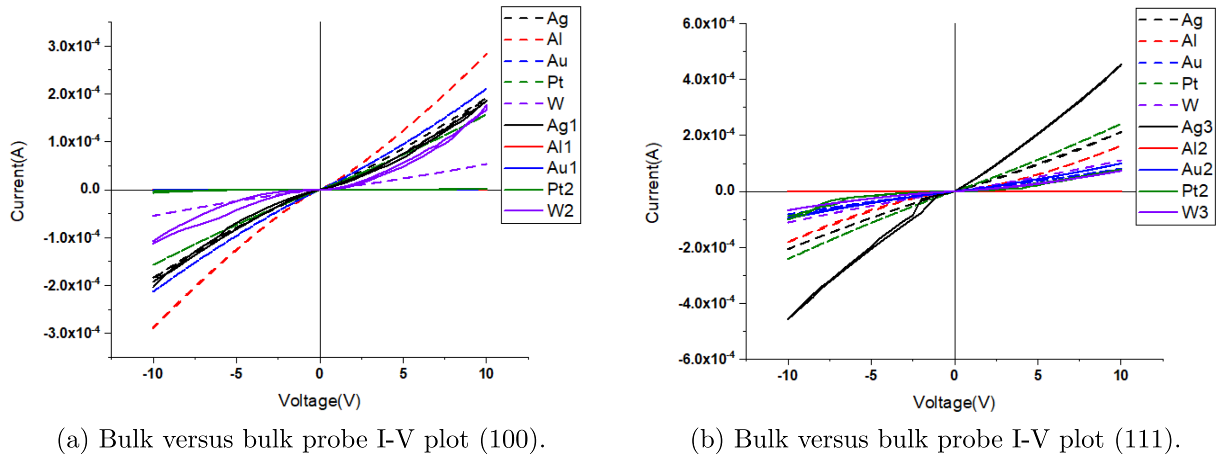

(a) Bulk versus bulk probe I-V plot (100). (b) Bulk versus bulk probe I-V plot (111).

Figure 45. Summary single-metal bulk versus bulk probe I-V plots.

4.3.5 Effects of Contact Area.

When comparing I-V plots against one another, current data is generally adjusted for contact area and plotted as current density (J) to allow for a normalized comparison of plots. Adjusting for contact area is a simple calculation but can yield orders of magnitude of difference between plots depending on the effective contact areas during measurement. The equation for transforming current to current density is as follows:

$$J = (I/A) \tag{27}$$

where I is the measured current and A the area of the contact. Throughout this study, I-V plots were not adjusted for contact area as comparisons were made only within measurement methods where it was assumed that differences in contact areas between measurements were negligible.

The analysis performed in Section 4.3.4, however, was conducted without normalizing current values despite the expectation of significant differences in nominal contact areas between the bulk and bulk-probe measurement methods. Assuming an ideal contact radius of 10 μm for probe tips and 100 μm for deposited contacts and using Equation 27 to adjust for circular contact area, it is easy to calculate ideal current densities to allow for a normalized comparison of bulk and bulk-probe I-V data. The normalized graphs of those plotted previously in Figure 45 with adjusted current density can be seen in Figure 46 below. When comparing these graphs, there are some interesting observations that can be made. Namely, it would seem that ideal contact sizes were not of ideal values as those assumed and that when comparing the magnitudes of the I-V plots in both Figures 45 and 46 that the effective contact areas of both methods must be fairly similar in size or that some property of the samples studied caused a negligible difference in current density when considering varying contact size. Another possible cause could be poor adhesion or degradation of deposited metals as alluded to previously. This could result in measurements where the effective contact area for both methods would be that of the probe tip area or some range between the radius of the deposited metal contact and the probe tip area in contact with the substrate/metal contact. Alternatively, this behavior could be explained if the junctions formed were blocking contacts where I-V plots can be modeled as unable to be forward-biased, essentially operating in the RB for positive and negative bias. Changes in contact area being far-less obvious looking at traditional MS junctions in the RB than in the FB.

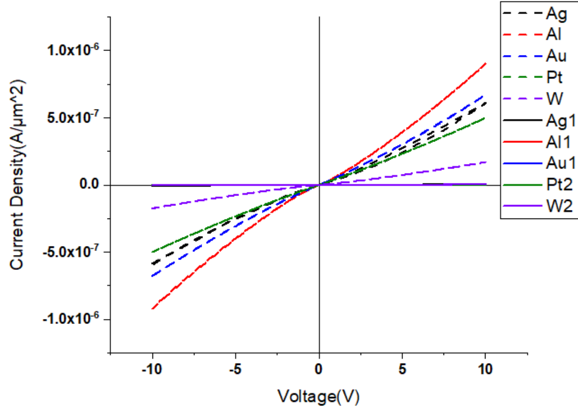

(a) Bulk versus bulk probe J-V plot (100).

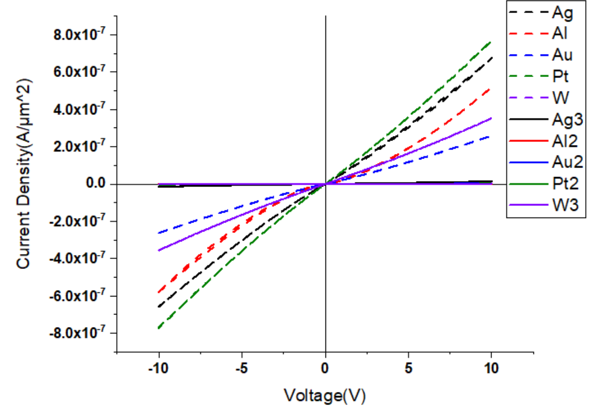

(b) Bulk versus bulk probe J-V plot (111).

Figure 46. Summary single-metal bulk versus bulk probe J-V plots.

4.3.6 I-V Curve Fitting.

Initial curve fitting as described in Section 3.6.4 was conducted using bulk I-V data obtained on the (100) sample, the I-V plots from this experiment can be seen in Figure 47 below, where Sub-Figure (a) represents the I-V plot from 0-10 V applied bias and Sub-Figure (b) represents a zoomed-in plot from 0-0.8 V applied bias, both plotted against the $ln(Y)$ axis. Despite successfully identifying and fitting a linear region of the FB I-V plots, it was determined that I-V data collected throughout this study did not have sufficient resolution to effectively determine the correct linear region. This is evidenced through the plotted MS ideal I-V curve depicted as blue dashed line in both plots. Due to hardware limitations of the I-V measurement setup used in this study, step sizes of 0.5 V were the smallest able to be measured when sweeping from -10 V to 10 V. The MS ideal I-V line is plotted with a step size of .5 mV seemingly of sufficient resolution to determine the linear region needed for this curve fitting method and is therefore recommended as a maximum step size for any future analysis of this type. There are many studies and methods similar to the one attempted in this study and could further optimize or offer more information from I-V plots such as those outlined in

[53, 54, 55, 56, 46, 57, 58, 59]. Matlab code used to plot and curve-fit the I-V data used to plot the graphs below can be found in Appendix B.

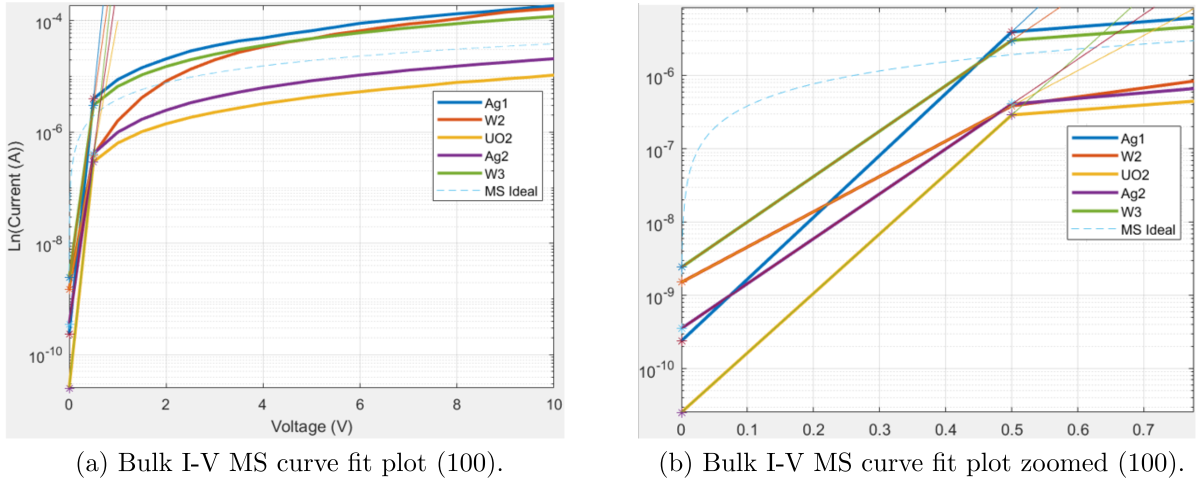

(a) Bulk I-V MS curve fit plot (100).

(b) Bulk I-V MS curve fit plot zoomed (100).

Figure 47. Bulk I-V MS curve fit plots on (100) sample depicting fitted lines and ideal MS I-V data.

Metal-Schottky-Metal (MSM) analysis was also briefly studied because it more accurately models the type of I-V measurements taken throughout this research as it considers both metal contacts as forming Schottky barriers with the substrate. This analysis is more representative of what is typically seen in experimentation, especially when dealing with intrinsic materials. Further modeling of metal contacts made to UO_2 would benefit greatly from a working MSM fitting model, studies such as [14, 60] use a "back-to-back" Schottky diode model to fit experimental data, allowing for extraction of the effective barrier heights Φ_B and the ideality factor n from a single I-V measurement.

4.4 Max Current Versus Work Function

Using probes coated with single and binary-metals with work functions as identified in Sections 4.2.1 and 4.2.2 as well as I_{MAX} values obtained from I-V measurements using said probes, I_{MAX} versus work function were plotted in Figure

48 for the (100) and (111) samples. It would be expected, based on an ideal semiconductor of n-type, with decreasing work function that I_{MAX} should increase to some point and then level off. This would be indicative of barrier lowering, in which more carriers are allowed to flow through the junction. This behavior is not observed here, instead peaks in I_{MAX} are observed occurring at two different work function values and points to some departure from ideal semiconductor behavior of the UO_2 samples used in this study.

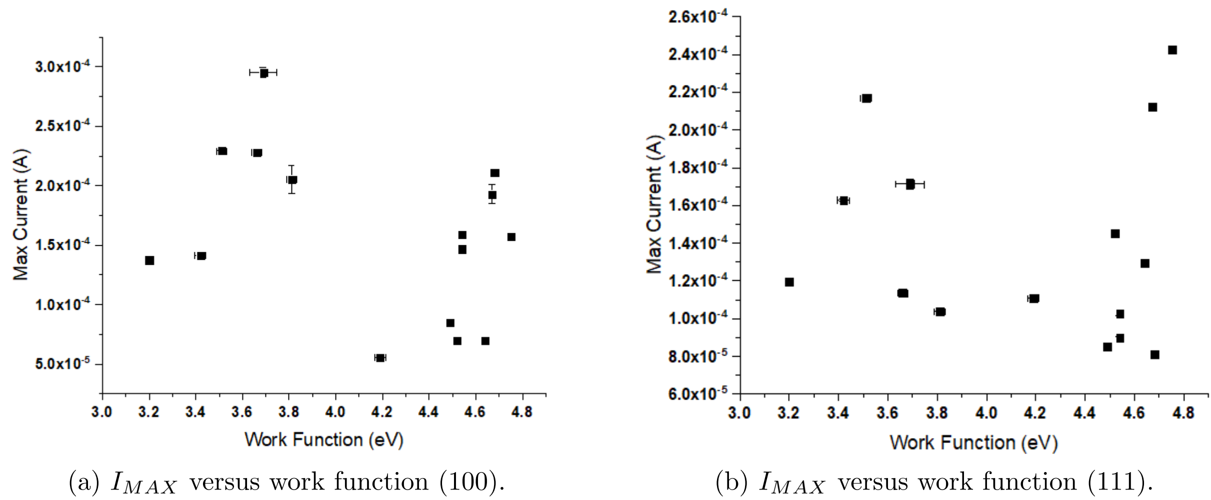

(a) I_{MAX} versus work function (100).

(b) I_{MAX} versus work function (111).

Figure 48. Maximum current versus work function using bulk-probe I-V measurements.

V. Conclusion

5.1 Summary of Findings

At the onset of this study, it was determined that the primary objective of this research was to establish processes to determine what metals could be deposited onto UO_2 samples to serve as electrical contacts that would allow for further electrical characterization of the material. In doing so, samples of hydrothermally grown UO_2 were systematically studied and used to answer the following questions:

1. Do any of the contact metals tested prove to form adequate ohmic electrical junctions with the samples tested?
2. Were any important trends in the data collected deemed important or provided useful information with regard to device fabrication?

Despite limitations on the availability of UO_2 samples and restrictions on facilities and processing of those samples, all questions have been answered sufficiently and have provided a path forward for further research in this area.

5.1.1 Effective Contact Metals.

I-V analysis through the bulk, contact-to-contact, and bulk-probe methods allowed for a novel look at how deposited and mechanical metal contacts interacted with the UO_2 samples systematically analyzed throughout this study. Each method offered a unique look at these interactions and offered distinct information that allowed for a cohesive solution. Comparative analysis offered insight into effective metals used to form electrical contacts and yielded some important information with regard to device fabrication.

Bulk I-V plots through each of the deposited contacts on both the (100) and (111) sample yield results specific to each of the samples analyzed. On the (100) sample, it appeared that only two of the contact metals formed functional junctions with the UO_2 substrate: Ag and W. Ag outperformed W in both max current through the junction and linear conformity with Ag attaining a maximum current throughput of .2 mA while W produced a slightly lower current and an asymmetric, non-linear I-V plot. On the (111) sample, contact metals of Ag, Pt, Au and W appeared to form function junctions. Ag far outperformed the other contact metals with a maximum current throughput of .455 mA with a mostly linear I-V plot despite some signs of mild hysteresis.

I-V plots obtained using the contact-to-contact method offered functional contact combinations with metals of Ag, Au, Pt, and W. While several metals formed effective junctions on the UO_2 substrates, Ag-Ag contacts far out-performed other combinations on both the (100) and (111) samples with maximum current throughputs of 1.5 mA and 1.79 mA respectively with mostly ohmic behavior presented on the I-V plots.

Bulk-probe measurements utilizing single and binary-metal sputtered probes applied to the UO_2 substrate offered a different perspective of how metals forming mechanical junctions with the surface behaved. All of the probes tested proved to form effective junctions with the substrate consisting of a variety of metals to include: Ag, Al, Au, Co, Cu, Mg, Mo, Ni, Pt, and W. Of the single-metal probes tested, Al in addition to Au and Ag performed the best on the (100) surface and on the (111) surface Pt, Ag and Al showed the most promising results. The max current throughput of Al, Au, and Ag on the (100) sample were .295 mA, .213 mA, and .192 mA respectively. Pt, Ag, and Al on the (111) sample had max currents of .242 mA, .210 mA, and .181 mA. Sputtered probes with binary films consisting of

mixtures containing AuMg, AgMg, PtMg, and WMg were also analyzed using the bulk-probe I-V method. All binary-metal probes proved to form effective junctions that performed better than the W reference probe. On the (100) sample, probes consisting WMg, PtMg, and AgMg performed optimally with max currents of .229 mA for both WMg and PtMg probes and .212 mA for the AgMg probes. On the (111) sample, probes consisting of WMg and AuMg performed better than others with max currents of .217 mA and .162 mA respectively.

5.1.2 Important Observations/Trends.

Several observations and trends were noticed throughout this study and are summarized within this section and include effects on measured work function values due to composition of co-sputtered thin films, sputtered thin film thickness, and the effects of RTA treatments on sputtered thin films. Some important trends when looking at I-V measurements were also observed and include shifts in max current (I_{MAX}) with replicate runs, a possible relationship to barrier height, and important information with respect to device fabrication when comparing bulk and bulk-probe measurements.

Looking at results within Section 4.2.2, it can be easily seen that varied compositions of Au-Mg compositions result in a decreasing work function with increased Mg content up to ~90% Mg where oxides begin to form and increase the measured work function values. In Section 4.2.3, an observed dependence of single-metal Pt films of varied thicknesses are depicted where work function values can be seen increasing from the tungsten probe substrate measured value of 4.49 eV up to 4.79 eV with a deposited Pt thickness of 55 nm. It is postulated that Pt film thicknesses ≥55 nm effectively "mask" the substrate of which they are deposited on. In Section 4.2.4, a brief look at the effects of RTA treatments of Au-Pt co-sputtered

films on their measured work functions was performed. It was found that despite showing a difference in work function values post treatment, there was not enough data to determine if these differences were statistically significant or which factors studied contributed to those differences. It was suggested that more samples were required in order to determine significance with the following sample sizes being adequate to attribute significance to each factor: Pt content - 5, RTA time - 20, and RTA temperature - 8.

Looking at results within Section 4.3, there are some interesting trends with respect to I_{MAX} and repeated I-V measurements. These trends are depicted graphically in Figures 37, 40, 42, and 44. The first thing to note is that values of I_{MAX} appear to change with repeated measurements over time and is visible despite which I-V method was looked at, this trend is especially noticeable with the Ag contacts. It is posed that some causes of this phenomenon could be due to the junction changing over time or due to a build-up of charge at the junction. Another interesting trend can be seen when within Section 4.3.3.2 where I_{MAX} can be seen changing with increased/decreased work function of the co-sputtered probes used in the I-V measurements and is likely indicative of a change in barrier height though more data points would be needed to verify this. Comparison of single-metal bulk and bulk-probe I-V measurements with Section 4.3.4 appear to solidify the existence of poor metal adhesion to the UO_2 substrate and/or the formation of blocking contacts. With the exception of Ag and W on the (100) sample and Ag, Au, and W on the (111) sample, mechanical contacts performed better than the deposited ones pointing to poor adhesion or formation of deposited contacts. Lastly, when looking at I_{MAX} versus work function plots for both of the samples in Section 4.4, it appears that there is a departure from true semiconductor behavior. This, along with the measured density of localized states of UO_2 as depicted in Figure 20,

confirm that the material is not truly a semiconductor.

5.2 Future Work

Within the scope of work performed throughout this study, there are many improvements to processes used and measurements taken that could be of great interest in future studies of related work. Regarding the I-V measurements performed in the bulk and bulk -probe methods, better effort to electrically isolate UO_2 samples would allow for more consistent results across measurement methods. Using a probe-to-probe setup as opposed to the probe-to-chuck used in this study could satisfy this requirement. Taking more I-V measurements across the UO_2 and deposited metal contact surfaces would allow for a more representative view with regard to uniformity.

Creating a greater range of binary-metal sputtered probes and depositing binary-metal contacts to the UO_2 surface would allow for a better picture of changing barrier height with regard to changing work function. Optimal contacts could be obtained using combinations of metals such as Ag, Au, Al, and Pt than those utilizing single-metals alone. On this note, an adhesion metal study would be of great benefit as it is assumed that poor adhesion hindered the analysis of some of the metal contacts looked at in this study. It would be of interest to study Cr, Ti, Ag, and W for use as thin adhesion layers (5-10 nm) prior to contact metal deposition. Further study of the RTA treatments on both the effects of work function and to treat deposited metal contacts to achieve a more intimate junction with the UO_2 could be of some interest as well.

Generally, being able to obtain larger, more uniform, and highly repeatable growths of UO_2 samples would allow for more statistically sound results and enable techniques such as transmission line measurements (TLM) to determine contact and

sheet resistances of the material more accurately. Research into possible doping methods of UO_2 would allow for traditional semiconductor device fabrication and better performing devices being possibly the single-most important issue to be solved with regard to using UO_2 in this capacity.

Appendix A.

1.1 Alloy Phase Diagrams

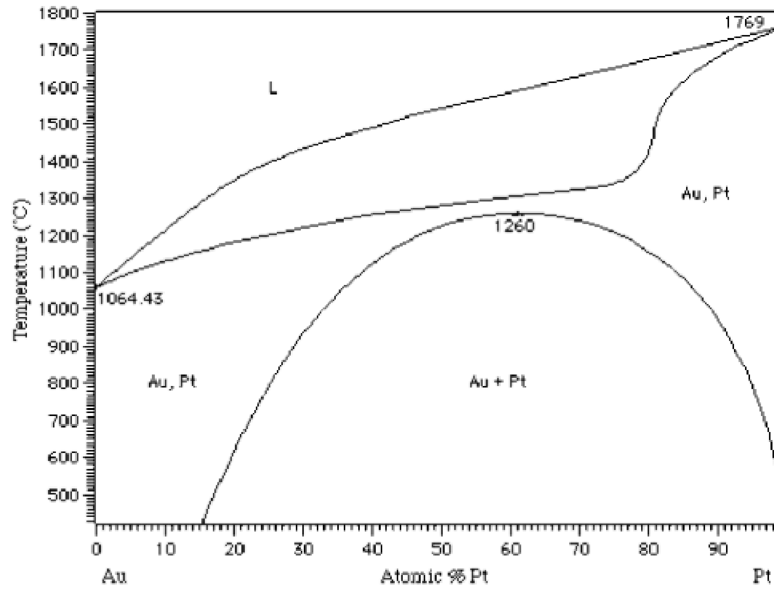

Figure 49. Equilibrium binary alloy phase diagram for gold-platinum alloys [61].

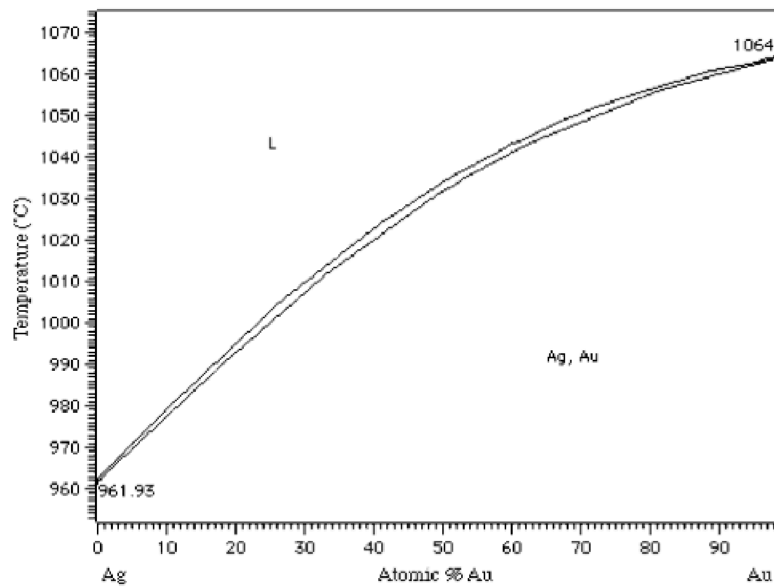

Figure 50. Equilibrium binary alloy phase diagram for gold-silver alloys [61].

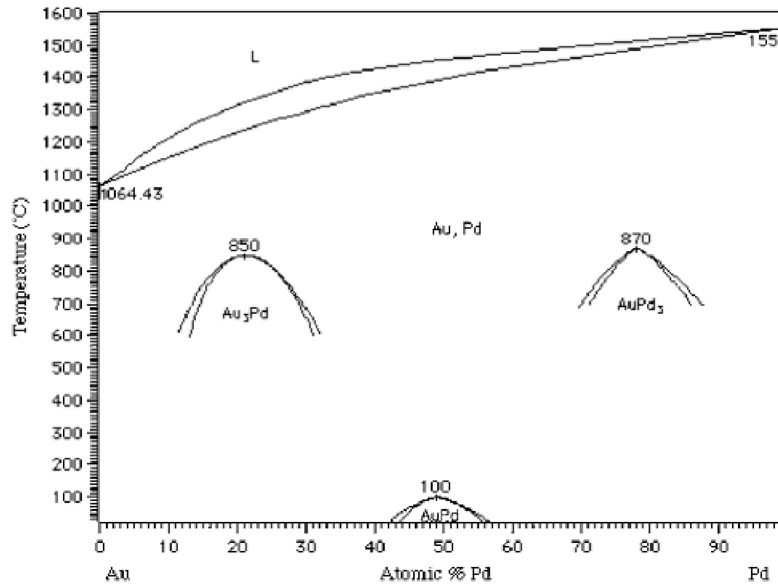

Figure 51. Equilibrium binary alloy phase diagram for gold-palladium alloys [61].

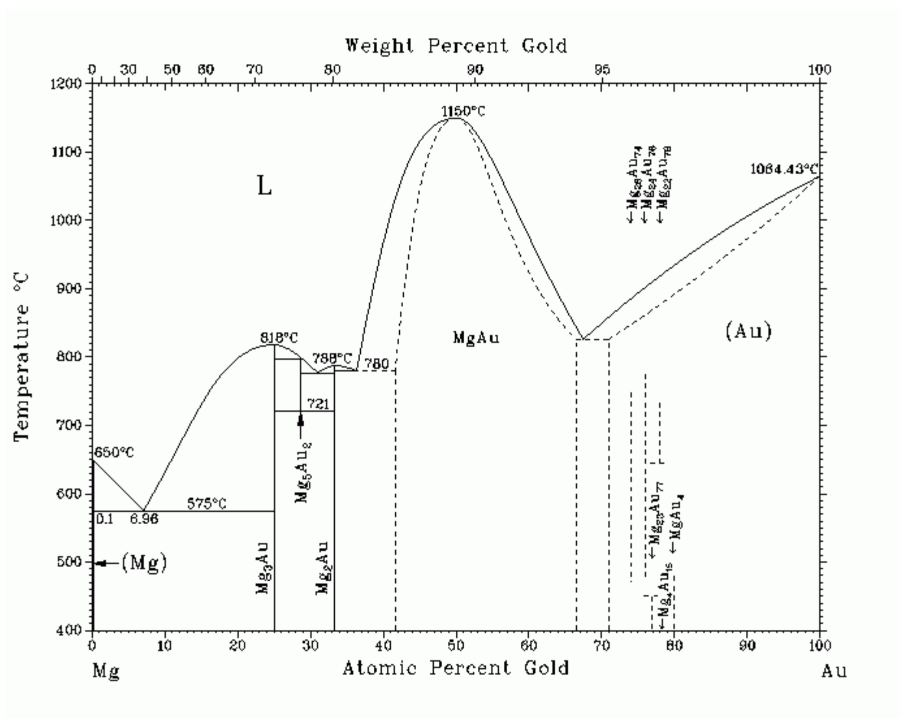

Figure 52. Equilibrium binary alloy phase diagram for gold-magnesium alloys [62].

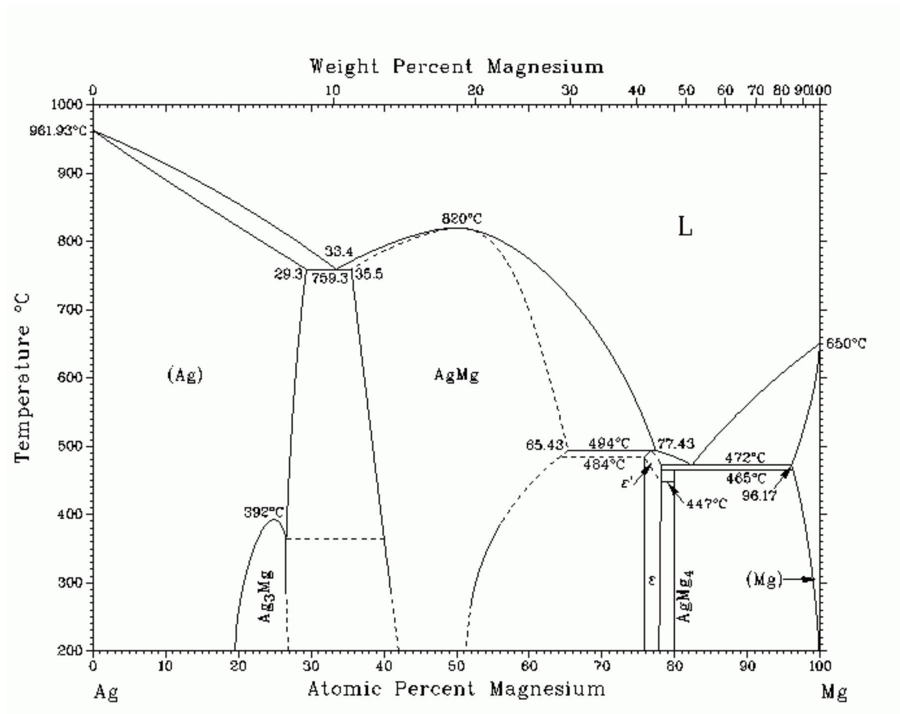

Figure 53. Equilibrium binary alloy phase diagram for silver-magnesium alloys [62].

1.2 Fission Cross-Section of Elements

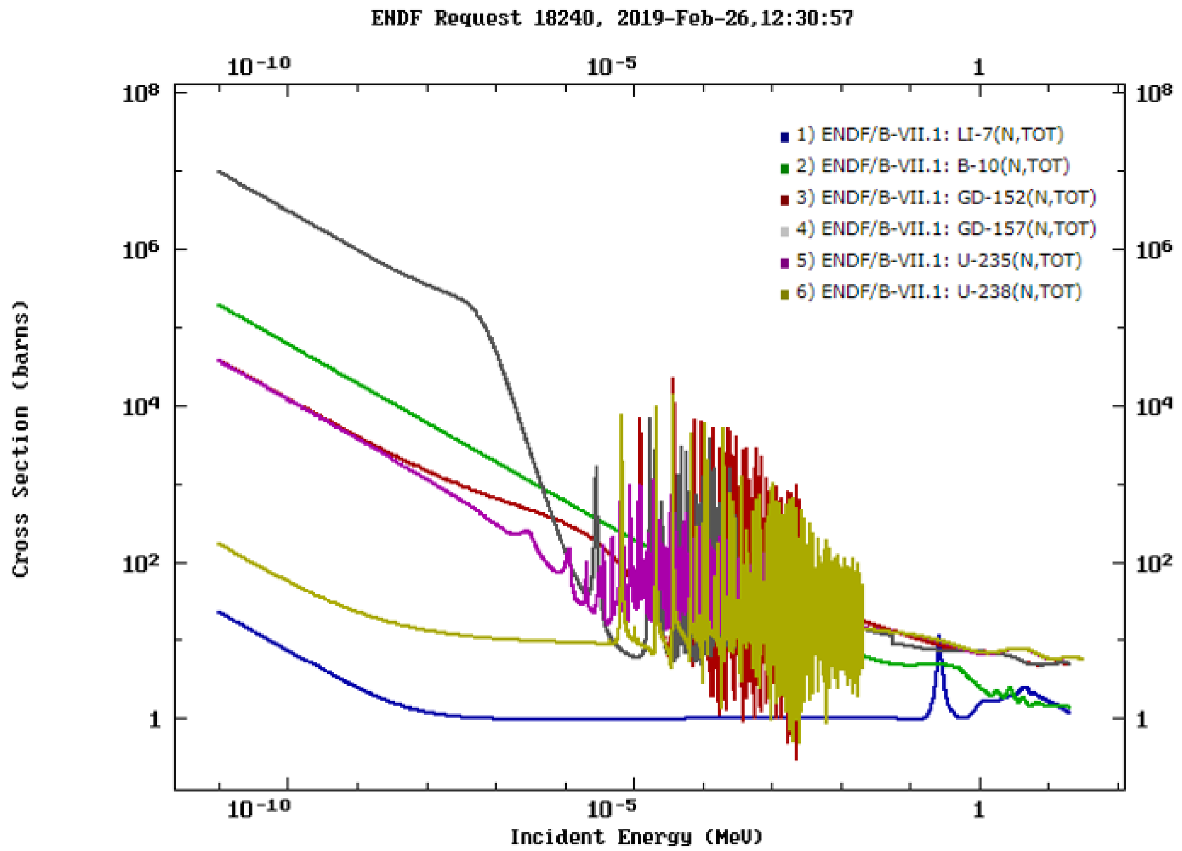

Figure 54. Fission cross-section of Li-7, B-10, Gd-152, Gd-157, U-235, and U-238 [63].

1.3 Single-Metal and Alloy Sputter Settings

Table 10. Deposition power and rate for single-metal films

	Ag				Al				Au				Co			
Power (W)	35	50	100	200	100	200	300	350	35	50	100	200	50	100	200	300
Deposition Rate (nm/min)	4.6	5.5	9.9	18.1	3.6	7.3	8.5	12.4	2.6	4.7	12.4	18.2	2.8	6.8	9.5	10.2
	Cu				**Mg**				**Mo**				**Ni**			
Power (W)	-	50	100	200	35	50	100	200	50	100	200	300	50	100	200	300
Deposition Rate (nm/min)	-	4.9	10.0	17.4	2.0	4.5	8.5	18.7	2.4	3.5	9.0	9.6	2.4	4.7	11.1	14.5
	Pt				**W**											
Power (W)	35	50	100	200	50	100	200	300								
Deposition Rate (nm/min)	2.8	3.3	5.0	11	2.5	5.7	6.8	7.9								

Table 11. Deposition power and rate for co-sputtered alloy films

	Ag				Al				Au				Co			
Power (W)	35	50	100	200	100	200	300	350	35	50	100	200	50	100	200	300
Deposition Rate (nm/min)	4.6	5.5	9.9	18.1	3.6	7.3	8.5	12.4	2.6	4.7	12.4	18.2	2.8	6.8	9.5	10.2
	Cu				**Mg**				**Mo**				**Ni**			
Power (W)	-	50	100	200	35	50	100	200	50	100	200	300	50	100	200	300
Deposition Rate (nm/min)	-	4.9	10.0	17.4	2.0	4.5	8.5	18.7	2.4	3.5	9.0	9.6	2.4	4.7	11.1	14.5
	Pt				**W**											
Power (W)	35	50	100	200	50	100	200	300								
Deposition Rate (nm/min)	2.8	3.3	5.0	11	2.5	5.7	6.8	7.9								

Note: Deposition rate for alloys is cumulative for both targets. Sputter power for alloys is noted as metal 1 power/ metal 2 power.

1.4 Current-Voltage Measurement Plots

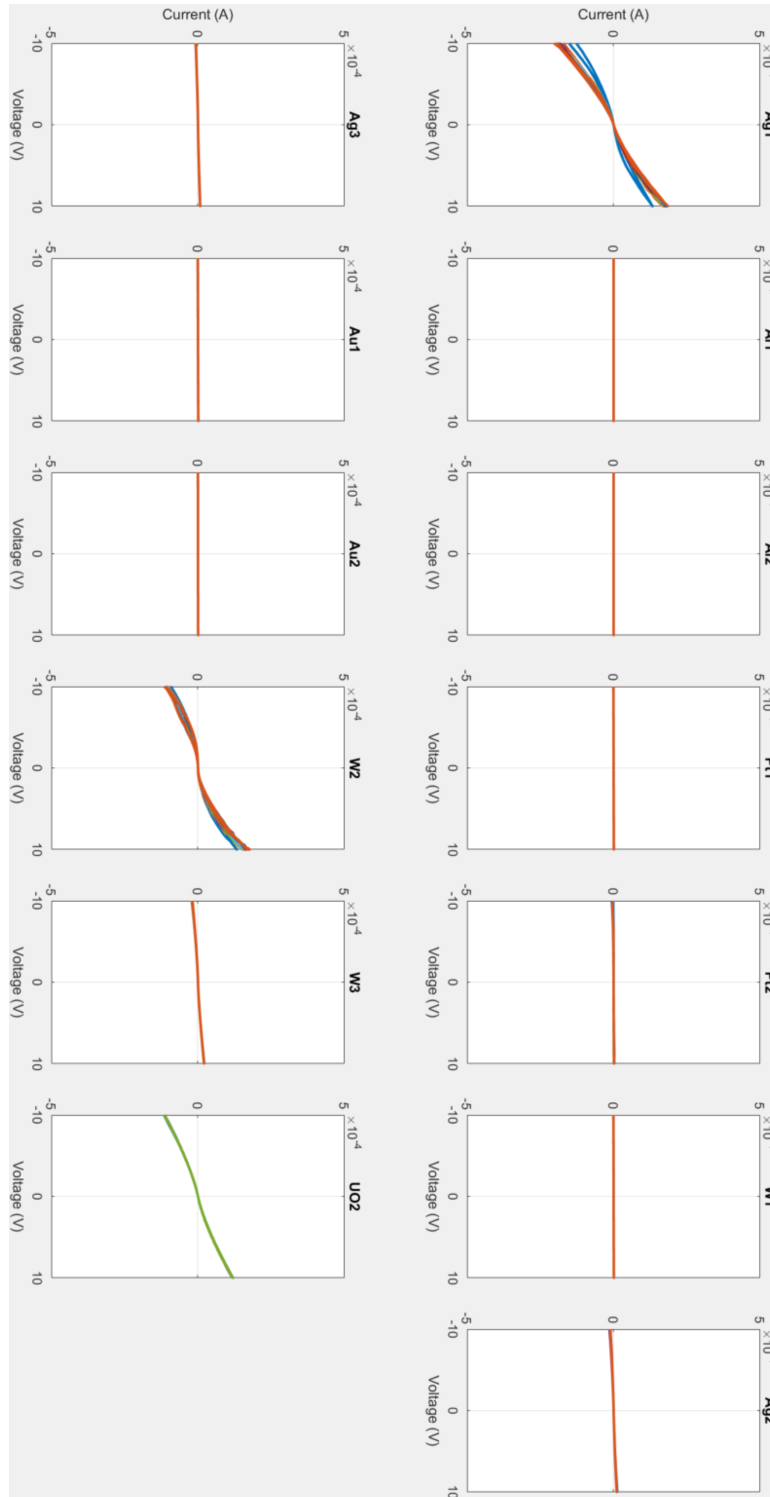

Figure 55. Bulk I-V plot for (100) UO_2 sample

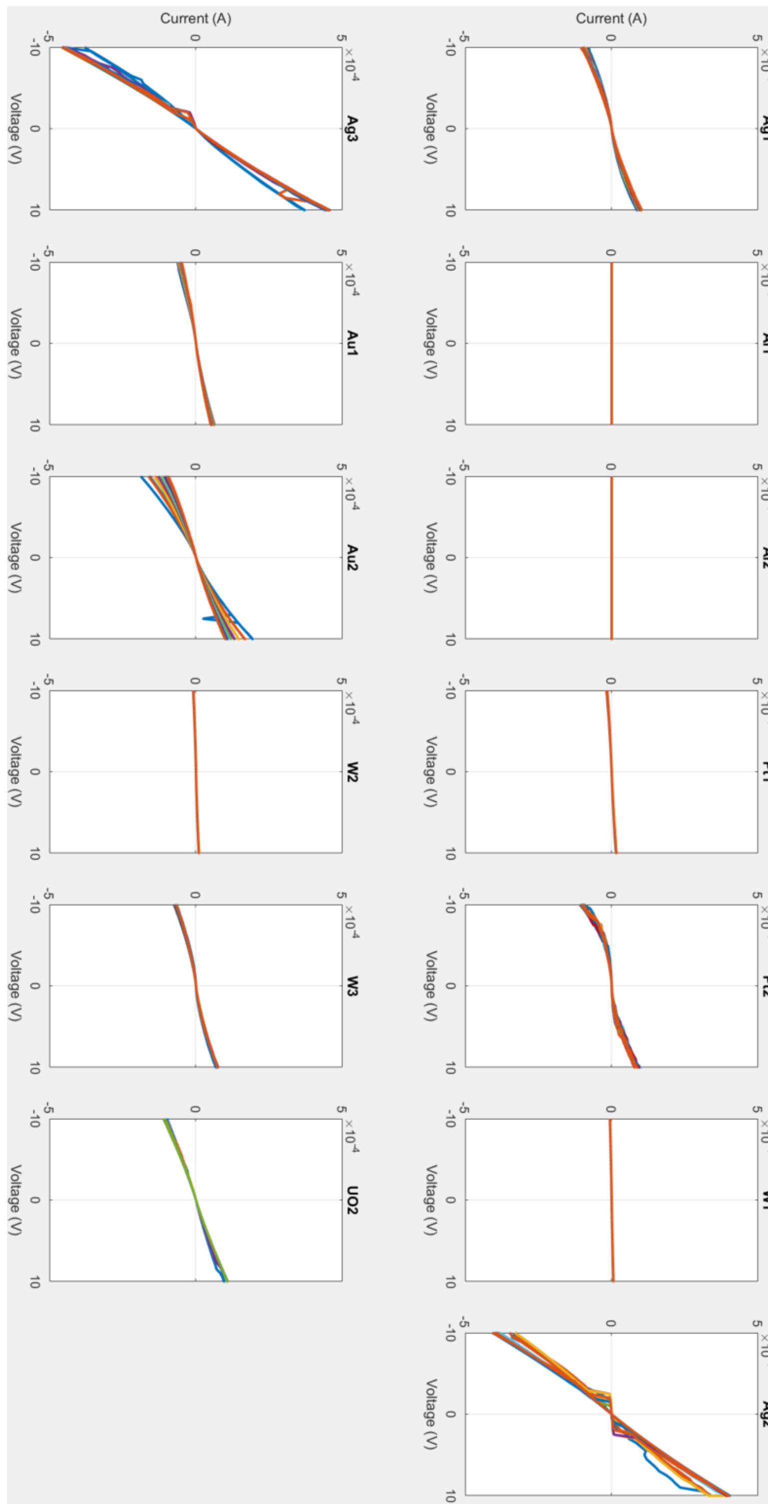

Figure 56. Bulk I-V plot for (111) UO_2 sample

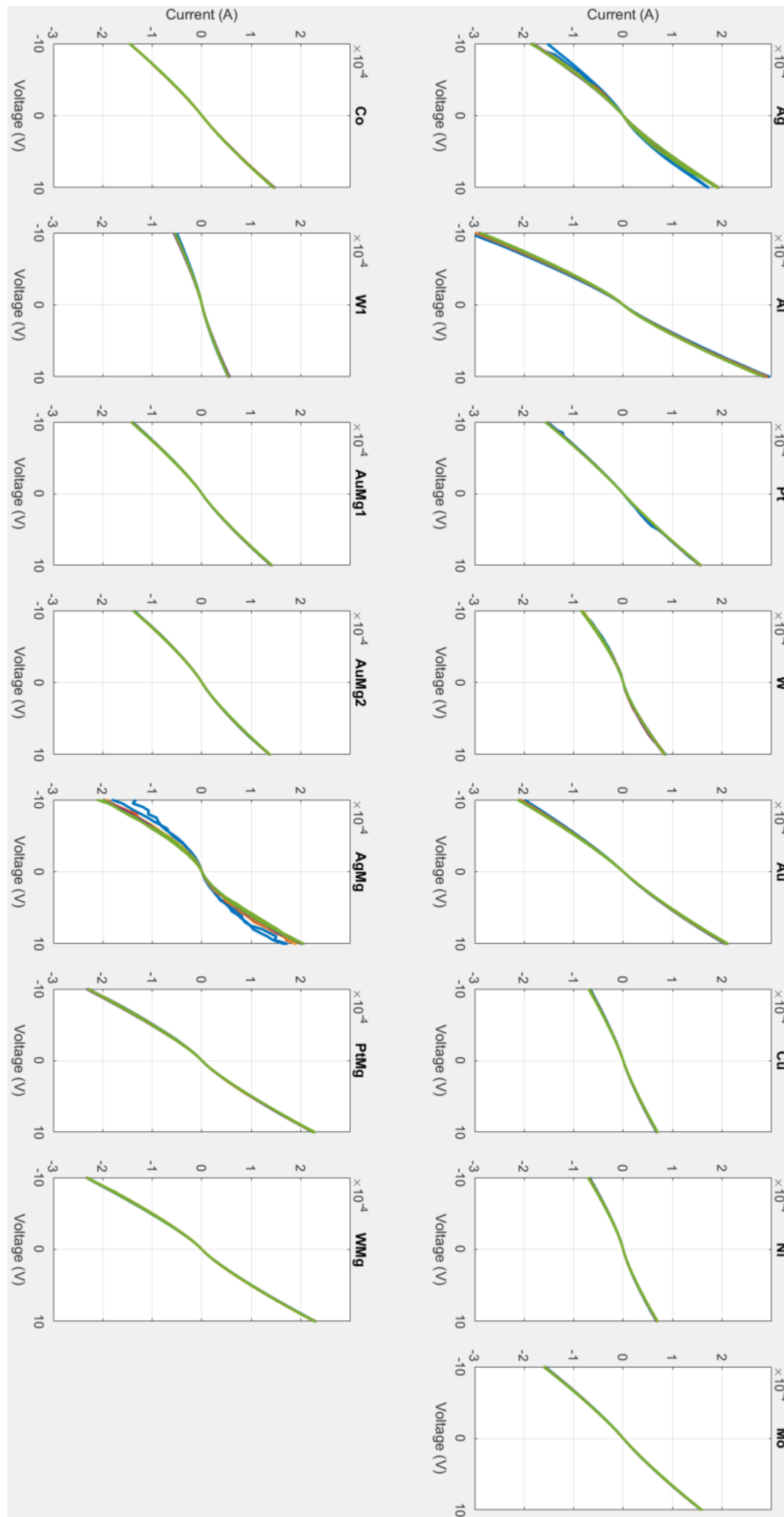

Figure 57. Bulk probe I-V plot for (100) UO_2 sample

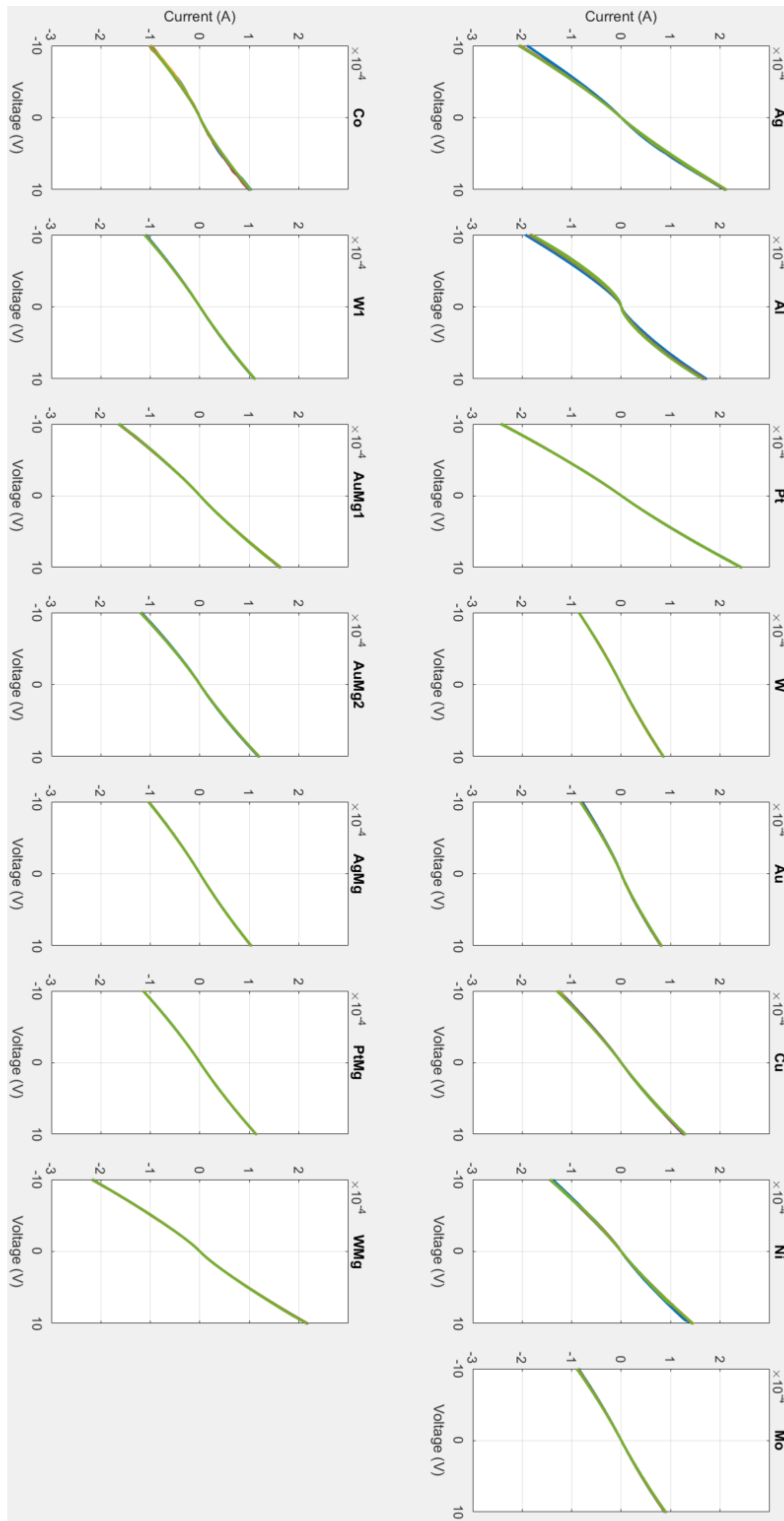

Figure 58. Bulk probe I-V plot for (111) UO_2 sample

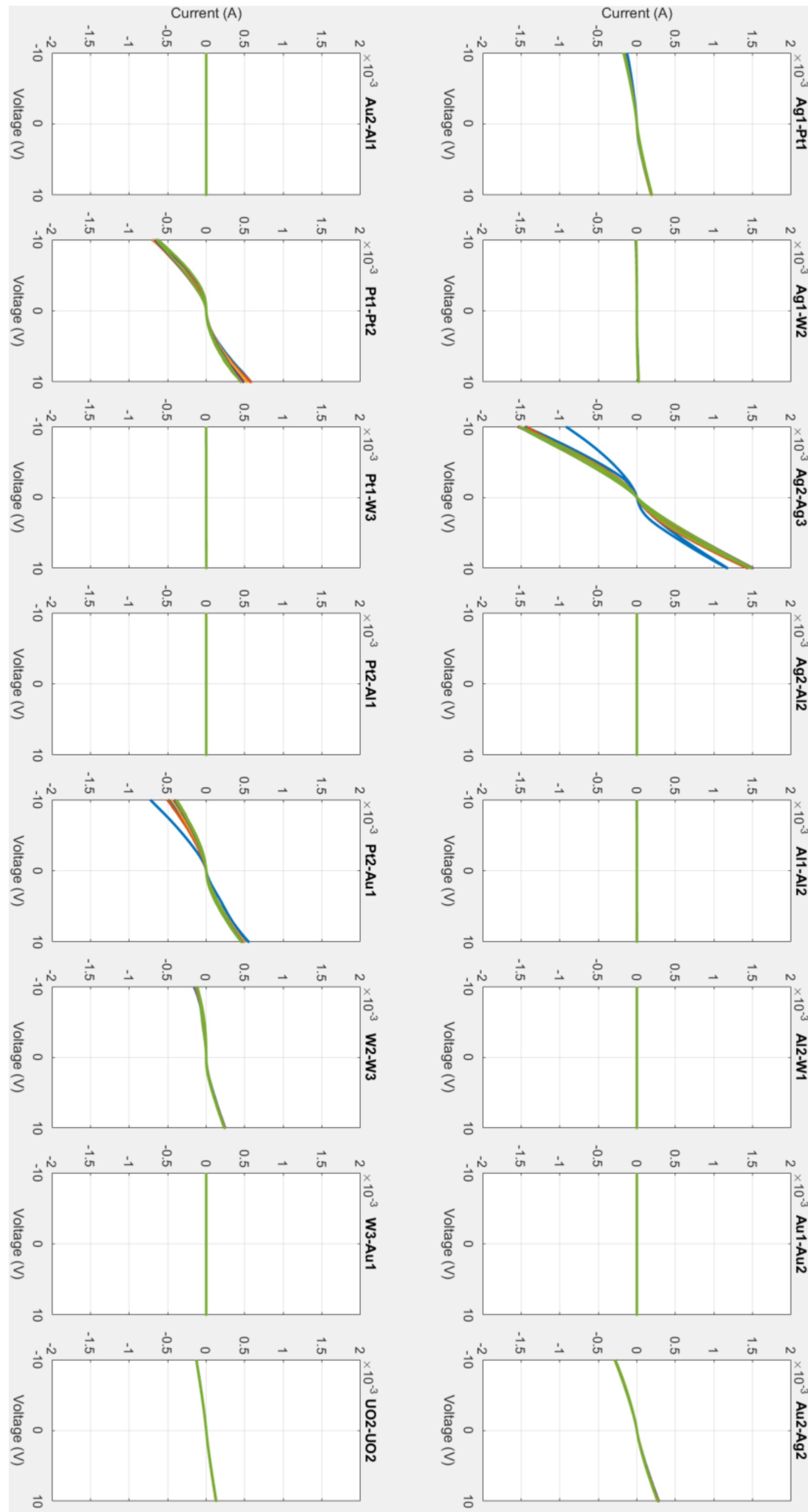

Figure 59. Contact-to-contact I-V plot for (100) UO_2 sample

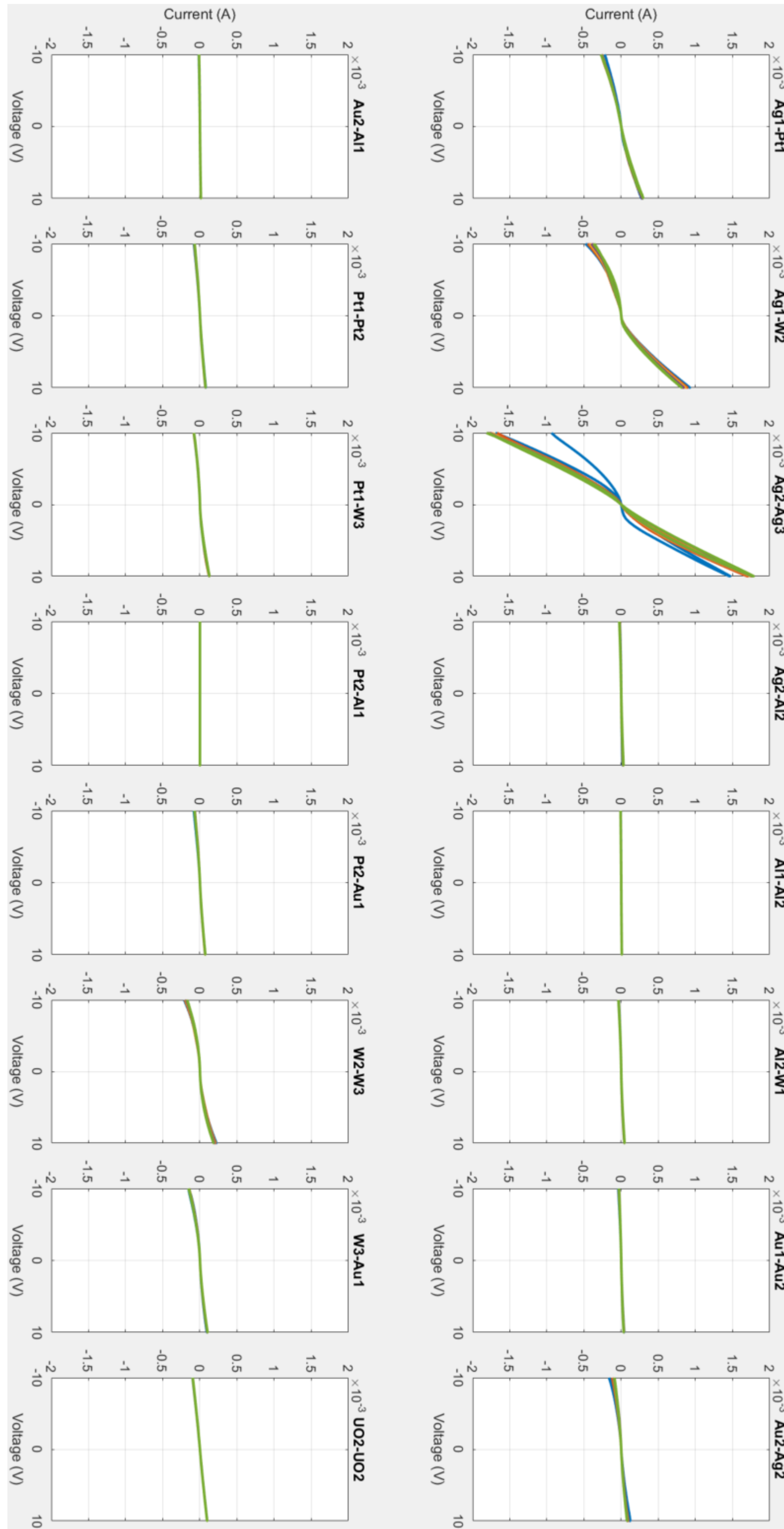

Figure 60. Contact-to-contact I-V plot for (111) UO_2 sample

Appendix B. I-V Curve Fitting Code

```
1  filename = 'I_V_Curve_Fit.xlsx'; %File name of Excel Workbook ...
       with I-V data
2  %----------(100) Bulk Graphs-----------
3  data = xlsread(filename,'B_100'); %Worksheet name of I-V data
4  B=.0259;
5  Data = zeros(100,2);
6  i=1;
7  for col = 1 : 2 : 10
8          x=data(1:21, col); %Pulls in voltage data (rows 1-21)
9          y=data(1:21, col +1); %Pulls in current data (rows 1-21)
10         semilogy(x,y,'-','LineWidth',2);
11         ylim([0 1.9E-4]);
12         legend('Ag1','W2','UO2','Ag2','W3');
13         hold on;
14 end
15 for col = 1 : 2 : 10 %adjust to # of I-V plot data to pull in (10 ...
       columns of data = 2 x 5 sets of I-V)
16 [rows, columns] = size(data);
17         x=data(1:2, col); %adjust range to linear region to be fitted
18         y=data(1:2, col +1); %adjust range to linear region to be ...
               fitted
19         y1=log(y);
20         c=polyfit(x,y1,1);
21         slope=c(1);
22         n=1/(B*slope)
23         Is=exp(c(2))
24         Data(i,1)=n;
25         Data(i,2)=Is;
26         i=i+1;
```

```
27          semilogy(x,exp(y1),'*','HandleVisibility','off');
28          hold on;
29          semilogy(0:.5:1,exp(polyval(c,0:.5:1)),'-','HandleVisibility','off');
30          hold on;
31  end
32  csvwrite('B_100_IV_Data.txt',Data); %writes n and Is values to ...
        .txt file
33  grid on;
34  xlabel('Voltage (V)');
35  ylabel('Ln(Current (A))');
36  title('Bulk 100');
```

Bibliography

1. Z. W. Bell, D. A. Carpenter, S. S. Cristy, V. E. Lamberti, A. Burger, B. F. Woodfield, T. Niedermayr, I. D. Hau, S. E. Labov, S. Friedrich, W. G. West, K. R. Pohl, and L. Van Den Berg, "Neutron detection with cryogenics and semiconductors," *Physica Status Solidi C: Conferences*, vol. 2, no. 5, pp. 1592–1605, 2005.

2. C. M. Young, "Evaluation of hydrothermally synthesized uranium dioxide for novel semiconductor applications," PhD Thesis, Air Force Institute of Technology, 2016.

3. N. Hong, J. Mullins, K. Foreman, and S. Adenwalla, "Boron carbide based solid state neutron detectors: the effects of bias and time constant on detection efficiency," *Journal of Physics D: Applied Physics*, vol. 43, no. 27, p. 275101, Jun. 2010. [Online]. Available: https://doi.org/10.1088%2F0022-3727%2F43%2F27%2F275101

4. A. N. Caruso, P. A. Dowben, S. Balkir, N. Schemm, K. Osberg, R. W. Fairchild, O. B. Flores, S. Balaz, A. D. Harken, B. W. Robertson, and J. I. Brand, "The all boron carbide diode neutron detector: Comparison with theory," *Materials Science and Engineering: B*, vol. 135, no. 2, pp. 129 – 133, 2006. [Online]. Available: http://www.sciencedirect.com/science/article/pii/S0921510706005101

5. C. L. Dugan, G. G. Peterson, A. Mock, C. Young, J. M. Mann, M. Nastasi, M. Schubert, L. Wang, W.-n. Mei, I. Tanabe, P. A. Dowben, J. Petrosky, C. L. Dugan, G. G. Peterson, A. Mock, C. Young, J. M. Mann, M. Nastasi, M. Schubert, L. Wang, W.-n. Mei, I. Tanabe, P. A. Dowben, and J. Petrosky, "Electrical and material properties of hydrothermally grown single Electrical and material properties of hydrothermally grown single crystal (111) UO2," 2018.

6. T. T. Meek, M. Hu, and M. J. Haire, "Semiconductive Properties of Uranium Oxides," *Waste Management 2001 Symposium*, pp. 0–6, 2001. [Online]. Available: http://www.wmsym.org/archives/2001/14/14-3.pdf

7. T. T. Meek and B. von Roedern, "Semiconductor devices fabricated from actinide oxides," *Vacuum*, vol. 83, no. 1, pp. 226–228, 2008.

8. C. A. Kruschwitz, S. Mukhopadhyay, D. Schwellenbach, T. Meek, B. Shaver, T. Cunningham, and J. P. Auxier, "Semiconductor neutron detectors using depleted uranium oxide," vol. 9213, p. 92130C, 2014. [Online]. Available: http://proceedings.spiedigitallibrary.org/proceeding.aspx?doi=10.1117/12.2063501

9. J. P. McKelvey, *Solid state and semiconductor physics.* Malabar, Fla: Krieger Pub. Co, 1982.

10. B. V. Van Zeghbroeck, *Principles of semiconductor devices and heterojunctions.* Upper Saddle River, N.J.; London: Prentice Hall ; Pearson Education [distributor, 2010, oCLC: 456836708.

11. R. S. Muller, T. I. Kamins, and M. Chan, *Device electronics for integrated circuits*, 3rd ed. New York, NY: John Wiley & Sons, Inc, 2003.

12. J. P. McKelvey, *Solid state physics for engineering and materials science*, original ed ed. Malabar, Fla: Krieger Pub. Co, 1993.

13. S. M. Sze and K. K. Ng, *Physics of semiconductor devices*, 3rd ed. Hoboken, N.J: Wiley-Interscience, 2007.

14. R. Nouchi, "Extraction of the Schottky parameters in metal-semiconductor-metal diodes from a single current-voltage measurement," *Journal of Applied Physics*, vol. 116, no. 18, 2014.

15. J.-P. Colinge and C. A. Colinge, *Physics of Semiconductor Devices*, 2005.

16. T. V. Laurvick, "Improvements to Micro-Contact Performance and Reliability," PhD Thesis, Air Force Institute of Technology, 2016.

17. B. Brown, S. D. Wolter, B. R. Stoner, and J. T. Glass, "Alloying Effects of Cosputtered Gold-Platinum Thin Films on the Oxygen Reduction Reaction in Acidic Electrolyte," *Journal of The Electrochemical Society*, vol. 155, no. 8, p. B852, 2008. [Online]. Available: http://jes.ecsdl.org/cgi/doi/10.1149/1.2939210

18. "Asperity (materials science)," Jul. 2018, page Version ID: 849059137. [Online]. Available: https://en.wikipedia.org/w/index.php?title=Asperity_(materials_science)&oldid=849059137

19. B. F. Toler, R. A. Coutu, and J. W. McBride, "A review of micro-contact physics for microelectromechanical systems (MEMS) metal contact switches," *Journal of Micromechanics and Microengineering*, vol. 23, no. 10, p. 103001, Oct. 2013. [Online]. Available: http://stacks.iop.org/0960-1317/23/i=10/a=103001?key=crossref.0dcec364e0b6838ac8b850adeb443090

20. B. F. Toler, R. A. Coutu, and J. W. McBride, "A review of micro-contact physics for microelectromechanical systems (MEMS) metal contact switches," *Journal of Micromechanics and Microengineering*, vol. 23, no. 10, 2013.

21. C. L. Dugan, "Electrical Characterization of Crystalline UO2, THO2 and U0.71TH0.29O2," PhD Thesis, Air Force Institute of Technology, 2018.

22. G. Leinders, T. Cardinaels, K. Binnemans, and M. Verwerft, “Accurate Lattice Parameter Measurements of Stoichiometric Uranium Dioxide,” *JOURNAL OF NUCLEAR MATERIALS*, vol. 459, pp. 135–142, 2015. [Online]. Available: http://dx.doi.org/10.1016/j.jnucmat.2015.01.029

23. C. Young, J. Petrosky, J. M. Mann, E. M. Hunt, D. Turner, and T. Kelly, “The work function of hydrothermally synthesized UO 2 and the implications for semiconductor device fabrication,” *physica status solidi (RRL) - Rapid Research Letters*, vol. 10, no. 9, pp. 687–690, 2016. [Online]. Available: https://www.scopus.com/inward/record.uri?eid=2-s2.0-85007545300&doi=10.1002%2Fpssr.201600203&partnerID=40&md5=8a8d72946e8a801f130aab8644da0237%5Cnhttp://doi.wiley.com/10.1002/pssr.201600203

24. Y. Baer and J. Schoenes, “Electronic structure and Coulomb correlation energy in UO2 single crystal,” *Solid State Communications*, 1980.

25. R. K. Willardson, J. W. Moody, and H. L. Goering, “The Electrical Properties of Uranium Oxides,” *Journal of Inorganic and Nuclear Chemistry*, vol. 6, no. 1, pp. 19–33, 1958.

26. P. W. Winter, “The electronic transport properties of UO2,” *Journal of Nuclear Materials*, vol. 161, pp. 38–43, 1989.

27. S. L. Dudarev, D. N. Manh, and A. P. Sutton, “Effect of Mott-Hubbard correlations on the electronic structure and structural stability of uranium dioxide,” *Philosophical Magazine B*, vol. 75, no. 5, pp. 613–628, May 1997. [Online]. Available: https://www.tandfonline.com/doi/full/10.1080/13642819708202343

28. G. Hyland and J. Ralph, “Electronic contributions to the high-temperature thermophysical properties of UOsub(2+x): a critical analysis,” *High Temperatures - High Pressures*, vol. 15, no. 2, pp. 179–190, 1983. [Online]. Available: http://inis.iaea.org/search/search.aspx?orig_q=RN:15013104

29. J. M. Casado, J. H. Harding, and G. J. Hyland, “Small-polaron hopping in Mott-insulating UO $_2$,” *Journal of Physics: Condensed Matter*, vol. 6, no. 25, pp. 4685–4698, Jun. 1994. [Online]. Available: http://stacks.iop.org/0953-8984/6/i=25/a=007?key=crossref.95083602c19b385c7eb2e9e01dd25b7e

30. A. R. Massih, “Electronic transport in pure and doped UO2,” *Journal of Nuclear Materials*, vol. 497, pp. 166–182, 2017. [Online]. Available: https://doi.org/10.1016/j.jnucmat.2017.07.035

31. H. Bao, P. Duan, J. Zhou, H. Cao, J. Li, H. Yu, Z. Jiang, H. Liu, L. Zhang, J. Lin, N. Chen, X. Lin, Y. Liu, Y. Huang, and J.-Q. Wang, “Uranium-Induced Changes in Crystal-Field and Covalency Effects of Th $^{4+}$ in Th $_{1-x}$ U $_x$ O $_2$

Mixed Oxides Probed by High-Resolution X-ray Absorption Spectroscopy," *Inorganic Chemistry*, vol. 57, no. 18, pp. 11 404–11 413, Sep. 2018. [Online]. Available: http://pubs.acs.org/doi/10.1021/acs.inorgchem.8b01142

32. H. Lee, R. A. Coutu, S. Mall, and K. D. Leedy, "Characterization of metal and metal alloy films as contact materials in MEMS switches," *Journal of Micromechanics and Microengineering*, vol. 16, no. 3, pp. 557–563, 2006.

33. D. E. Eastman, "Photoelectric work functions of transition, rare-earth, and noble metals," *Physical Review B*, vol. 2, no. 1, pp. 1–2, 1970.

34. W. M. H. Sachtler, G. J. H. Dorgelo, and A. A. Holscher, "The Work Function of Gold," *Surface Science*, vol. 5, pp. 221–229, 1966.

35. E. W. Müller, "Work function of tungsten single crystal planes measured by the field emission microscope," *Journal of Applied Physics*, vol. 26, no. 6, pp. 732–737, 1955.

36. R. A. Coutu, P. E. Kladitis, K. D. Leedy, and R. L. Crane, "Selecting metal alloy electric contact materials for MEMS switches," *Journal of Micromechanics and Microengineering*, vol. 14, no. 8, pp. 1157–1164, 2004.

37. G. Peterson, "Electrical Characterization of Irradiated Semiconducting Amorphous Hydrogenated Boron Carbide," Ph.D. dissertation, University of Nebraska Lincoln, Aug. 2017. [Online]. Available: http://digitalcommons.unl.edu/mechengdiss/124

38. S. E. Inc., "Diagram of DC Magnetron Sputtering Process," 2019. [Online]. Available: http://www.semicore.com/images/photos/diagram-dc-magnatron.png

39. L. Hanke, *Handbook of analytical methods for materials*, 2001.

40. Y. Leng, *Materials characterization: introduction to microscopic and spectroscopic methods*, second edition ed. Weinheim: Wiley-VCH, 2013.

41. "Lift Mode Surface Potential Imaging (AM-KPFM)." [Online]. Available: http://www.nanophys.kth.se/nanophys/facilities/nfl/afm/icon/bruker-help/Content/Interleave%20Scanning/LiftMode%20SurfacePotentialDetectionPrinciples.htm

42. W. Melitz, J. Shen, A. C. Kummel, and S. Lee, "Kelvin probe force microscopy and its application," *Surface Science Reports*, vol. 66, no. 1, pp. 1–27, 2011. [Online]. Available: http://dx.doi.org/10.1016/j.surfrep.2010.10.001

43. M. Kumar and R. Mitra, "Effect of substrate temperature and annealing on structure, stress and properties of reactively co-sputtered Ni-TiN nanocomposite thin films," *Thin Solid Films*, vol. 624, pp. 70–82, 2017.

44. D. C. Montgomery, *Design and analysis of experiments*, eighth edition ed. Hoboken, NJ: John Wiley & Sons, Inc, 2013.

45. R. F. Pierret, *Advanced semiconductor fundamentals*, 2nd ed., ser. Modular series on solid state devices. Upper Saddle River, N.J: Prentice Hall, 2003, no. v. 6.

46. R. M. Cibils and R. H. Buitrago, "Forward I - V plot for nonideal Schottky diodes with high series resistance," *Journal of Applied Physics*, vol. 58, no. 2, pp. 1075–1077, Jul. 1985. [Online]. Available: http://aip.scitation.org/doi/10.1063/1.336222

47. M. Nikolić, S. Radić, V. Minić, and M. Ristić, "The dependence of the work function of rare earth metals on their electron structure," *Microelectronics Journal*, vol. 27, no. 1, pp. 93–96, Feb. 1996. [Online]. Available: http://linkinghub.elsevier.com/retrieve/pii/0026269295000976

48. M. Chelvayohan and C. H. B. Mee, "Work function measurements on (110), (100) and (111) surfaces of silver," *Journal of Physics C: Solid State Physics*, vol. 15, no. 10, pp. 2305–2312, Apr. 1982. [Online]. Available: http://stacks.iop.org/0022-3719/15/i=10/a=029?key=crossref.0888e03a776e234254f6ea33a0cf5773

49. M. Chelvayohan and C. H. B. Mee, "Work function measurements on (110), (100)and (111) surfaces of silver," p. 9.

50. T. Leniogne and H. Montes, "Aluminum Work Function: Effect of Oxidation, Mechanical Scraping, and Ion Bombardment," p. 18.

51. S. Fain and J. McDavid, "Work-function variation with alloy composition: Ag-Au," *Physical Review B*, vol. 9, no. 12, pp. 5099–5107, Jun. 1974. [Online]. Available: https://link.aps.org/doi/10.1103/PhysRevB.9.5099

52. J. Cohen, *Statistical power analysis for the behavioral sciences*, 2nd ed. Hillsdale, N.J: L. Erlbaum Associates, 1988.

53. C.-D. Lien, F. So, and M.-A. Nicolet, "An improved forward I-V method for nonideal Schottky diodes with high series resistance," *IEEE Transactions on Electron Devices*, vol. 31, no. 10, pp. 1502–1503, Oct. 1984. [Online]. Available: http://ieeexplore.ieee.org/document/1484024/

54. M. Lyakas, R. Zaharia, and M. Eizenberg, "Analysis of nonideal Schottky and pn junction diodes—Extraction of parameters from I-V plots," *Journal of Applied Physics*, vol. 78, no. 9, pp. 5481–5489, Nov. 1995. [Online]. Available: http://aip.scitation.org/doi/10.1063/1.359664

55. H. Norde, “A modified forward I-V plot for Schottky diodes with high series resistance,” *Journal of Applied Physics*, vol. 50, no. 7, pp. 5052–5053, Jul. 1979. [Online]. Available: http://aip.scitation.org/doi/10.1063/1.325607

56. S. K. Cheung and N. W. Cheung, “Extraction of Schottky diode parameters from forward current-voltage characteristics,” *Applied Physics Letters*, vol. 49, no. 2, pp. 85–87, Jul. 1986. [Online]. Available: http://aip.scitation.org/doi/10.1063/1.97359

57. K. Ahmed and T. Chiang, “Schottky barrier height extraction from forward current-voltage characteristics of non-ideal diodes with high series resistance,” *Applied Physics Letters*, vol. 102, no. 4, 2013.

58. J. H. Werner, “Schottky barrier and pn-junction I-V plots -Small signal evaluation,” *Applied Physics A Solids and Surfaces*, vol. 47, no. 3, pp. 291–300, Nov. 1988. [Online]. Available: http://link.springer.com/10.1007/BF00615935

59. V. Aubry and F. Meyer, “Schottky diodes with high series resistance: Limitations of forward I-V methods,” *Journal of Applied Physics*, vol. 76, no. 12, pp. 7973–7984, Dec. 1994. [Online]. Available: http://aip.scitation.org/doi/10.1063/1.357909

60. A. J. Chiquito, C. A. Amorim, O. M. Berengue, L. S. Araujo, E. P. Bernardo, and E. R. Leite, “Back-to-back Schottky diodes: The generalization of the diode theory in analysis and extraction of electrical parameters of nanodevices,” *Journal of Physics Condensed Matter*, vol. 24, no. 22, 2012.

61. H. Okamoto, *Desk handbook: phase diagrams for binary alloys.* Materials Park, OH: ASM International, 2000, oCLC: ocm46310868.

62. A. A. Nayeb-Hashemi, J. B. Clark, and A. International, Eds., *Phase diagrams of binary magnesium alloys*, ser. Monograph series on alloy phase diagrams. Metals Park, Ohio: ASM International, 1988.

63. “E4/Servlet: Output.” [Online]. Available: https://www.nndc.bnl.gov/exfor/servlet/E4sMakeE4

REPORT DOCUMENTATION PAGE	*Form Approved* *OMB No. 0704-0188*

The public reporting burden for this collection of information is estimated to average 1 hour per response, including the time for reviewing instructions, searching existing data sources, gathering and maintaining the data needed, and completing and reviewing the collection of information. Send comments regarding this burden estimate or any other aspect of this collection of information, including suggestions for reducing the burden, to Department of Defense, Washington Headquarters Services, Directorate for Information Operations and Reports (0704-0188), 1215 Jefferson Davis Highway, Suite 1204, Arlington, VA 22202-4302. Respondents should be aware that notwithstanding any other provision of law, no person shall be subject to any penalty for failing to comply with a collection of information if it does not display a currently valid OMB control number.
PLEASE DO NOT RETURN YOUR FORM TO THE ABOVE ADDRESS.

1. REPORT DATE *(DD-MM-YYYY)*	2. REPORT TYPE	3. DATES COVERED *(From - To)*
21-03-2019	Master's Thesis	August 2017 - March2019

4. TITLE AND SUBTITLE
Characterization of Metal Contacts on Hydrothermally Synthesized Uranium Dioxide For Novel Semiconductor Applications

5a. CONTRACT NUMBER

5b. GRANT NUMBER

5c. PROGRAM ELEMENT NUMBER

6. AUTHOR(S)
Robinson, Tory E., Captain, USAF

5d. PROJECT NUMBER

5e. TASK NUMBER

5f. WORK UNIT NUMBER

7. PERFORMING ORGANIZATION NAME(S) AND ADDRESS(ES)
Air Force Institute of Technology
Graduate School of Engineering and Management (AFIT/EN)
2950 Hobson Way
Wright-Patterson AFB OH 45433-7765

8. PERFORMING ORGANIZATION REPORT NUMBER
AFIT-ENG-19-M-052

9. SPONSORING/MONITORING AGENCY NAME(S) AND ADDRESS(ES)
Intentionally Left Blank

10. SPONSOR/MONITOR'S ACRONYM(S)

11. SPONSOR/MONITOR'S REPORT NUMBER(S)

12. DISTRIBUTION/AVAILABILITY STATEMENT
DISTRIBUTION A. APPROVED FOR PUBLIC RELEASE; DISTRIBUITION UNLIMITED.

13. SUPPLEMENTARY NOTES
This work is declared a work of the U.S. Government and is not subject to copyright protection in the United States.

14. ABSTRACT
This research is focused on determining which metals or combinations of metals form effective electrical contacts on hydrothermally synthesized UO2 substrates to allow for additional work in characterization of the material as well as the feasibility of its use in semiconductor devices such as solid-state neutron detectors. A methodology was established for selection of candidate metals. Target mixtures composed of Au, Ag, Pt, and Mg were chosen along with several single-metals. Thin metal films were deposited onto tungsten probe tips and hydrothermally synthesized UO2 samples to allow for analysis of mechanical and deposited contact to the substrates through I-V measurements.

15. SUBJECT TERMS
Uranium Dioxide, contact study, semiconductor

16. SECURITY CLASSIFICATION OF: a. REPORT	b. ABSTRACT	c. THIS PAGE	17. LIMITATION OF ABSTRACT	18. NUMBER OF PAGES	19a. NAME OF RESPONSIBLE PERSON
U	U	U	UU	115	Maj Tod Laurvick, AFIT/ENG
					19b. TELEPHONE NUMBER *(Include area code)* (312) 785-3636 x4382 Tod.Laurvick@afit.edu